2011

Modeling, Design And Fabrication Of Orthogonal And Psuedo-orthogonal Frequency Coded Saw Wireless Spread Spectrum Rfid Sensor Tags

Nancy Saldanha
University of Central Florida

MODELING, DESIGN AND FABRICATION OF ORTHOGONAL AND PSUEDO-ORTHOGONAL FREQUENCY CODED SAW WIRELESS SPREAD SPECTRUM RFID SENSOR TAGS

by

NANCY VOLGA SALDANHA
B.S. University of Central Florida, 2001
M.S. University of Central Florida, 2003

A dissertation submitted in partial fulfillment of the requirements
for the degree of Doctor of Philosophy
in the Department of Electrical Engineering and Computer Science
in the College of Engineering and Computer Science
at the University of Central Florida
Orlando, Florida

Spring Term
2011

Major Professor: Donald C. Malocha

ABSTRACT

Surface acoustic wave (SAW) sensors offer a wireless, passive sensor solution for use in numerous environments where wired sensing can be expensive and infeasible. Single carrier frequency SAW sensor embodiments such as delay lines, and resonators have been used in single sensor environments where sensor identification is not a necessity. The orthogonal frequency coded (OFC) SAW sensor tag embodiment developed at UCF uses a spread spectrum approach that allows interrogation in a multi-sensor environment and provides simultaneous sensing and sensor identification. The SAW device is encoded via proper design of multiple Bragg reflectors at differing frequencies. To enable accurate device design, a model to predict reflectivity over a wide range of electrode metallization ratios and metal thicknesses has been developed and implemented in a coupling of modes (COM) model. The high coupling coefficient, reflectivity and temperature coefficient of delay (TCD) of YZ $LiNbO_3$ makes it an ideal substrate material for a temperature sensor, and the reflectivity model has been developed and verified for this substrate.

A new concept of pseudo-orthogonal frequency coded (POFC) SAW sensor tags has been investigated, and with proper design, the POFC SAW reduces device insertion loss and fractional bandwidth compared to OFC. OFC and POFC sensor devices have been fabricated at 250 MHz and 915 MHz using fundamental operation, and 500 MHz and 1.6 GHz using second harmonic operation. Measured device results are shown and compared with the COM simulations using the

enhanced reflectivity model. Additionally, the first OFC devices at 1.05 GHz were fabricated on 128^o YX $LiNbO_3$ to explore feasibility of the material for future use in OFC sensor applications.

Devices at 915 MHz have been fabricated on YZ $LiNbO_3$ and integrated with an antenna, and have then been used in a transceiver system built by Mnemonics, Inc. to wirelessly sense temperature. The first experimental wireless POFC SAW sensor device results and predictions will be presented.

To my mother who taught me that anything can be accomplished through hard work and perseverance. To my father, who always encouraged me to pursue my dreams. I could not have done this without your continued love and support.

ACKNOWLEDGMENTS

Foremost, I offer my sincerest gratitude to my adviser, Dr. Donald Malocha, who has supported me throughout my graduate career and offered significant technical guidance towards the completion of this work. I am grateful for his unfailing support, and patience and for many tecnhical discussions that helped me solve the technical problems I encountered during this work; I owe my success largely to his mentoring and encouragement. Dr. Malocha has been a very positive influence in my life, I have learned so much from him and I am truly grateful for his friendship.

I am grateful to my parents for their undying love and support; for believing in me when I didn't and for getting me through some of the difficult moments in life. I am grateful to my brother Kelvin, who has always been encouraging and supportive. I thank him for his help with proofreading this manuscript. I could never have completed this without you all.

I thank the rest of my dissertation committee, Dr. Samuel Richie, Dr. Glenn Boreman and Dr. Xun Gong for their time and support. I would also like to express my gratitude to Dr. Robert Youngquist for his support, encouragement and insightful comments and suggestions. I am grateful to NASA for funding this research through the STTR and SBIR programs and the Graduate Student Researchers Program (GSRP). I would also like to thank the Florida Space Grant Consortium (FSGC) and the Florida High Technology I-4 Corridor Grant for financial support. I thank my managers, Alejandro Zajac and Emmanuelle Briot at TriQuint Semiconductor Inc., for allowing

me to utilize their fabrication facilities while I was employed with them and for encouraging me to continue my PhD work.

I would like to express my gratitude to all my friends and colleagues at the Consortium for Applied Acoustoelectronic Technology (CAAT) at the University of Central Florida for their technical contributions. I want to especially thank Derek Puccio and Nikolai Kozlovski for many fruitful technical discussions over the past several years. I am also grateful to Daniel Gallagher, Mark Gallagher, and Brian Fisher for spending many long hours with me fixing equipment and for help with device fabrication whenever I needed it. I also thank Daniel Gallagher for providing the LaTex template which helped tremendously in typing and formatting this dissertation. Thank you all for the fun times and for making this journey a memorable one.

TABLE OF CONTENTS

LIST OF FIGURES . . . . . **xii**

LIST OF TABLES . . . . . **xxiv**

CHAPTER 1 : INTRODUCTION **1**

CHAPTER 2 : SAW MODELING BACKGROUND **4**

2.1 SAW Modeling Techniques 4

2.1.1 Delta Function Model 4

2.1.2 Equivalent Circuit Model 6

2.1.3 Finite Element Method 8

2.1.4 Coupling of Modes Model 8

2.2 Coupling of Modes Theory Review 9

CHAPTER 3 : COUPLING OF MODES MODEL **12**

3.1 Reflector COM Equations 12

3.2 Solutions of the Reflector COM Equations 18

3.3 Transducer COM Equations and Solutions 20

3.3.1 SAW Transducer P-matrix Representation 22

3.3.2 The Transduction Parameter 25

3.4 Harmonic Modeling 26

3.5 Cascading of P-Matrices 29

3.5.1 One-Port P-Matrix Cascade 31

3.5.2 Two-Port P-Matrix Cascade 33

CHAPTER 4 : MODELING OF SAW REFLECTOR COM PARAMETERS FOR ALUMINUM ELECTRODES ON YZ LITHIUM NIOBATE 34

4.1 Experimental Extraction of SAW Reflectivity and Grating Velocity 36

4.1.1 Test Device Structure 36

4.1.2 Method of Reflectivity and Velocity Extraction 38

4.2 Existing Transmission Line Model 40

4.3 Modified Transmission Line Model 44

4.3.1 First Harmonic Operation 44

4.3.2 Second Harmonic Operation 46

4.4 Experimental Results 48

4.4.1 Results for First Harmonic Operation 48

4.4.2 Results for Second Harmonic Operation 55

4.4.3 Reflector Loss Discussion 61

CHAPTER 5 : SPREAD SPECTRUM IMPLEMENTATION OF SAW RFID TAGS AND SENSORS 65

5.1 Spread Spectrum Concepts 66

5.1.1 Direct Sequence Spread Spectrum (DSSS) 67

5.1.2 Frequency Hopped Spread Spectrum (FHSS) 70

5.1.3 Orthogonal Frequency Division Multiplexing (OFDM) 74

5.2 Spread Spectrum Techniques For Sensors 77

5.2.1 Single Frequency CDMA Tags 78

5.2.2 Orthogonal Frequency Coded Tags 79

CHAPTER 6 : ORTHOGONAL AND PSUEDO-ORTHOGONAL FREQUENCY CODED SAW SENSORS 88

6.1 Implementation of OFC SAW Sensor 88

6.2 Development of Psuedo-Orthogonal Frequency Coding (P-OFC) 93

6.2.1 Effect of Reflector Chip Length on Tag Performance 95

6.2.2 Orthogonality Condition for P-OFC 100

6.3 Chip Correlation and Cross-Correlation Properties 107

6.4 Devices at 250 MHz 113

6.5 Device Results at 915 MHz 116

6.6 Harmonic Operation 133

6.7 Devices on 128^o YX Lithium Niobate 139

6.8 Summary of Results 141

CHAPTER 7 : DISCUSSION AND CONCLUSION 144

LIST OF REFERENCES 148

LIST OF FIGURES

Figure 2.1 The delta-function modeling of the electric field distribution under the excited IDT, with sources at finger edges 5

Figure 2.2 The equivalent circuit for a single electrode of an interdigital SAW transducer with impedance discontinuities between metallized and unmetallized regions. 7

Figure 2.3 Propagation of waves on a piezoelectric substrate 10

Figure 3.1 Propagation and coupling of Rayliegh waves in a SAW reflector grating due to the presence of metal electrodes 13

Figure 3.2 Schematic of an unweighted interdigital SAW transducer; forward and reverse propagating modes are launched when an external voltage is applied 21

Figure 3.3 Schematic showing the acoustic and electrical ports of a SAW transducer which are represented using a mixed P-matrix 23

Figure 3.4 Schematic showing the cascading of two adjacent components in a one-port SAW device. The electrical ports are in parallel and the acoustic ports are in series. 30

Figure 3.5 Schematic showing the cascading of of a two-port SAW device. The two electrical ports are isolated and the acoustic ports are in series. 33

Figure 4.1 Delay line with reflector for obtaining reflectivity measurements. Transducers contain $\frac{1}{6}$ wavelength electrodes, providing for both fundamental and second harmonic operation using a single device. 38

Figure 4.2 Experimental (S_{21}) frequency response from device structure in Fig.4.1. The reflector response appears as a ripple in the pass band of the delay line response. 39

Figure 4.3 Delay line with reflector (S_{21}) time response. The direct SAW time response appears first followed by the reflector response. The energy in the reflector's trailing edge time response is a result of inter-electrode reflections that decay later in time. 39

Figure 4.4 SAW grating (S_{21}) frequency response for a shorted grating with 25 electrodes. Solid line is COM model predicted grating response, and dotted line is experimentally extracted grating response. The extraction technique minimizes differences between the main passband of the experimental and predicted responses. 40

Figure 4.5 Transmission line representation of a SAW reflector. The perturbation introduced by the grating is represented as a series of stepped impedance and velocity discontinuities. The susceptance element represents the stored energy parameter. 41

Figure 4.6 Percent reflectivity per strip versus metallization ratio for an open grating at first harmonic operation. Shown in the dashed curve is the prediction of the electrical term for $h/\lambda = 0$ using perturbation theory given by Datta [1]. The dotted curve shows the fit to the extracted reflectivity using above equation for reflectivity at first harmonic operation. The solid line shows the fit using the modified model proposed in this paper. 43

Figure 4.7 Reflectivity per strip versus metallization ratio and normalized metal thickness for shorted aluminum gratings at fundamental operation. The metallization ratio varies from 0.2 to 0.8 and the normalized metal thickness ranges from 0.4% to 2%. 49

Figure 4.8 Reflectivity per strip versus metallization ratio and normalized metal thickness for open circuit aluminum gratings at fundamental operation. The metallization ratio varies from 0.2 to 0.9 and the normalized metal thickness ranges from 0.4% to 2%. Reflectivity per strip extracted by Härmä [2] is also plotted. 50

Figure 4.9 SEM image of a typical aluminum grating on YZ $LiNbO_3$. The grating has a metallization ratio of 0.5 as verified in the image and the metal thickness was 1200 Angstroms. 52

Figure 4.10 Grating velocity versus metallization ratio and normalized metal thickness for shorted aluminum gratings at fundamental operation. The metallization ratio varies from 0.2 to 0.8 and the normalized metal thickness ranges from 0.4% to 2%. 53

Figure 4.11 Grating velocity versus metallization ratio and normalized metal thickness for open aluminum gratings at fundamental operation. The metallization ratio varies from 0.2 to 0.9 and the normalized metal thickness ranges from 0.4% to 2%. 54

Figure 4.12 Grating reflectivity versus metallization ratio and normalized metal thickness for shorted aluminum gratings at second harmonic operation. The metallization ratio varies from 0.2 to 0.8 and the normalized metal thickness ranges from 0.8% to 4%. 56

Figure 4.13 Grating reflectivity versus metallization ratio and normalized metal thickness for open aluminum gratings at second harmonic operation. The metallization ratio varies from 0.2 to 0.8 and the normalized metal thickness ranges from 0.8% to 4%. 57

Figure 4.14 Grating velocity versus metallization ratio and normalized metal thickness for shorted aluminum gratings at second harmonic operation. The metallization ratio varies from 0.2 to 0.8 and the normalized metal thickness ranges from 0.8% to 4%. 58

Figure 4.15 Grating velocity versus metallization ratio and normalized metal thickness for open aluminum gratings at second harmonic operation. The metallization ratio varies from 0.2 to 0.8 and the normalized metal thickness ranges from 0.8% to 4%. 59

Figure 4.16 The test structure for loss extraction and the different measurements used to extract losses. A combination of reflection and transmission measurements are used to isolate losses under the grating electrodes. 62

Figure 5.1 Transmitter for a DS/SS system. The bit information and coding signal are mixed together and then translated to carrier frequency. The frequency spectrum shows the bandwidth spreading in the transmitted signal due to the coding. 67

Figure 5.2 Block diagram for a DS/SS fixed correlator receiver. The received signal r(t) is matched filtered to demodulate it and recover the original information signal. 69

Figure 5.3 Frequency hopped signal pattern. The vertical axis is a map of frequency channels and the horizontal axis indicates the dwell time in each frequency channel. 71

Figure 5.4 Block diagram of a FHSS transmitter and receiver. (a) At the transmitter the modulated data is mixed with a frequency synthesizer output to produce the frequency hopped signal. (b) At the receiver the frequency hopped signal is decoded using a synchronized synthesizer. The dehopped signal is then demodulated to recover the original data. 73

Figure 5.5 5-Subchannel spectra of an OFDM signal; although the sub-carriers have some spectral overlap, interference between channels is minimal due to sub-carrier signal orthogonality. The frequency is normalized to center frequency. 75

Figure 5.6 Block diagram of an OFDM (a)transmitter and (b)receiver. 76

Figure 5.7 Schematic of a single frequency SAW CDMA ID Tag [3]. All the reflectors are in-line in a single track which geometrically decreases the power received by subsequent reflectors. 79

Figure 5.8 Time and frequency responses of an orthogonal frequency coded stepped chirp response. The chip lengths are kept constant so that the chip frequency responses have the same bandwidths. The time responses have integer number of half wavelength cycles. Time axis is normalized to chip length and the frequency axis is normalized to the center frequency of the chirp bandwidth. 82

Figure 5.9 Schematic of a 7 chip SAW OFC RFID tag; the frequency responses of the reflector chips are orthogonal to each other. The figure shows the chirp interrogation signal and the returned noise-like signal which is the convolution of the chirp with the OFC. 85

Figure 5.10 A schematic of the interrogation and correlation receiver approach for an OFC SAW reader. 86

Figure 6.1 Picture of an 8-chip OFC SAW device being probed. The colors of the SAW reflectors is due to the interference pattern from the different center frequencies of the SAW reflectors 89

Figure 6.2 Shorted reflector responses of the eight chip OFC SAW tag shown in Fig. 6.1. Each reflector has 50 electrodes, the reflector loss is approximately 5dB per chip 90

Figure 6.3 Experimental and COM simulated S_{11} (a) frequency and (b) time responses for an 8-chip OFC SAW device. The overall device bandwidth is 40 MHz. 91

Figure 6.4 Auto-correlation and matched filter correlation of the OFC device with eight chips. Magnitude is normalized to maximum correlation and time is normalized to chip time length. 93

Figure 6.5 (a) Frequency and (b) time responses of an reflector chip of varying reflector lengths. A reflectivity of 1.4% is assumed for YZ-$LiNbO_3$. The insertion loss of the frequency response increases with increasing $Ng \cdot r$ while the null-bandwidth decreases, and the time response approaches a sin(x)/x type response with increasing $Ng \cdot r$. As $Ng \cdot r$ increases, the stored energy in the reflector due to intra-chip reflections increases and is dissipated later in time resulting in an impulse occuring at τ_c. 96

Figure 6.6 Frequency responses of 7 reflector chips with 150 electrodes using OFC and P-OFC with a reflectivity of 1.4% assumed for YZ-$LiNbO_3$. OFC shows a significant overlap of

energy between two adjacent frequency reflectors (shown by the shaded region) which causes distortion of the tag frequency response. 98

Figure 6.7 COM prediction of the insertion loss of a single chip SAW reflector grating with r=1.4% versus the product $Ng \cdot r$ is shown by the solid curve which approaches 1dB at $Ng \cdot r = 2.1$ or 150 electrodes. The absolute 4 dB bandwidth of a single chip at a center frequency of 250 MHz (shown in the dotted curve) reduces from 5 MHz at $Ng \cdot r = 0.7$ to 1.67 MHz at $Ng \cdot r = 2.1$ 99

Figure 6.8 Time response of a reflector chip on YZ $LiNbO_3$ with 150 electrodes and its time function approximation. 102

Figure 6.9 Comparison of the device auto-correlation, and matched filter correlation using the Hamming window approximation for a 5 chip P-OFC device. 103

Figure 6.10 Insertion loss of a single chip versus the product $Ng \cdot r$ is shown by the solid curve which approaches 1dB at $Ng \cdot r = 2.1$ or 150 electrodes. The fractional bandwidth of an eight chip device using OFC and P-OFC definitions are shown. The OFC definition is used for $Ng \cdot r < 0.7$ while the P-OFC definition is used for $1.2 < Ng \cdot r < 2.5$. 106

Figure 6.11 Auto-correlation of a reflector chip of varying lengths plotted versus time normalized to chip time length. The peak of the auto-correlation pulse increases from -17 dB for $Ng \cdot r = 0.7$ to -12 dB for $Ng \cdot r = 2.1$ and -11 dB for $Ng \cdot r = 2.8$. 109

Figure 6.12 Cross-correlation of first and second adjacent OFC frequencies for reflector chips with 50 electrodes. Amplitude of all three correlation pulses are normalized to the peak of the auto-correlation shown in red and plotted versus time normalized to chip length. 111

Figure 6.13 Cross-correlation of first and second adjacent OFC frequencies for reflector chips with 150 electrodes. Amplitude of all three correlation pulses are normalized to the peak of the auto-correlation of f_1 shown in red and plotted versus time normalized to chip length. There is significant energy in the cross-correlations due to the frequency distortion and overlap of long reflectors that no longer approximate the ideal OFC conditions. 111

Figure 6.14 Cross-correlation of first and second adjacent P-OFC frequencies for reflector chips with 150 electrodes. The center frequency separation is $2.4/\tau_c$MHz. Amplitude of all three correlation pulses are normalized to the peak of the auto-correlation of f_1 shown in red and plotted versus time normalized to chip length. 112

Figure 6.15 Cross-correlation of first and second adjacent bandwidth optimized P-OFC frequencies for reflector chips with 150 electrodes. The center frequency separation is $1.6/\tau_c$MHz. Amplitude of all three correlation pulses are normalized to the peak of the auto-correlation of f_1 shown in red and plotted versus time normalized to chip length. 112

Figure 6.16 Experimental (in red) and COM simulated (blue) response of an 8-chip P-OFC SAW ID tag. Experimental and COM simulation shows good agreement and no chip degradation is observed. 114

Figure 6.17 Experimental (in red) and COM simulated (blue) response of an 8-chip OFC SAW ID tag. Experimental and COM simulation shows good agreement and chip degradation is observed for chips five and seven (shown in the highlighted area). 114

Figure 6.18 Experimental gated SAW OFC reflector response (in red) and COM simulated ideal OFC reflector response (in blue) for a 8 chip P-OFC tag with 150 electrodes in each chip. 115

Figure 6.19 Experimental gated SAW OFC reflector response (in red) and COM simulated ideal OFC reflector response (in blue) for a 8 chip OFC tag with 50 electrodes in each chip. 115

Figure 6.20 Picture of OFC device at 915 MHz mounted on PCB dipole antenna. 116

Figure 6.21 Plot of measured antenna impedance, probed OFC device impedance and impedance of packaged OFC device with dipole antenna operating at 915 MHz center frequency. 117

Figure 6.22 Schematic of impedance optimized OFC device at 915 MHz. All the reflectors are inline which introduces losses from the wave propagating under adjacent reflectors. . . 118

Figure 6.23 Frequency and time responses of a 5-chip OFC device. The amplitude roll-off in time domain is due to propagation losses under the gratings and is predicted well by the COM simulation which included the loss factor under the grating electrodes. 119

Figure 6.24 Plot of single OFC sensor being heated and cooled; solid line is extracted sensor temperature and dots indicate thermocouple temperature. The discrepancies between the thermocouple and sensor temperature are due to the thermal mass of the sensor package and PCB.

Each time sample is a few seconds since the data acquisition and the adaptive filter software is in MATLAB®. 121

Figure 6.25 Time domain responses of the four orthogonal codes used for simultaneous interrogation. The codes had frequency diversity and had no time overlap to provide good cross-correlation properties. 122

Figure 6.26 Matched filter correlation with (a)single sensor (b) four sensors in the system. Side-lobe level increases as more sensor are introduced into the environment due to self-interference of multiple sensors. 124

Figure 6.27 Time domain responses of the four orthogonal codes used for simultaneous interrogation. The codes had frequency diversity and had no time overlap to provide good cross-correlation properties. 125

Figure 6.28 Time domain response of the OFC device with the improved staggered layout. The time domain roll-off is improved which enhances correlation properties. 126

Figure 6.29 Comparison of an inline chip layout and a staggered chip layout. The roll-off in chip amplitude to due propagation losses under the reflector electrodes is significantly reduced in the staggered layout case. 127

Figure 6.30 Comparison of gated reflector responses with transducer effects eliminated. P-OFC device has 5.4% fractional bandwidth and the OFC device has 11% bandwidth, the reflector loss is 3 dB lower in the P-OFC device. 128

Figure 6.31 Compressed pulse obtained from the auto-correlation of the responses of an (150 electrodes per chip) five chip OFC device and P-OFC device and a (50 electrodes per chip) five chip OFC device . The P-OFC auto-correlation has a narrower pulse. 130

Figure 6.32 Wireless interrogation of the new P-OFC device at 915MHz using transceiver from Mnemonics. The device was heated using a heat gun and then cooled using a can of gas duster held upside down. The P-OFC device had a 5.4% fractional bandwidth. 132

Figure 6.33 The S_{21} (a)frequency and (b)time response of delay line devices with reflectors. The reflector response appears as a ripple in the passband of the delay-line frequency response. Bulk radiation occurs close to the region of the second harmonic transducer passband. The reflectors operate at all harmonics with the greatest reflectivity for the given film thickness occurring at second harmonic. 134

Figure 6.34 Experimental (solid red curve) and COM modeled (dashed blue curve) S_{11} (a)frequency and (b)time responses of an OFC reflector device at second harmonic operation. The device has 5 reflector chips each on either of the transducer, hence two sets of reflections are observed in the time response. 135

Figure 6.35 (a)Time-domain response of a five chip P-OFC device at 1.6 GHz using harmonic operation. The roll-off from chip one to 5 is approximately 10 dB. (b) The gated reflector response of the P-OFC device; effects of transducer bidirectional loss and mismatch loss are eliminated, and propagation loss effects are isolated. The first chip, f_1, has a loss of 10 dB, due to free space propagation loss at 1.6GHz, chip f_5 has a loss of 20dB. 138

Figure 6.36 Comparison of the S11 frequency responses of same OFC device on on YZ $LiNbO_3$ and 128^o YX $LiNbO_3$. The device on 128^o YX $LiNbO_3$ has higher coupling, velocity and reflectivity. 140

Figure 6.37 The gated reflector responses of the OFC devices on YZ $LiNbO_3$ and 128^o YX $LiNbO_3$ with transducer effects eliminated. The frequency scale for the device on 128^o YX $LiNbO_3$ was scaled down to be centered at 915 MHz for comparison. 141

LIST OF TABLES

Table 4.1 Material Properties For Typical Single Crystal SAW Materials 34

Table 4.2 Device Variations Used For Reflectivity Extraction 37

Table 4.3 First Harmonic Coefficients for the Transmission Line Model Obtained from Least Squares Fit to the Data 55

Table 4.4 Second Harmonic Coefficients for the Transmission Line Model Obtained from Least Squares Fit to the Data 60

CHAPTER 1
INTRODUCTION

Surface acoustic wave (SAW) sensors have been studied extensively and are used widely in several wireless sensor applications. SAW devices are capable of passive wireless operation, can operate over large temperature ranges (from 0°C to 1200°C), are rugged and radiation hard. These properties make these devices extremely attractive for wireless sensor applications. Currently, a variety of SAW device embodiments such as delay lines and resonators are being used used for a variety of sensing purposes [4, 5, 6]. However, these embodiments are not ideal in multi-sensor environments, since the simultaneous transmission of both tag identification and sensed measurement is required [7, 8]. Single frequency CDMA SAW tags have been used for simultaneous sensing and tagging, but have limited range due to device reflector losses, have only time diversity for coding and are susceptible to external interference signals[9, 10, 11].

Orthogonal frequency coded (OFC) SAW sensor tags presented by Malocha and Puccio [12, 13, 3], offer a spread-spectrum solution for use of SAW tags and sensors in a multiple access environment. Use of spread-spectrum approach for sensor interrogation provides enhanced range by reducing effects of interference such as multi-path fading, noise and external jamming. The spread-spectrum coding technique allows for time and frequency diversity in coding. The design

of the OFC SAW sensors requires the use of a robust model that includes accurate predictions of device behavior on substrate materials of choice.

The high coupling coefficient, reflectivity and temperature coefficient of delay (TCD) of YZ-Lithium Niobate (YZ-$LiNbO_3$) makes it a substrate material of choice for a SAW OFC temperature sensor. The device electrode reflectivity is dependent on electrode width and metal thickness and is an important parameter in OFC SAW device design. This dissertation presents the extraction of reflectivity coefficients for aluminum electrodes on YZ $LiNbO_3$ over varying reflector properties such as electrode width and metal thickness using experimental measurements at both fundamental and second harmonic operation. A model to predict reflectivity over a wide range of electrode metallization ratios and metal thickness has been developed and implemented in the coupling of modes (COM) model to enable more accurate SAW device design.

Chapter 2 gives an overview on the available SAW device modeling techniques, such as the delta function model, the equivalent circuit or transmission line model, the finite-element model and the COM model. Chapter 3 provides an in depth explanation of the COM model used in this dissertation and the derivation of the COM equations and solutions for the SAW reflector are given as well. A thorough characterization of reflectivity of aluminum electrodes on YZ $LiNbO_3$ has been performed and an in-depth explanation of the methodology used for the extraction of reflectivity and velocity, and the experimental data are shown in Chapter 4. Additionally, the coefficients for the transmission line model obtained from a least squares fit to the measured data was incorporated into the COM model is explained in Chapter 4.

Chapter 5 provides an overview of communication theory for direct sequence and frequency hopping spread-spectrum techniques. The benefits of using a spread-spectrum approach such as immunity to jamming and multi-path interference, and multiple access are discussed. Principles of spread-spectrum signal processing such as processing gain and use of passive matched filter correlation are explained. A summary of previous work done on the orthogonal frequency coding concept and its implementation in SAW devices is given.

Chapter 6 introduces the new concept of the psuedo-orthogonal frequency coding POFC to reduce sensor insertion loss and fractional bandwidth. The POFC coding is defined, and correlation and cross-correlation properties discussed. The POFC and OFC coding are contrasted, and experimental results of both types of devices at fundamental operation of 250MHz and 915MHz and second harmonic operation of 500 MHz and 1.6 GHz are shown. The results are compared to COM modeled responses using the reflectivity model developed in this work. The first OFC SAW devices at 1 GHz on 128^o $LiNbO_3$ are shown to test feasibility. Finally, the 915 MHz OFC and POFC devices on YZ $LiNbO_3$ have then been used in a transceiver system built by Mnemonics, Inc. to wirelessly sense temperature.

In Chapter 7 a summary of the work done is given and possible areas of future research are discussed.

CHAPTER 2
SAW MODELING BACKGROUND

There are various models that have been developed over the years to model SAW devices. A few examples are the delta-function model, the equivalent circuit model, the coupling of modes (COM) model and numerical methods such as the finite element method (FEM). A brief overview of each of the mentioned models is given below. The COM model is computationally efficient and includes many of the second order effects to yield highly accurate results. The devices in this dissertation were modeled and designed using a COM model implemented in MATLAB®.

2.1 SAW Modeling Techniques

2.1.1 Delta Function Model

The delta-function model presented by Tancrell and Holland [14] is a very simplistic model and is based on superposition. In a SAW transducer the surface wave has an electric field intensity E associated with it due to the excitation at the transducer electrodes. The distribution of the time-varying electric field under adjacent electrodes is complex but in the delta-function model it is approximated to be normal to the piezoelectric surface. Adjacent electrodes have opposite

voltage polarity and opposite charge accumulation and since unlike charges attract, the charges on the electrodes migrate toward the edges [15]. This charge distribution that is concentrated mostly at the electrode edges can be modeled as delta-function source of the electric-field intensity at the electrode edges. Fig. 2.1 shows the delta-function modeling of the electric field distribution under the excited IDT, with sources at finger edges. Superposition is used to determine the total wave amplitude by summing the contribution from each of the electrodes. The waves are assumed to be unaffected by the electrodes they travel under and thus any effects of mass-loading, electrical shorting, and reflections are ignored.

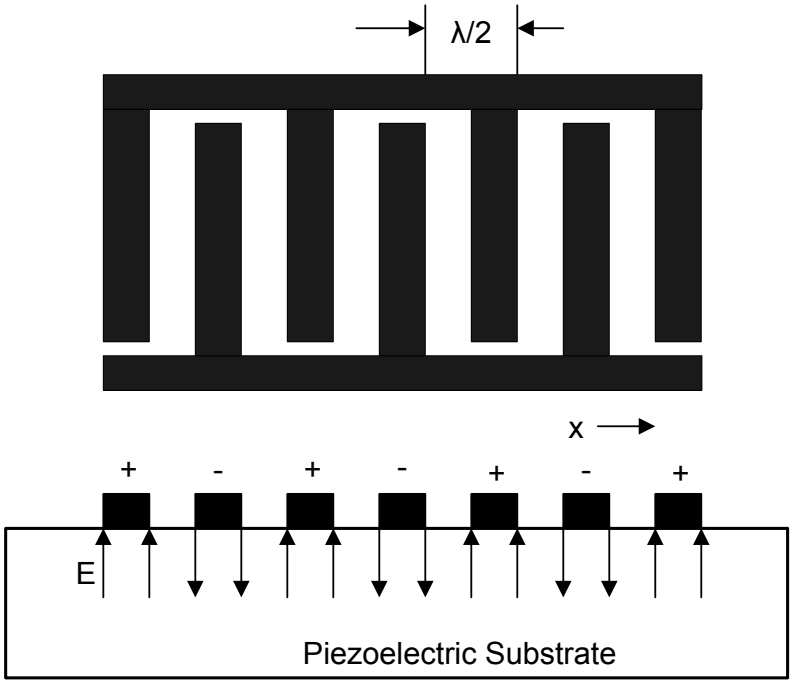

Figure 2.1: The delta-function modeling of the electric field distribution under the excited IDT, with sources at finger edges

2.1.2 Equivalent Circuit Model

The equivalent circuit model includes the interaction between the electric and acoustic energies of the piezoelectric device and was first derived by Mason [16, 17]. Fig. 2.2 is the equivalent circuit for a single electrode of an interdigital SAW transducer with impedance discontinuities between metallized and unmetallized regions. Each metal electrode of the transducer is represented by a three-port circuit that has two acoustic ports and an electrical port. For a transducer with N electrodes, the N sections are cascaded by connecting the acoustic ports in series and the electrical ports in parallel. The metallized and unmetallized regions of the transducer are represented by lumped element impedance discontinuities, similar to a transmission line. The acoustic medium is described by an equivalent circuit coupled to the electrical circuit by a transformer which is a function of the acoustic aperture and the electromechanical coupling coefficient of the piezoelectric substrate [18, 19, 15]. The model is very physical and includes reflections that occur at the edge of the electrodes and also includes the piezoelectric coupling effect. An electrode in a SAW reflector can also be represented using an equivalent circuit which is modeled as a transmission line with a periodic impedance mismatch. The details of this model are presented in Chapter 4, where enhancements to the current transmission line model are proposed to model reflectivity on YZ $LiNbO_3$ and the model coefficients are extracted and presented.

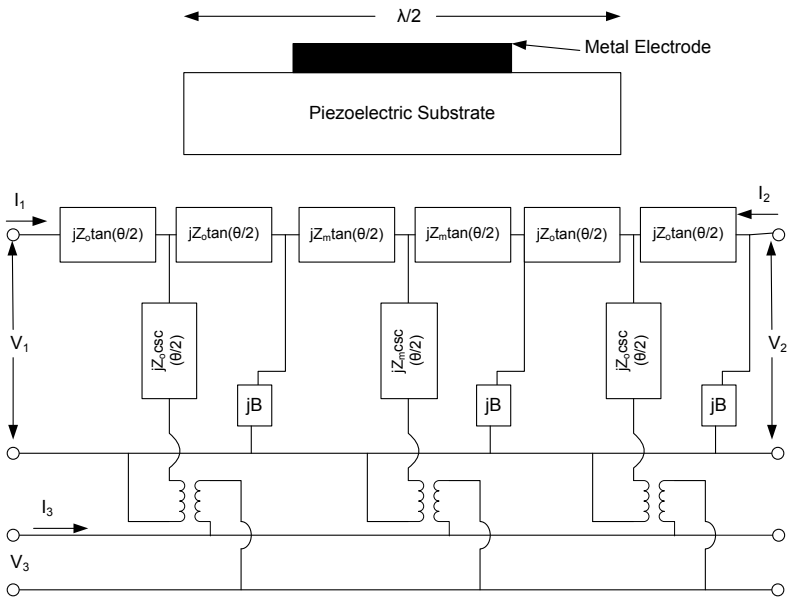

Figure 2.2: The equivalent circuit for a single electrode of an interdigital SAW transducer with impedance discontinuities between metallized and unmetallized regions.

2.1.3 Finite Element Method

The FEM approach is a numerical technique that requires a large amount of computations. In the FEM each electrode is divided into a number of elements and in each element the equations of elasticity are represented in a discrete form, yielding a set of simultaneous equations [20]. This method is extremely accurate, includes any dispersive effects and can predict the presence of other propagating modes. However, it is computationally intensive and simulations require excessive time as compared to the equivalent circuit model or coupling of modes model which will be discussed next.

2.1.4 Coupling of Modes Model

The coupling of modes (COM) approach has been used extensively since the 1950's in optics and electromagnetism to describe wave propagation through a periodically perturbed medium, or a structure with periodic geometry [21, 22]. The COM model was first applied to the SAW reflective gratings in 1980 by Haus and Wright [23]. Later, in 1985 Chen and Haus [24] expanded the model to include COM equations for SAW interdigitated transducers. The COM model enables precise and computationally efficient simulations of SAW devices. The surface acoustic waves are represented by a set of differential equations and the perturbations due to the presence of the electrodes are added into the differential equations to fully describe the wave propagation. The devices in this dissertation have been modeled using the COM model implemented in MATLAB®.

This chapter develops the first order differential equations as applied to a propagating SAW on a piezoelectric substrate assuming the waves are uncoupled and that there are no perturbations. In the next chapter the perturbations due to the electrodes will be included and the equations for each component, i.e. the reflector grating, the interdigital transducer and the free space delay will be developed.

2.2 Coupling of Modes Theory Review

The COM model applied to a surface acoustic wave, essentially describes the propagation of a Rayleigh wave moving through a piezoelectric substrate. The SAW can be represented as a scalar wave and the aperture of the transducer is assumed to be small enough so that no transverse modes are generated in the cavity, thus allowing for a one-dimensional analysis. The propagation of the SAW then satisfies the second order wave equation for a plane wave [25, 26]:

$$\frac{d^2u\left(x,t\right)}{dx^2} - \left(\frac{1}{v\left(x,\omega\right)^2}\right)\frac{d^2u\left(x,t\right)}{dt^2} = 0 \tag{2.1}$$

where $v(x,\omega)$ is the Rayleigh wave velocity. The COM equations can be expressed as first order wave equations. Consider two uncoupled modes on the surface of a piezoelectric substrate with metal electrodes as shown in Fig.2.3. The wave propagating to the right f(x,t) is the forward propagating mode, while the wave propagating to the left is the reverse propagating mode r(x,t). The surface wave can then be represented by the sum of the forward and reverse propagating

modes:

$$u(x,t) = f(x,t) + r(x,t) \tag{2.2}$$

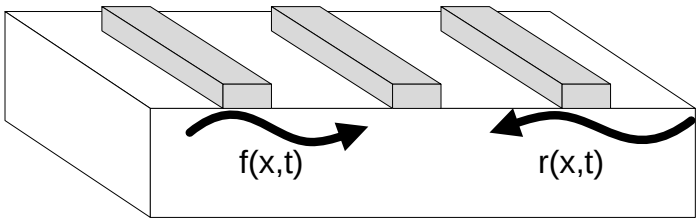

Figure 2.3: Propagation of waves on a piezoelectric substrate

The forward and reverse propagating modes are initially assumed to be uncoupled and their motion on the surface is assumed to be unperturbed by the presence of the electrodes. The perturbations due to the electrodes will be individually added to the first order differential wave equation later.

The first order wave equations for the forward and reverse waves are given by,

$$\frac{df(x,t)}{dx} = -\frac{1}{v_R(x,\omega)}\frac{df(x,t)}{dt} \tag{2.3}$$

$$\frac{dr(x,t)}{dx} = \frac{1}{v_R(x,\omega)}\frac{dr(x,t)}{dt} \tag{2.4}$$

The perturbations induced by the presence of the electrodes are frequency dependent and therefore the COM analysis will be considered in the frequency domain. The frequency domain form of equations (2.3) and (2.4) are found using the Fourier transform as:

$$\frac{dF(x,\omega)}{dx} = -jk_R(\omega)F(x,\omega) \tag{2.5}$$

$$\frac{dR(x,\omega)}{dx} = +jk_R(\omega)R(x,\omega) \tag{2.6}$$

where k_R is the SAW wave number and is defined as

$$k_R(\omega) = \frac{\omega}{v_R} \tag{2.7}$$

In the next chapter the COM equations for each component, i.e. the reflector, free space delay and transducer will be developed and their solutions shown; the cascaded P-matrices will be shown and harmonic operation modeling included.

CHAPTER 3
COUPLING OF MODES MODEL

This chapter shows the development of COM equations for each of the components of a SAW device, the reflector, the free space delay and the interdigital transducer. First, the reflector grating COM equations are derived and an electrical port is added to derive the transducer COM equations. The mixed P-matrix is developed and cascaded P-matrices for a one-port device and Y-parameters for a two-port device are shown. Additionally, the inclusion of the harmonic operation model is also developed. A coupling of modes model developed in MATLAB®has been used to model the devices.

3.1 Reflector COM Equations

In chapter 2 a forward and a reverse propagating wave, $F(x,\omega)$ and $R(x,\omega)$ were considered and the waves were assumed to be uncoupled to each other. However, the presence of the metal electrodes on the surface of the piezoelectric substrate introduces perturbations due to the electrical loading and mass loading which cause the waves to slow down. The impedance discontinuities due to the metal electrodes cause the incident waves to be partially reflected, thus causing the propagating modes to be coupled to each other as shown in Fig. 3.1. The variable *h* in Fig. 3.1

represents the thickness of the metal electrodes on the surface of the piezoelectric substrate, a is the electrode width and p is the period of the grating.

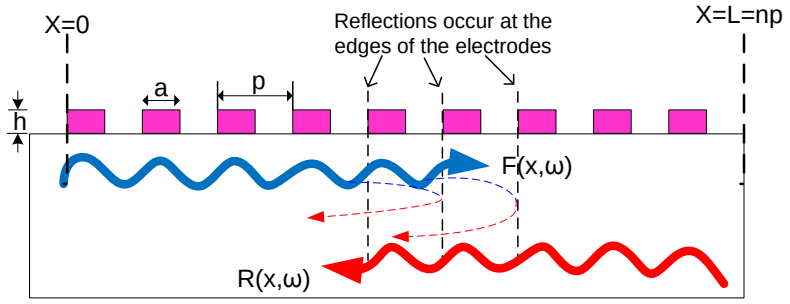

Figure 3.1: Propagation and coupling of Rayliegh waves in a SAW reflector grating due to the presence of metal electrodes

The effective velocity under the grating, $v_G(\omega)$, is the average velocity over one period of the reflector. It is frequency dependent and is related to an effective wave number $k_e(\omega) = \omega/v_G(\omega)$. This average velocity $v_G\left(\omega\right)$ under the reflector grating is a result of the mass loading $\Delta v_M\left(\omega\right)$, electrical shorting $\Delta v_E\left(\omega\right)$ and stored energy $\Delta v_{SE}\left(\omega\right)$ effects of the electrodes on the piezoelectric substrate and is defined as:

$$v_G\left(\omega\right) = v_R\left[1 + \frac{\Delta v_M\left(\omega\right)}{v_R} + \frac{\Delta v_E\left(\omega\right)}{v_R} + \frac{\Delta v_{SE}\left(\omega\right)}{v_R}\right] \tag{3.1}$$

The mathematical forms and the coefficients of the terms $\Delta v_M\left(\omega\right)$, $\Delta v_E\left(\omega\right)$ and $\Delta v_{SE}\left(\omega\right)$ in equation (3.1), for aluminum electrodes on YZ $LiNbO_3$ were determined from experimental data and the results are described in greater detail in Chapter 4.

Accounting for the perturbation under the grating the forward and reverse waves traveling through a reflector can be written as:

$$F(x,\omega) = \tilde{F}(x,\omega)\, e^{-jx(k_e-k_g)e^{-j\omega t}} \tag{3.2}$$

$$R(x,\omega) = \tilde{R}(x,\omega)\, e^{+jx(k_e-k_g)e^{j\omega t}} \tag{3.3}$$

where $\tilde{F}(x,\omega)$ and $\tilde{R}(x,\omega)$ are phasors representing the complex amplitudes of the waves and $k_g = \frac{\pi}{p}$ is the Bragg wave number associated with the reflector, and $p = \lambda/2$. A propagating surface wave is attenuated by phonon scattering, as well as coupling to longitudinal acoustic waves in air. This frequency dependent attenuation $\alpha(\omega)$ for YZ $LiNbO_3$ is given as [27]:

$$\alpha(\omega) = 0.19f + 0.88f^2 \tag{3.4}$$

The coupling of the forward to the reverse wave and the reverse to the forward wave, due to the reflections at the edges of the metal electrodes are represented by the reflection coefficients $\kappa_{21}(x,\omega)$ and $\kappa_{12}(x,\omega)$, respectively [25]. Including the wavenumber change, the attenuation coefficient and the reflection coefficients in equations (2.5) and (2.6), the complex amplitude wave equations can now be written as:

$$\frac{d\tilde{F}(x,\omega)}{dx} = -j\left[\delta(\omega) - j\alpha(\omega)\right]\tilde{F}(x,\omega) + j\kappa_{12}(x,\omega)\,\tilde{R}(x,\omega) \tag{3.5}$$

$$\frac{d\tilde{R}(x,\omega)}{dx} = j\left[\delta(\omega) - j\alpha(\omega)\right]\tilde{R}(x,\omega) - j\kappa_{21}(x,\omega)\,\tilde{F}(x,\omega) \tag{3.6}$$

where $\delta(\omega)$ is the detuning parameter and is defined as:

$$\delta(\omega) = k_e(\omega) - k_g \tag{3.7}$$

The relationship between the forward and reverse reflectivity coefficients $\kappa_{12}(x,\omega)$ and $\kappa_{21}(x,\omega)$ can be derived by considering the conservation of power. The periodic perturbations due to the presence of metal electrodes leads to an exchange of power between the forward propagating

$$\frac{d}{dx}\left|\tilde{F}(x,\omega)\right|^2 + \frac{d}{dx}\left|\tilde{R}(x,\omega)\right|^2 = 0 \tag{3.8}$$

In a lossy structure assuming no coupling between the waves, the forward and reverse traveling waves can be written as:

$$\tilde{F}(x,\omega) = F_o e^{-(jk+\alpha)x} \tag{3.9}$$

$$\tilde{R}(x,\omega) = R_o e^{+(jk+\alpha)x} \tag{3.10}$$

where F_o and R_o are the scalar amplitudes of the forward and reverse waves, respectively and k is the wave number. The change in power of these waves in a lossy medium is written as [28, 3]:

$$\frac{d}{dx}\left[\left|\tilde{F}\left(x,\omega\right)\right|^2\right] = -2\alpha F_o^2 e^{-2\alpha x} = -2\alpha\left|\tilde{F}\left(x,\omega\right)\right|^2 \tag{3.11}$$

$$\frac{d}{dx}\left[\left|\tilde{R}\left(x,\omega\right)\right|^2\right] = 2\alpha R_o^2 e^{2\alpha x} = 2\alpha\left|\tilde{R}\left(x,\omega\right)\right|^2 \tag{3.12}$$

From equations (3.8), (3.11), and (3.12):

$$|\tilde{F}(x,\omega)|^2 = |\tilde{R}(x,\omega)|^2 \tag{3.13}$$

From equations (3.5) and (3.6)the condition in equation (3.13) is satisfied when:

$$\kappa_{12}\left(x,\omega\right) = \kappa_{21}^*\left(x,\omega\right) \tag{3.14}$$

The coupling term κ_{12} for a periodic grating is given by a complex Fourier series [29, 25]:

$$\kappa_{12}\left(x,\omega\right) = \sum_n K\left(n,\omega\right) e^{jnk_g x} \tag{3.15}$$

Substituting in equations (3.5) and (3.6), the forward and reverse wave equations are:

$$\frac{d\tilde{F}(x,\omega)}{dx} = -j\left[\delta(\omega) - j\alpha(\omega)\right]\tilde{F}(x,\omega) + j\sum_{n} K(n,\omega)\,\tilde{R}(x,\omega)\,e^{j(n+1)k_g x} \tag{3.16}$$

$$\frac{d\tilde{R}(x,\omega)}{dx} = j\left[\delta(\omega) - j\alpha(\omega)\right]\tilde{R}(x,\omega) - j\sum_{n} K^*(n,\omega)\,\tilde{F}(x,\omega)\,e^{-j(n+1)k_g x} \tag{3.17}$$

In equations (3.5) and (3.6) only the fourier component with *n=-1* produces spatially independent coupling between the forward and reverse propagating waves, therefore all the other terms are discarded [29, 30, 31]. Rewriting equations (3.5) and (3.6):

$$\frac{d\tilde{F}(x,\omega)}{dx} = -j\left[\delta(\omega) - j\alpha(\omega)\right]\tilde{F}(x,\omega) + jK(\omega)\,\tilde{R}(x,\omega) \tag{3.18}$$

$$\frac{d\tilde{R}(x,\omega)}{dx} = j\left[\delta(\omega) - j\alpha(\omega)\right]\tilde{R}(x,\omega) - jK^*(\omega)\,\tilde{F}(x,\omega) \tag{3.19}$$

Using the condition $K(\omega) = K^*(\omega)$, and eliminating frequency dependence for simplicity equations(3.18) and (3.19) can be rewritten as:

$$\frac{d\tilde{F}(x)}{dx} = -j\Delta\tilde{F}(x) + jK\tilde{R}(x) \tag{3.20}$$

$$\frac{d\tilde{R}(x)}{dx} = -jK\tilde{F}(x) + j\Delta\tilde{R}(x) \tag{3.21}$$

where the variable $\Delta(\omega)$ is given as:

$$\Delta(\omega) = \delta(\omega) - j\alpha(\omega) \tag{3.22}$$

3.2 Solutions of the Reflector COM Equations

The solutions for these coupled equations can be found from the eigen vector and eigen values using equations (3.20) and (3.21) and is written as:

$$\tilde{F}(x) = C_1 e^{j\gamma x} + C_2 e^{-j\gamma x} \tag{3.23}$$

$$\tilde{R}(x) = C_1 e^{j\gamma x}\left(\frac{\gamma+\Delta}{K}\right) + C_2 e^{-j\gamma x}\left(\frac{-\gamma+\Delta}{K}\right) \tag{3.24}$$

where the new variable γ is called the propagation constant and is defined as:

$$\gamma = \sqrt{(\Delta)^2 - |K|^2} \tag{3.25}$$

The constants C_1 and C_2 in equations (3.23) and (3.24)are found by applying the following boundary conditions:

$$\tilde{F}(0) = 1 \tag{3.26}$$

$$\tilde{R}(L) = 0 \tag{3.27}$$

The constants C_1 and C_2 are found to be:

$$C_1 = \frac{(\gamma - \Delta) e^{-j\gamma L}}{2(\gamma cos(\gamma L) + j\Delta sin(\gamma L))} \tag{3.28}$$

$$C_2 = \frac{(\gamma + \Delta) e^{j\gamma L}}{2(\gamma cos(\gamma L) + j\Delta sin(\gamma L))} \tag{3.29}$$

The solutions for the forward and reverse propagating waves in a metallized grating on a piezoelectric substrate are then:

$$\tilde{F}(x) = \frac{\gamma cos[\gamma(L-x)] + j\Delta sin[\gamma(L-x)]}{\gamma cos(\gamma L) + j\Delta sin(\gamma L)} \tag{3.30}$$

$$\tilde{R}(x) = \frac{jKsin[\gamma(L-x)]}{\gamma cos(\gamma L) + j\Delta sin(\gamma L)} \tag{3.31}$$

The S-matrix of the reflector can then be written as:

$$[S] = \begin{bmatrix} R(0) & F(L) \\ F(L) & R(0) \end{bmatrix} = \begin{bmatrix} \frac{jKsin(\gamma L)}{\gamma cos(\gamma L) + j\Delta sin(\gamma L)} & \frac{(-1)^n \gamma}{\gamma cos(\gamma L) + j\Delta sin(\gamma L)} \\ \frac{(-1)^n \gamma}{\gamma cos(\gamma L) + j\Delta sin(\gamma L)} & \frac{jKsin(\gamma L)}{\gamma cos(\gamma L) + j\Delta sin(\gamma L)} \end{bmatrix} \quad (3.32)$$

The COM reflectivity parameter *K* is the reflection coefficient per wavelength and defined as:

$$K = \frac{f}{v_R} N \cdot r \quad (3.33)$$

where, *N* is the number of electrodes per wavelength and *r* is the reflectivity per electrode and is the result of the reflectivity contributions from three effects, the electrical shorting, the mass loading and the stored energy. The term *r*, is dependent on metalization ratio (ratio of electrode width to period of the reflector) and metal thickness. In order to fully characterize reflectivity of aluminum electrodes on YZ $LiNbO_3$ a least squares fit to experimental data over a large range of metalization ratios and metal thickness was performed. The extraction method, mathematical forms of the equations and the coefficients of each of the contributing terms are described in detail in Chapter 4

3.3 Transducer COM Equations and Solutions

When a voltage is applied across a transducer, SAW modes are excited due to the piezoelectric coupling; this process is called transduction. Shown in Fig. 3.2 is a uniformly weighted transducer

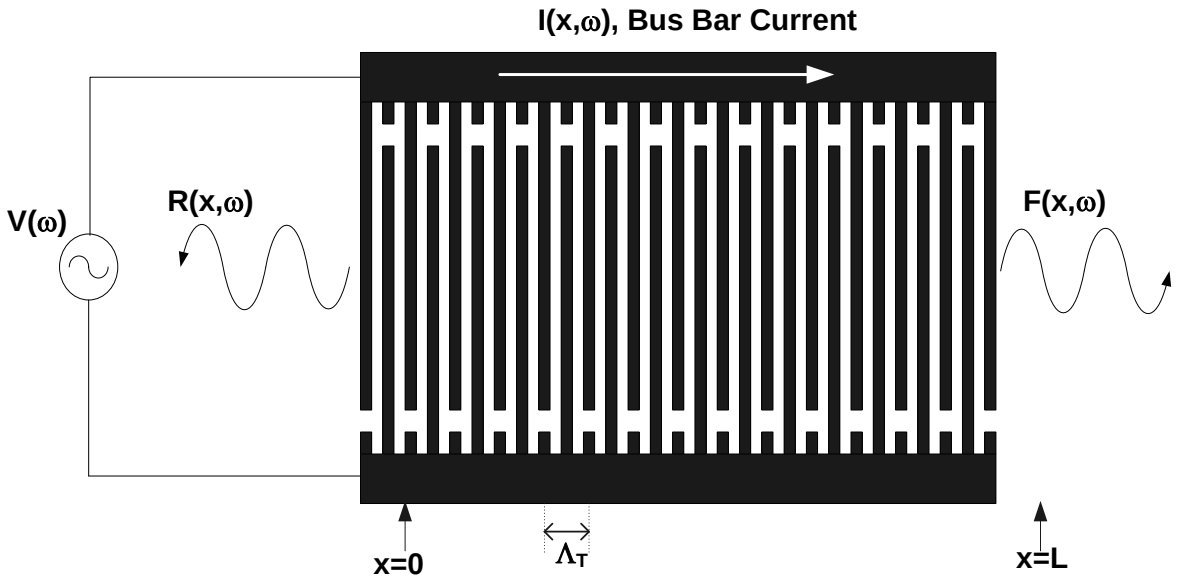

Figure 3.2: Schematic of an unweighted interdigital SAW transducer; forward and reverse propagating modes are launched when an external voltage is applied

that consists of a series of equal length electrodes with a periodicity of half the center frequency wavelength. The electrodes alternate between positive and negative polarities, with two electrodes per period. When a RF voltage is applied across this transducer a forward and a reverse propagating SAW launched. The COM differential equations for the transducer can be written using a similar analysis as the SAW reflector, however the inclusion of the third electrical port is required to model the transduction. A third equation is required to model the relationship between the applied RF voltage $V(\omega)$, the induced busbar current $I(x,\omega)$ and the transduction term ξ. The COM differential equations for the transducer are then written as [25, 26]:

$$\frac{d\tilde{F}(x,\omega)}{dx} = -j\Delta(\omega)\tilde{F}(x,\omega) + jK(\omega)\tilde{R}(x,\omega) + j\xi V(\omega) \tag{3.34}$$

$$\frac{d\tilde{R}(x,\omega)}{dx} = j\Delta(\omega)\,\tilde{R}(x,\omega) - jK^{*}(\omega)\,\tilde{F}(x,\omega) + j\xi^{*}V(\omega) \tag{3.35}$$

$$\frac{dI(x,\omega)}{dx} = -2j\xi^{*}(\omega)\,\tilde{F}(x,\omega) + 2j\xi(\omega)\,\tilde{R}(x,\omega) - j\omega CV(\omega) \tag{3.36}$$

where C is the capacitance of one pair of electrodes and $\xi(\omega)$ is the transduction coefficient. The detailed derivation of the transducer COM equation solutions are given by Abbott [25]. Abbott's solutions are used in the following section for the mixed matrix representation of the transducer.

3.3.1 SAW Transducer P-matrix Representation

The COM equations for the SAW transducer are expressed using two acoustic ports and an electrical port which requires the use of a mixed matrix in order to relate the acoustic and electrical terms. Fig. 3.3 is a schematic of the P-matrix definition of a SAW transducer. The variables at the electrical port are the applied voltage and the induced current, while the variables at the two acoustic ports are the amplitudes of the incident and reflected waves, a_n and b_n according to the scattering matrix representation. This combination of the S-matrix and Y-matrix allows for easy cascading of adjacent acoustic components.

As shown by Tobolka [32], the P-matrix representation of a SAW transducer is:

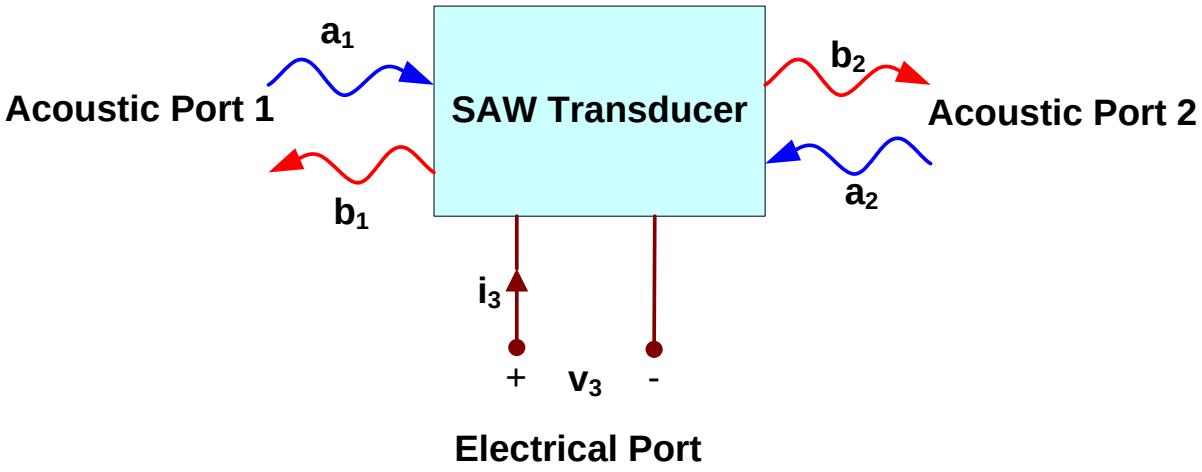

Figure 3.3: Schematic showing the acoustic and electrical ports of a SAW transducer which are represented using a mixed P-matrix

$$\begin{bmatrix} b_1 \\ b_2 \\ i_3 \end{bmatrix} = \begin{bmatrix} P_{11} & P_{12} & P_{13} \\ P_{21} & P_{22} & P_{23} \\ P_{31} & P_{32} & P_{33} \end{bmatrix} \begin{bmatrix} a_1 \\ a_2 \\ v_3 \end{bmatrix} \tag{3.37}$$

The terms P_{11}, P_{12}, P_{21} and P_{22} are the reflection and transmission parameters in the case where the electrical port is shorted. This condition is analogous to a SAW reflector grating and the terms can be represented by the scattering matrix of the SAW reflector which was derived in section 3.2. The term P_{33} is the admittance of the transducer seen at the electrical port when the amplitudes of the incident waves is zero $(a_1 = a_2 = 0)$ and has units of Ω^{-1}. The terms P_{13}, P_{23}, P_{31} and P_{32} are the voltage to SAW transfer parameters and have units of $\Omega^{-0.5}$. In the case of a lossless transducer, due to the conservation of power flow,

$$|P_{13}|^2 + |P_{23}|^2 = \frac{1}{2} Re\left(P_{33}\right) \tag{3.38}$$

Additionally, in a unweighted SAW transducer the two acoustic ports are identical, yielding a reciprocal device. In a reciprocal device it can be shown that

$$P_{12} = P_{21} \tag{3.39}$$

$$2P_{13} = -P_{31} \tag{3.40}$$

$$2P_{23} = -P_{32} \tag{3.41}$$

As mentioned earlier, terms P_{11}, P_{12}, P_{21} and P_{22} for the transducer are identical to the SAW reflector S-matrix terms and given the equations (3.39), (3.40) and (3.41) only three unknown terms remain. As derived by Abbott [25], these terms are:

$$P_{13} = jL \frac{sin\left(\frac{\gamma L}{2}\right)}{\frac{\gamma L}{2}} \frac{\xi^* \gamma cos\left(\frac{\gamma L}{2}\right) + j\left(K^* \xi + \Delta\right) sin\left(\frac{\gamma L}{2}\right)}{\gamma cos\left(\gamma L\right) + j\Delta sin\left(\gamma L\right)} \tag{3.42}$$

$$P_{23} = jL\left(-1\right)^n \frac{sin\left(\frac{\gamma L}{2}\right)}{\frac{\gamma L}{2}} \frac{\xi^* \gamma cos\left(\frac{\gamma L}{2}\right) + j\left(K^* \xi + \Delta\right) sin\left(\frac{\gamma L}{2}\right)}{\gamma cos\left(\gamma L\right) + j\Delta sin\left(\gamma L\right)} \tag{3.43}$$

$$
\begin{aligned}
P_{33} = & -j2\left[\frac{K^*\xi^2 + K\xi^{*2} + 2\Delta\left|\xi\right|^2}{\gamma^3}\right]\left[\gamma L - \frac{\gamma sin\left(\gamma L\right) + j\Delta\left(1 - cos\left(\gamma L\right)\right)}{\gamma cos\left(\gamma L\right) + j\Delta sin\left(\gamma L\right)}\right] \\
& - 2\left[\frac{\Delta\left(K\xi^{*2} + K^*\xi^2\right) + 2\left|K\right|^2\left|\xi\right|^2}{\gamma^3}\right]\left[\frac{1 - cos\left(\gamma L\right)}{\gamma cos\left(\gamma L\right) + j\Delta sin\left(\gamma L\right)}\right] \\
& + j\left[\frac{3\omega C_f L}{\Gamma_t\left(3 + j\omega C_f R_f\right)}\right]
\end{aligned} \tag{3.44}
$$

where, L is the length of the SAW transducer, Λ_T is the transduction period and C_f and R_f are the electrode capacitance and resistance.

3.3.2 The Transduction Parameter

The transduction term is a measure of the conversion of electrical energy to acoustical energy that takes place in the transducer. The transduction term can be derived by comparing the voltage to SAW transfer parameter P_{13}, with reflectivity set to zero in the COM model to the same term derived for the impulse response model, where the all the electrodes are assumed to be non-reflective. The P_{13} element in the impulse response model is given as [14, 20]:

$$
P_{13} = j\left|k_R\right|\sqrt{\frac{\omega W\Gamma_s}{2}}\epsilon_s V_F\left(k_R\right)\left(\frac{sin\left(\frac{\Delta L}{2}\right)}{sin\left(\frac{\Delta\Lambda_T}{2}\right)}\right)e^{\frac{-j(k_R - k_o)L}{2}} \tag{3.45}
$$

The P_{13} element in the COM model with reflectivity set to zero is given as:

$$P_{13} = j\xi(\omega) L \left(\frac{sin\left(\frac{\Delta L}{2}\right)}{sin\left(\frac{\Delta \Lambda_T}{2}\right)} \right) e^{\frac{-j(k_R - k_o)L}{2}} \tag{3.46}$$

Comparing equations (3.45) and (3.46), the transduction term can be equated to:

$$\xi(\omega) = |k_R| \epsilon_s \frac{V_F(k_R)}{\Lambda_T} \sqrt{\frac{\omega W \Gamma_s}{2}} e^{j\phi_T} \tag{3.47}$$

where, k_R is the wave number, ϵ_s is the electrostatic permittivity.

3.4 Harmonic Modeling

A given SAW transducer will respond at only certain harmonic frequencies which are related to the periodicity of the electrodes. In order to understand the harmonic modeling it is essential to look at the array factor and the element factor of the transducer which contribute to the acoustic conductance. The acoustic conductance of a transducer is given by:

$$G_a(\omega) = \omega W \Gamma_s |V_e(k_R)|^2 \tag{3.48}$$

where, *W* is the transducer aperture width, Γ_s is the SAW coupling coefficient, $V_e(k_R)$ is the electrostatic charge density of the transducer and k_R is the wave number. Γ_s, the SAW coupling coefficient defined by Morgan [20] is:

$$\Gamma_s \approx \frac{1}{\epsilon_s}\frac{v_f - v_m}{v_f} = \frac{k^2}{2\epsilon_s} \tag{3.49}$$

v_f and v_m are the free surface and metallized surface surface wave velocities and k^2 is known as the surface wave piezoelectric coupling constant. The electrostatic charge density of the transducer is the product of three fourier transforms; $A_1(k_R)$, the array factor for one period of the transducer, $A_N(k_R)$, the part of the array factor that gives the repetition for N periods and $V_f(k_R)$, the fourier transform of the electrostatic charge density of the transducer is given as [20]:

$$V_e\left(k_R\right) = A_1\left(k_R\right) * A_N\left(k_R\right) * V_f\left(k_R\right) \tag{3.50}$$

In case of a uniform transducer the array factor is dependent on the number of electrodes per wavelength, S_e. There are three types of commonly used uniform transducers, $S_e = 2$, indicating 2 electrodes per wavelength and each electrode has a width of $\lambda/4$, $S_e = 3$, indicating 3 electrodes per wavelength and each electrode has a width of $\lambda/6$, and $S_e = 4$, indicating 4 electrodes per wavelength and each electrode has a width of $\lambda/8$. It has been shown [20] that for a transducer with N periods the array factor can be written as:

$$A_1\left(\beta\right) * A_N\left(\beta\right) = \begin{cases} \dfrac{sin\left(N\beta pS_e/2\right)}{sin\left(\beta pS_e/2\right)} & \text{for } S_e\text{=2 or 3} \\ 2cos\left(\beta p/2\right)\dfrac{sin\left(N\beta pS_e/2\right)}{sin\left(\beta pS_e/2\right)} & \text{for } S_e = 4 \end{cases} \tag{3.51}$$

where β is a multiple of the wave number that corresponds to the harmonic of operation. For S_e=2 or 3, the array factor in equation (3.51) has maxima when $\beta = 2\pi M/pS_e$, with *M=0,1,2,...* and *M* is the harmonic of operation and $M\omega_c$ being the harmonic frequency. However, the transducers do not respond at all harmonics due to the fourier transform elemental charge density $V_f(k)$ from equation (3.50). The fourier transform of the elemental charge density of the transducer, $V_f(\beta)$, known as the element factor of the transducer was derived by Peach [33] and Datta and Hunsinger [34] and is given by

$$V_f(\beta) = \epsilon \frac{2sin\pi s}{P_s\left(-cos\frac{\pi a}{p}\right)} P_m\left(cos\frac{\pi a}{p}\right), \quad for\ m \leq \frac{\beta p}{2\pi} \leq m+1 \tag{3.52}$$

where $s = \frac{\beta p}{2\pi} - m$, so that $0 \leq s \leq 1$ and $P_s\left(-cos\frac{\pi a}{p}\right)$ is a Legendre function and $P_m\left(cos\frac{\pi a}{p}\right)$ is a Legendre polynomial. The variable *a*, is the width of the metal electrode and *p*, is the period of the transducer. The Legendre function and the Legendre polynomial are evaluated using a series expansion given in Morgan [20]. $V_f(\beta)$ is zero at the sampling frequency f_s of the transducer and multiples of f_s. This is because at frequency f_s, the potential of the wave has the same periodicity as that of the electrodes, so the electrodes will all have the same voltage and no current is induced. Therefore, for the case where S_e=2, harmonics with *M=2,4,6,..* are absent because $V_f(k)$*=0* at these points. In addition for S_e*=2*, the third harmonic is absent if *a/p=1/2*. Similarly, for S_e*=3* the harmonics where *M* is a multiple of 3 do not exist. For S_e*=4* the array factor has a cosine term (shown in equation (3.51)), therefore the harmonics with *M=2,6,10,..* are suppressed and only harmonic responses for odd values of *M* occur.

For the reflector the reflectivity, *r*, and grating velocity, v_G, versus the metallization ratio and the normalized metal thickness at second harmonic operation were extracted experimentally. A least squares fit to the data was then used to extract coefficients to the mathematical forms of the equations. The extraction methodology, the mathematical forms of the equations and the coefficients are discussed in detail in Chapter 4.

3.5 Cascading of P-Matrices

From section (4.3), the P-matrix of the transducer can be defined in terms of its' S-parameters, admittance, and voltage to SAW transfer parameters as

$$P_{transducer} = \begin{bmatrix} S_{11} & S_{12} & P_{13} \\ S_{21} & S_{22} & P_{23} \\ P_{31} & P_{32} & Y \end{bmatrix} \tag{3.53}$$

The S-parameters represent the transducer when the electrical port is shorted and Y is the input admittance of the transducer. For a SAW reflector there is no electrical port, therefore all the terms related to the third port are zero. The P-matrix for the SAW reflector is:

$$P_{reflector} = \begin{bmatrix} S_{11} & S_{12} & 0 \\ S_{21} & S_{22} & 0 \\ 0 & 0 & 0 \end{bmatrix} \tag{3.54}$$

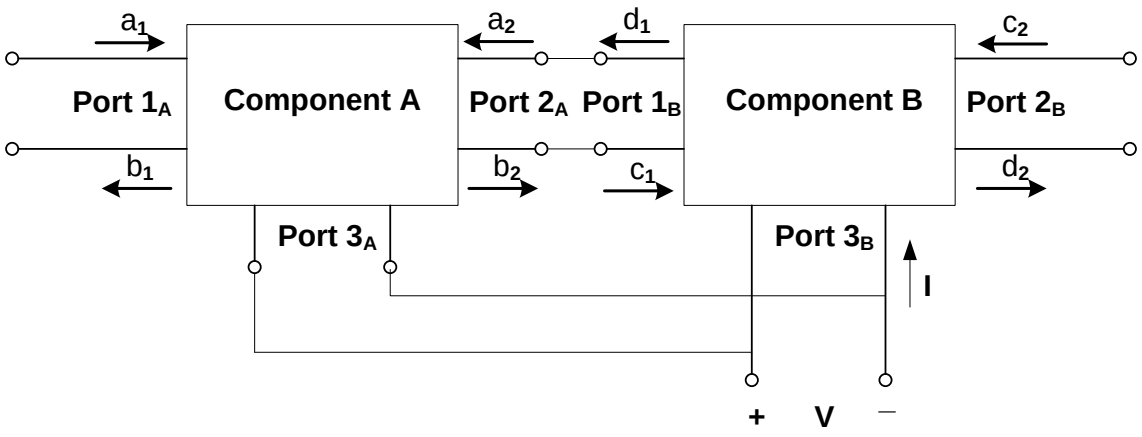

Figure 3.4: Schematic showing the cascading of two adjacent components in a one-port SAW device. The electrical ports are in parallel and the acoustic ports are in series.

For a free-space delay of length L, it's electrical length can be written as $k_o L$. There are no acoustic reflections ant the third electrical port is non-existent, therefore the P-matrix for a free-space delay is defined as:

$$P_{delay} = \begin{bmatrix} 0 & e^{-jk_oL} & 0 \\ e^{-jk_oL} & 0 & 0 \\ 0 & 0 & 0 \end{bmatrix} \tag{3.55}$$

Using the P-matrix of these acoustic components, it is possible to simulate different types of SAW devices, once the appropriate matrix cascade equations are derived.

3.5.1 One-Port P-Matrix Cascade

A typical SAW device consists of multiple acoustic components. In order to simulate the frequency response of the entire device it is necessary to link the individual components together by cascading the P-matrices of adjacent components iteratively. As shown in Fig. 3.4, in the case of a one-port device, the electrical ports of adjacent components are in parallel while their acoustic ports are in series. The equations for cascading two adjacent components can be derived by converting the P-matrices of individual components to a transmission matrix, finding the product of T-matrix of two adjacent components and then converting the solution back to P-matrix form [35]. Another method is to draw a signal flow graph for the two adjacent components and then use Mason's gain formula to find the cascaded P-matrix of two adjacent components [3]. The cascaded P-matrix equations for two adjacent components have been derived previously and are given below for completeness.

$$P_{11} = \frac{b_1}{a_1} = P_{11}^A + P_{11}^B \left[\frac{P_{21}^A P_{12}^A}{1 - P_{11}^B P_{22}^A} \right] \tag{3.56}$$

$$P_{12} = \frac{b_1}{c_2} = \frac{P_{12}^A P_{12}^B}{1 - P_{11}^B P_{22}^A} \tag{3.57}$$

$$P_{13} = \frac{b_1}{V} = P_{13}^A + P_{12}^A \left[\frac{P_{13}^B + P_{11}^B P_{23}^A}{1 - P_{11}^B P_{22}^A} \right] \tag{3.58}$$

$$P_{21} = \frac{d_2}{a_1} = \frac{P_{21}^A P_{21}^B}{1 - P_{11}^B P_{22}^A} \tag{3.59}$$

$$P_{22} = \frac{d_2}{c_2} = P_{22}^B + P_{22}^A \left[\frac{P_{12}^B P_{21}^B}{1 - P_{11}^B P_{22}^A} \right] \tag{3.60}$$

$$P_{23} = \frac{d_2}{V} = P_{23}^B + P_{21}^B \left[\frac{P_{23}^A + P_{22}^A P_{13}^B}{1 - P_{11}^B P_{22}^A} \right] \tag{3.61}$$

$$P_{31} = \frac{I}{a_1} = P_{31}^A + P_{21}^A \left[\frac{P_{31}^B + P_{11}^B P_{32}^A}{1 - P_{11}^B P_{22}^A} \right] \tag{3.62}$$

$$P_{32} = \frac{I}{c_2} = P_{32}^B + P_{12}^B \left[\frac{P_{32}^A + P_{22}^A P_{31}^B}{1 - P_{11}^B P_{22}^A} \right] \tag{3.63}$$

$$P_{33} = \frac{I}{V} = P_{33}^A + P_{33}^B + P_{32}^A \left[\frac{P_{13}^B + P_{11}^B P_{23}^A}{1 - P_{11}^B P_{22}^A} \right] + P_{31}^B \left[\frac{P_{23}^A + P_{22}^A P_{13}^B}{1 - P_{11}^B P_{22}^A} \right] \tag{3.64}$$

The equations are further simplified when one or both of the cascaded components is a reflector or a delay since the elements associated with the third electrical port for these components can be eliminated. A SAW device with numerous components that are acoustically in series and electrically in parallel can be simulated by using equations (3.56) to (3.64) iteratively. The cascade equations for a two-port device whose electrical ports are isolated are shown in the next section.

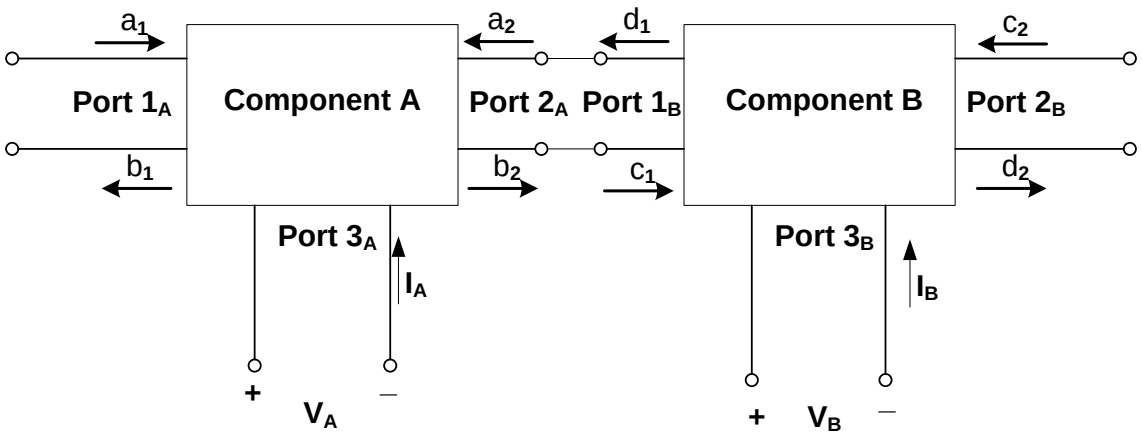

Figure 3.5: Schematic showing the cascading of of a two-port SAW device. The two electrical ports are isolated and the acoustic ports are in series.

3.5.2 Two-Port P-Matrix Cascade

In a two port device, as shown in Fig. 3.5, the acoustic ports are connected in series through a delay, however, the electrical ports are now isolated. In order to find the P-matrix solution of the entire device, first, each transducer is cascaded to its adjacent reflectors or delays that do not contain the third electrical port. Next, the resulting one-port cascaded P-matrices are now converted to an equivalent two port admittance matrix. The final resulting admittance matrix is:

$$[Y] = \begin{bmatrix} \frac{I_A}{V_A} & \frac{I_A}{V_B} \\ \frac{I_B}{V_A} & \frac{I_B}{V_B} \end{bmatrix} = \begin{bmatrix} P_{33}^A + \frac{P_{23}^A P_{32}^A P_{11}^B e^{-j2kL}}{1 - P_{22}^A P_{11}^B e^{-j2kL}} & \frac{P_{13}^B P_{32}^A e^{-jkL}}{1 - P_{22}^A P_{11}^B e^{-j2kL}} \\ \frac{P_{23}^A P_{31}^B e^{-jkL}}{1 - P_{22}^A P_{11}^B e^{-j2kL}} & P_{33}^B + \frac{P_{13}^B P_{31}^B P_{22}^A e^{-j2kL}}{1 - P_{22}^A P_{11}^B e^{-j2kL}} \end{bmatrix} \tag{3.65}$$

Various SAW device embodiments can be simulated using the cascading of appropriate P-matrices.

CHAPTER 4
MODELING OF SAW REFLECTOR COM PARAMETERS FOR ALUMINUM ELECTRODES ON YZ LITHIUM NIOBATE

Material choice for SAW device applications is based on material properties such as SAW velocity, electromechanical coupling constant k^2, temperature coefficient of delay (TCD), diffraction effects, temperature range of operation, and coupling to unwanted bulk waves. The SAW velocity determines the wavelength at a given frequency and therefore the device size. The electromechanical coupling coefficient is a measure of the efficiency of a given piezoelectric substrate in converting an applied electrical signal into mechanical energy associated with the SAW. TCD of a material relates to the change in delay of a SAW device over temperature. Table 4.1 shows a comparison of some of the material properties for commonly used single crystal surface-wave materials for SAW applications. High coupling coefficient and large TCD translate to large fractional bandwidths and higher sensitivity to changes in temperature which are both required for the spread-spectrum devices in this dissertation. YZ Lithium Niobate ($LiNbO_3$) has a high coupling

Table 4.1: Material Properties For Typical Single Crystal SAW Materials

Material	Free Surface Velocity (m/s)	Coupling Constant $k^2(\%)$	TCD (ppm/^{o}C)	Maximum Temperature (^{o}C)	Reference
YZ-$LiNbO_3$	3488	4.8	94	350	[36]
128^{o}YX-$LiNbO_3$	3979	5.4	75	350	[37]
ST-X Quartz	3159	0.16	0	573	[38, 39]
Langasite	2730	0.32	0	1000	[38, 40]

coefficient, a high TCD, and very low diffraction which make it an ideal choice for a temperature sensor. 128^o YX $LiNbO_3$ has similar properties however, diffraction is much higher and therefore it was not chosen as a primary material for the sensors in this dissertation. In order to accurately simulate the SAW devices on YZ $LiNbO_3$ using the COM model discussed in the previous chapter it was necessary to extract the reflectivity and velocity on YZ $LiNbO_3$. A thorough characterization of the reflectivity and velocity on YZ $LiNbO_3$ was conducted at both fundamental and second harmonic operation. In this chapter the reflector COM parameters that were experimentally extracted for aluminum electrodes on YZ $LiNbO_3$ are discussed. The details of the extraction methodology, the mathematical forms of the equations derived using the transmission line model for a SAW grating and the coefficients extracted are presented.

The devices are currently built using aluminum reflectors having $\frac{1}{2}$ wavelength period, for fundamental harmonic operation. To increase the device operation frequency for a given line-width, devices employing harmonic operation of the transducer and reflector must be used. It was found that experimental data did not fit well with often quoted models and theoretical predictions for fundamental reflectivity. Reflectivity and velocity data for shorted and open aluminum grating reflectors on YZ $LiNbO_3$, at both fundamental and second harmonic operation are presented. To completely characterize the reflectivity and grating velocity, the data was extracted over a metallization ratio ranging from 0.2 to 0.9 and a normalized metal thickness ranging from 0.4% to 4%. The data were then fit to a new modified transmission line model extended from that presented by Li and Melngailis [41] and Wright [42], yielding model parameters that are represented by the physical structure. The data curve-fits yield the coefficients for the new modified transmission

line model that are used to predict reflectivity of aluminum gratings on YZ $LiNbO_3$ for a given metallization ratio and normalized metal thickness at fundamental or second harmonic operation. The derived equations were then used in the COM model simulation of frequency coded reflector devices on YZ $LiNbO_3$ presented in this dissertation.

4.1 Experimental Extraction of SAW Reflectivity and Grating Velocity

4.1.1 Test Device Structure

Delay line devices with either shorted or open reflectors, as shown in Fig. 4.1, were used to extract aluminum grating reflectivity [42, 43]. The reflectors consisted of 25 electrodes and were located 70 wavelengths away from the delay line. The transducers were 18 wavelengths long and were spaced 40 wavelengths apart. The transducer employed $\frac{1}{6}$ wavelength electrodes which provided both fundamental and second harmonic data from a single device. The devices had varying center frequency wavelengths of $16\mu m$, $24\mu m$ and $32\mu m$, and many sets of devices were fabricated with varying metal thicknesses to provide a range of variation in normalized metal thickness from 0.4% to 2% for fundamental operation and 0.8% to 4% for second harmonic operation. Additionally, for each center frequency wavelength, several devices for each open circuit and short circuit gratings were fabricated with grating metallization ratios ranging from 0.2 to 0.9. Table 4.2 shows the device variations used for parameter extraction. This provides a large number of data points as a function of a/p and h/λ necessary to extract the physical model parameters.

Table 4.2: Device Variations Used For Reflectivity Extraction

Device Wavelength (μm)	Metallization Ratio (a/p)	Harmonic of Operation	Metal Thickness (A^o)	Normalized Metal Thickness (h/λ)
16	0.2 to 0.9	First	1200	0.75%
24	0.2 to 0.9	First	1200	0.5%
32	0.2 to 0.9	First	1200	0.38%
8	0.2 to 0.9	Second	1200	1.5%
12	0.2 to 0.9	Second	1200	1.0%
16	0.2 to 0.9	Second	1200	0.75%
16	0.2 to 0.9	First	2400	1.5%
24	0.2 to 0.9	First	2400	1.0%
32	0.2 to 0.9	First	2400	0.75%
8	0.2 to 0.9	Second	2400	3.0%
12	0.2 to 0.9	Second	2400	2.0%
16	0.2 to 0.9	Second	2400	1.5%
16	0.2 to 0.9	First	3200	2.0%
24	0.2 to 0.9	First	3200	1.3%
32	0.2 to 0.9	First	3200	1.0%
8	0.2 to 0.9	Second	3200	4.0%
12	0.2 to 0.9	Second	3200	2.67%
16	0.2 to 0.9	Second	3200	2.0%

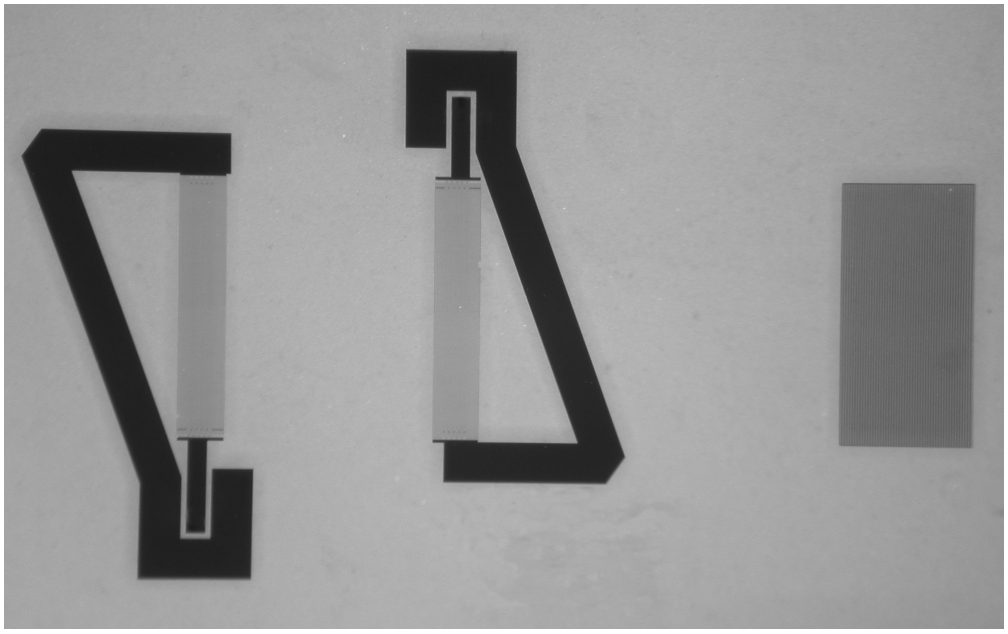

Figure 4.1: Delay line with reflector for obtaining reflectivity measurements. Transducers contain $\frac{1}{6}$ wavelength electrodes, providing for both fundamental and second harmonic operation using a single device.

4.1.2 Method of Reflectivity and Velocity Extraction

Transmission S_{21} responses of the delay line devices were used to extract reflectivity and the S_{21} frequency response was converted to time domain by performing an inverse FFT. Typical S_{21} frequency and time domain responses for the delay line and reflector structure are shown in Fig. 4.2 and Fig. 4.3 respectively. The reflector response appears as a ripple in the pass band of the delay line frequency response. The time domain reflector response and delay line response were gated out individually and converted to the frequency domain using an FFT. The time domain reflector response was normalized by the delay line response to eliminate effects of its loss and transfer function effects, similar to [42].

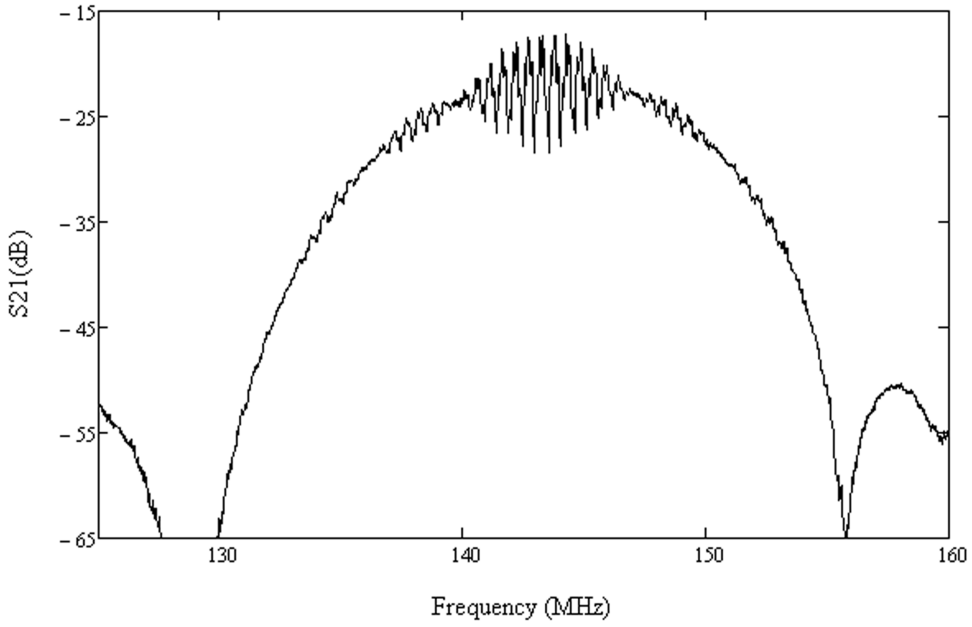

Figure 4.2: Experimental (S_{21}) frequency response from device structure in Fig.4.1. The reflector response appears as a ripple in the pass band of the delay line response.

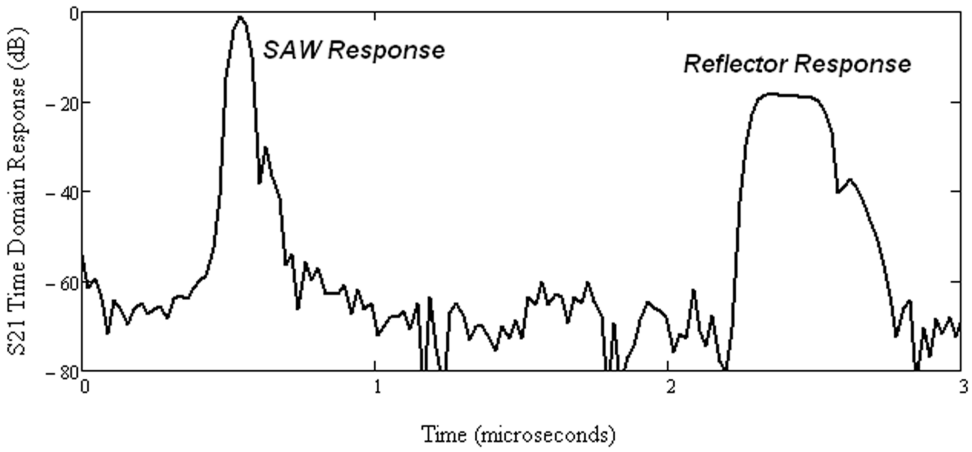

Figure 4.3: Delay line with reflector (S_{21}) time response. The direct SAW time response appears first followed by the reflector response. The energy in the reflector's trailing edge time response is a result of inter-electrode reflections that decay later in time.

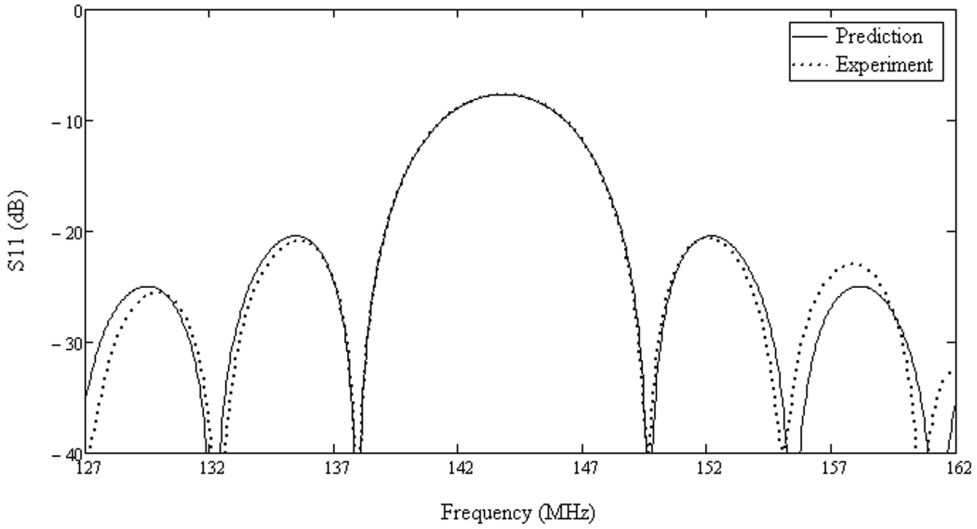

Figure 4.4: SAW grating (S_{21}) frequency response for a shorted grating with 25 electrodes. Solid line is COM model predicted grating response, and dotted line is experimentally extracted grating response. The extraction technique minimizes differences between the main passband of the experimental and predicted responses.

Reflectivity per electrode was obtained by minimizing the integral squared error between the experimental and the COM model predicted reflector response over the reflector's main passband. Fig. 4.4 shows a typical SAW grating frequency response, where the dotted line is the predicted COM model response and the solid line is the experimentally extracted response. Since the center frequency wavelength of the grating is known, the grating velocity information is extracted from the frequency at the point of maximum reflectivity in the grating frequency response.

4.2 Existing Transmission Line Model

As the SAW propagates under a grating, the wave is perturbed by the presence of electrodes. As the wave propagates under an electrode on a piezoelectric substrate, the presence of the electrode

creates an impedance and velocity discontinuity due to two effects. One effect is the mechanical loading due to the mass of the metal electrode and the other is the electrical loading effect which is effectively a shorting of the associated electric field of the surface wave under the electrode. These effects are modeled by a transmission line with a series of stepped impedance and velocity discontinuities. There is additionally a stored energy effect that results due to the energy stored in higher-order non-propagating, evanescent components of the wave which is modeled by a lumped susceptance element [41] as shown in Fig. 4.5. This transmission line model for a SAW reflector

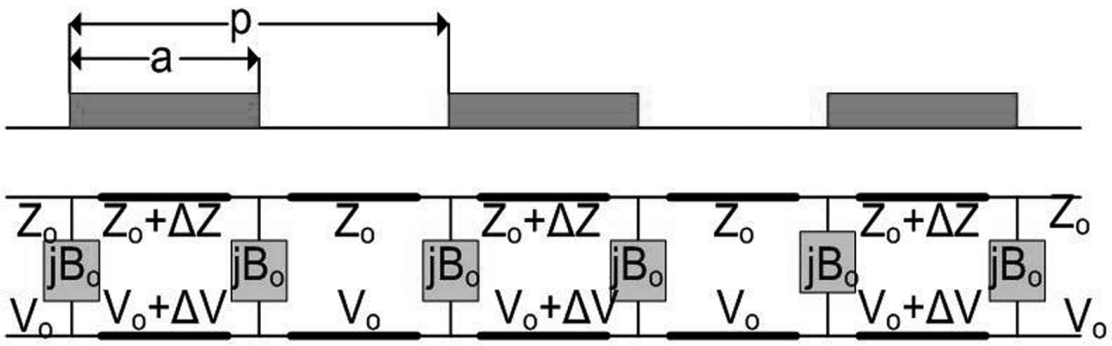

Figure 4.5: Transmission line representation of a SAW reflector. The perturbation introduced by the grating is represented as a series of stepped impedance and velocity discontinuities. The susceptance element represents the stored energy parameter.

was later modified by Wright [42] to introduce a sine dependence of the lumped element term on the metallization ratio and is given as:

$$r = j\left\{\left[\left(\frac{\Delta Z}{Z_o}\right) + \left(\frac{a}{p}\cdot\frac{\Delta Z_1}{Z_o}\right)\right] sin\left(\frac{2\pi a}{Np}\right) - \frac{B_o}{Y_o} sin\left(\frac{\pi a}{p}\right) cos\left(\frac{2\pi a}{Np}\right)\right\} \tag{4.1}$$

$$v = v_o \left[1 + \frac{a}{p} \left(\frac{\Delta v}{v_o} \right) - \left(\frac{N}{2\pi} \right) \left(\frac{B_o}{Y_o} \right) \sin \left(\frac{a}{p} \pi \right) \right] \tag{4.2}$$

where, *a/p* is the metallization ratio, (i.e. ratio of electrode width to period of the grating) and *N* is the number of electrodes per wavelength of the grating. For fundamental operation *N=2*, (i.e. two electrodes per wavelength of the grating), and at second harmonic operation *N=1*, (i.e. one there is only one electrode per wavelength of the grating). Equation (1) was used to fit the grating reflectivity, *r*, where $\Delta Z/Z_o$ is the mechanical loading parameter, and $\Delta Z_1/Z_o$ is the piezoelectric shorting parameter. Equation (2) was used to fit the velocity, v, under the grating, v_o is the free surface velocity, $\Delta v/v_o$ is the fractional change in velocity as the wave propagates under the grating, and B_o/Y_o represents the normalized susceptance term.

As a comparison, shown in Fig. 4.6, are plots of reflectivity versus a/p for a measured data set, predictions based on Wright's model [42] and perturbation theory from Datta [1]. The measured data fits the general shape of the perturbation theory, but the peak reflectivity is lower (this was found for all data sets). Equation (4.1) for reflectivity does not fit the extracted data well versus a/p. Wright's model is an approximation to the measurements, but the actual shape has quite a large error for much of the data set.

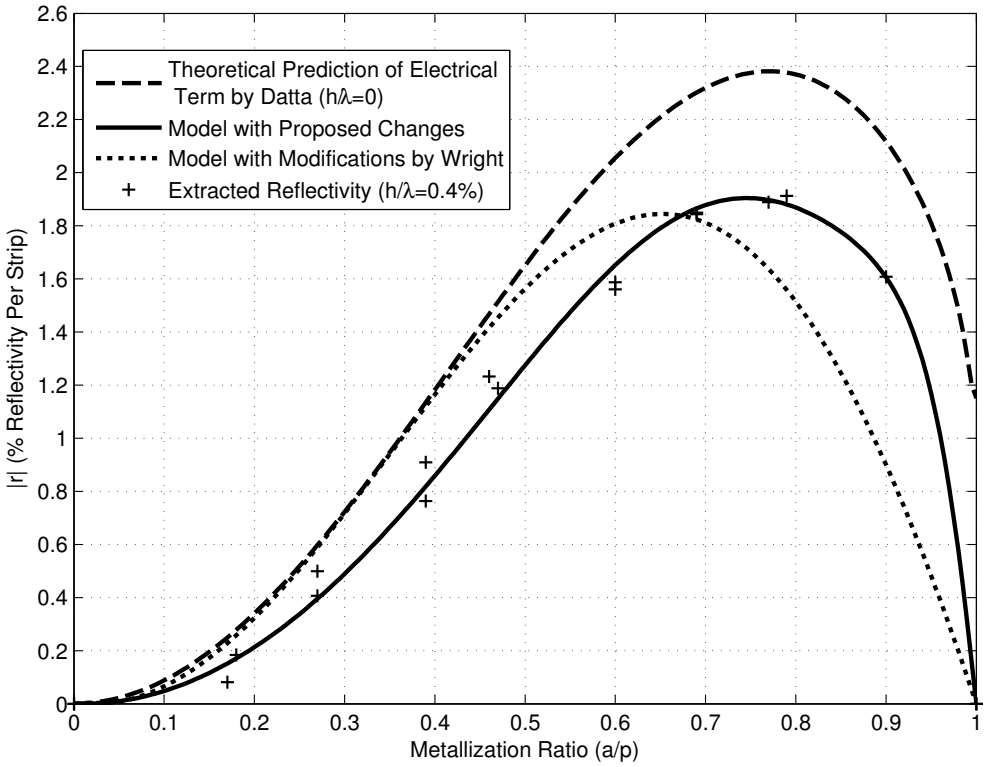

Figure 4.6: Percent reflectivity per strip versus metallization ratio for an open grating at first harmonic operation. Shown in the dashed curve is the prediction of the electrical term for $h/\lambda = 0$ using perturbation theory given by Datta [1]. The dotted curve shows the fit to the extracted reflectivity using above equation for reflectivity at first harmonic operation. The solid line shows the fit using the modified model proposed in this paper.

4.3 Modified Transmission Line Model

4.3.1 First Harmonic Operation

To improve the correlation to the data, modifications to the model are proposed. The data is asymmetric about $a/p = 0.5$, with the peak occurring at $a/p \approx 0.25$ for short circuit gratings and a peak at $a/p \approx 0.75$ for open circuit gratings. The theoretical prediction of the electrical loading contribution to reflectivity given by Datta [1] predicts a similar trend and the electrical loading term should be modified to predict this behavior. The data indicates that the sinusoidal term in the electrical loading contribution must include a higher order dependence on the metallization ratio than that assumed by Wright, so as to produce a peak that correlates with the skew in the data. The change in peak from $a/p \approx 0.25$ for short circuit gratings to $a/p \approx 0.75$ for open circuit gratings is due to a 180 degree phase change in the electrical loading term. To account for this change in phase, the a/p term in the electrical loading for open circuit grating is replaced with $\frac{a}{p} - 1$ in the short circuit grating equation. The new proposed equation form for electrode reflectivity is:

$$r^{o.c.} = \frac{\Delta Z_1}{Z_o} sin\left(\pi \left(\frac{a}{p}\right)^2\right) + \frac{\Delta Z_2}{Z_o} sin\left(\pi \left(\frac{a}{p}\right)^{10}\right) + \frac{\Delta Z_o}{Z_o} sin\left(\pi \frac{a}{p}\right) \frac{h}{\lambda} + \frac{B_o}{Y_o} sin\left(\pi \frac{a}{p}\right) cos\left(\pi \frac{a}{p}\right) \left(\frac{h}{\lambda}\right)^2 \tag{4.3}$$

$$r^{s.c.} = \frac{\Delta Z_1}{Z_o} sin\left(\pi\left(\frac{a}{p}-1\right)^2\right) + \frac{\Delta Z_2}{Z_o} sin\left(\pi\left(\frac{a}{p}-1\right)^{10}\right) + \frac{\Delta Z_o}{Z_o} sin\left(\pi\frac{a}{p}\right)\frac{h}{\lambda} + \frac{B_o}{Y_o} sin\left(\pi\frac{a}{p}\right) cos\left(\pi\frac{a}{p}\right)\left(\frac{h}{\lambda}\right)^2 \tag{4.4}$$

where, $r^{o.c.}$ and $r^{s.c.}$ are the open circuit grating and short circuit grating reflectivities. The terms $\Delta Z_1/Z_o$ and $\Delta Z_2/Z_o$ are the coefficients for the piezoelectric shorting terms, $\Delta Z_o/Z_o$ is the coefficient for the mechanical loading term and B_o/Y_o is the stored energy term. The signs of the coefficients were obtained from a least squares fit to the data and indicate whether the terms are adding in or out of phase with each other. The coefficients obtained from the least squares fit are given in the results section and can be used to predict reflectivity and velocity for any combination of metallization ratio and normalized metal thickness. Wright's form of the equation is based on the physical model of Fig. 4.5 and satisfies the cases for $a/p = 0$ and $a/p = 1$. The new reflectivity also satisfies the physical model of Fig. 4.5, but is modified to more accurately fit measured data. The mechanical loading, h/λ is included in equations (4.3) and (4.4) and is absent in equation (4.1). It is determined that the argument of the sine term for the electrical loading is of higher order power in equations (4.3) and (4.4) compared to equation (4.1).

As the wave propagates through a grating the perturbation caused by the presence of the electrodes results in an effective slowing down of the wave. There are three terms contributing to velocity, namely the piezoelectric shorting or electrical loading, the mechanical loading and the stored energy effect. The electrical loading is expected to be the dominant term due to the high

coupling coefficient of YZ $LiNbO_3$, therefore the linear trend in the velocity data implies that this term must have a linear dependence on the metallization ratio. Equation (4.2) lumps the mechanical loading term and electrical loading term into one term, however it has been shown [44] that the mechanical loading term has sinusoidal dependence on metallization ratio. It is also known that the mechanical loading term has a linear dependence on normalized metal thickness and the stored energy term has a quadratic dependence on the normalized metal thickness. The new grating velocity equation is:

$$v = v_o \left\{ 1 - \frac{\Delta v_1}{v_o} \left(\frac{a}{p} \right) - \frac{\Delta v_o}{v_o} sin \left(\pi \frac{a}{p} \right) \frac{h}{\lambda} - \frac{B_o}{Y_o} sin \left(\pi \frac{a}{p} \right) \left(\frac{h}{\lambda} \right)^2 \right\} \tag{4.5}$$

where, $\Delta v_1/v_o$ is the electrical loading coefficient, $\Delta v_o/v_o$ is the mechanical loading coefficient, and B_o/Y_o is normalized susceptance term representing the stored energy coefficient. All the terms are assumed to contribute to the slowing of the wave, however, the signs of the coefficients obtained from the least squares fit indicate how the terms interact with each other.

4.3.2 Second Harmonic Operation

The perturbation theory representation for the electrical loading term for second harmonic reflectivity derived by Datta [1] has a sin^2 dependence on a/p. The data for the second harmonic

reflectivity is nearly symmetric around a peak reflectivity occurring at a metallization ratio of 0.5, therefore the electrical loading term for fundamental and second harmonic reflectivity must be different. The new proposed second harmonic grating reflectivity equation for both open circuit and short circuit gratings is given as:

$$r = \frac{\Delta Z_1}{Z_o} sin\left(\pi \frac{a}{p}\right)^2 + \frac{\Delta Z_o}{Z_o} sin\left(2\pi \frac{a}{p}\right) \frac{h}{\lambda} + \frac{B_o}{Y_o} sin\left(\pi \frac{a}{p}\right) cos\left(2\pi \frac{a}{p}\right) \left(\frac{h}{\lambda}\right)^2 \tag{4.6}$$

where, $\Delta Z_1/Z_o$ is the piezoelectric shorting coefficient, $\Delta Z_o/Z_o$ is the mass loading coefficient and B_o/Y_o is the normalized susceptance term which represents the stored energy coefficient. Similarly for the velocity at second harmonic the linear dependence on a/p is replaced with a quadratic dependence on a/p for the electrical loading term. The velocity equation is then written as:

$$v = v_o \left\{ 1 - \frac{\Delta v_1}{v_o} \left(\frac{a}{p}\right)^2 - \frac{\Delta v_o}{v_o} sin\left(\frac{\pi a}{p}\right) \frac{h}{\lambda} - \frac{B_o}{Y_o} sin\left(\frac{\pi a}{p}\right) \left(\frac{h}{\lambda}\right)^2 \right\} \tag{4.7}$$

where, $\Delta v_1/v_o$ is the electrical loading coefficient, $\Delta v_o/v_o$ is the mechanical loading coefficient, and B_o/Y_o is normalized susceptance term representing the stored energy coefficient.

4.4 Experimental Results

The coefficients for the modified transmission line model discussed above were obtained by performing a least squares fit to experimentally extracted reflectivity and velocity data. Data was extracted for both open and short circuit gratings, at both fundamental and second harmonic operation, over a wide range of metallization ratios and normalized metal thickness in order to fully characterize the behavior. The results are shown and the coefficients obtained for each case are given. These coefficients were then used to model grating reflectivity and velocity in the coupling of modes (COM) model for orthogonal frequency coded (OFC) gratings and the experimental and COM results are shown and discussed.

4.4.1 Results for First Harmonic Operation

Fig. 4.7 and Fig. 4.8 show the reflectivity per strip at fundamental operation for shorted and open circuit aluminum gratings on YZ $LiNbO_3$. The reflectivity is extracted versus metallization ratio ranging from 0.2 to 0.9 and normalized metal thickness ranging from 0.4% to 2%. The markers represent the extracted data and the lines are the curve fits to the data using a least squares fit to the transmission line model discussed.

The shorted grating has a maximum reflectivity value of approximately 2% which is slightly higher than the maximum reflectivity of 1.8% for an open grating. The maximum reflectivity for a shorted grating occurs at a metallization ratio of 0.2, while the open grating has an opposing

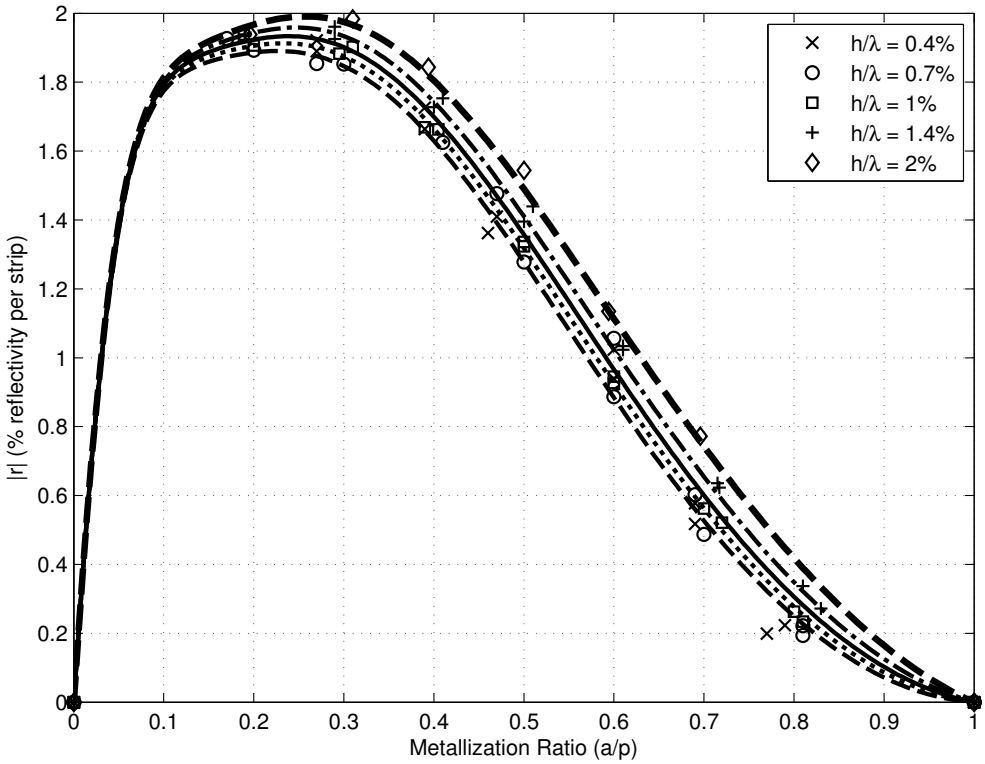

Figure 4.7: Reflectivity per strip versus metallization ratio and normalized metal thickness for shorted aluminum gratings at fundamental operation. The metallization ratio varies from 0.2 to 0.8 and the normalized metal thickness ranges from 0.4% to 2%.

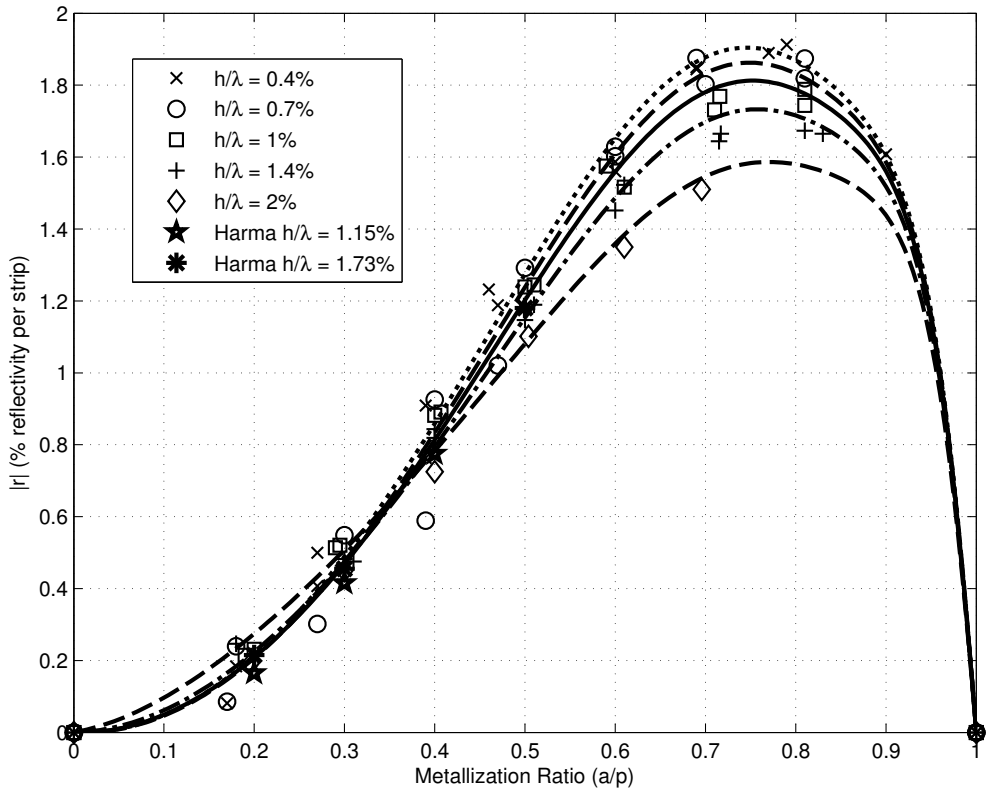

Figure 4.8: Reflectivity per strip versus metallization ratio and normalized metal thickness for open circuit aluminum gratings at fundamental operation. The metallization ratio varies from 0.2 to 0.9 and the normalized metal thickness ranges from 0.4% to 2%. Reflectivity per strip extracted by Härmä [2] is also plotted.

trend in the reflectivity with a maximum value occurring at a metallization ratio of approximately 0.8. This makes physical sense since the electrical regeneration effect in the open grating adds out of phase with the net reflectivity and since the regeneration effect grows weaker with increasing metallization ratio, the open grating reflectivity reaches a maximum value at a metallization ratio of 0.8. As shown in Fig. 4.7 and Fig. 4.8, the reflectivity increases with increasing normalized metal thickness, but the change is not significant with the maximum difference in reflectivity of approximately 0.5%. This is expected since lithium niobate is a high coupling material and the piezoelectric shorting is the dominant effect. The shorted grating reflectivity for a normalized metal thickness of 0.3% has been previously presented by Wright [42] and showed a maximum reflectivity of approximately 2.5%, which is slightly higher that the value extracted in this work. Perturbation theory predicts a reflectivity of 1.7% at a metallization ratio of 0.5 for near zero metal thickness, however, the experimentally extracted reflectivity had a value of aproximately 1.4% which correlates with the value extracted by Peter Cross [45]. Open circuit reflectivity data by Härmä et al [2] are shown in Fig. 4.8, and correlate with the extracted data in this dissertation. The reason for the measurement discrepancy with perturbation theory is not clear. The grating in this work used a lift-off process and a SEM micrography is shown in Fig. 4.9 for $a/p = 0.5$ and shows no obvious abnormalities due to fabrication.

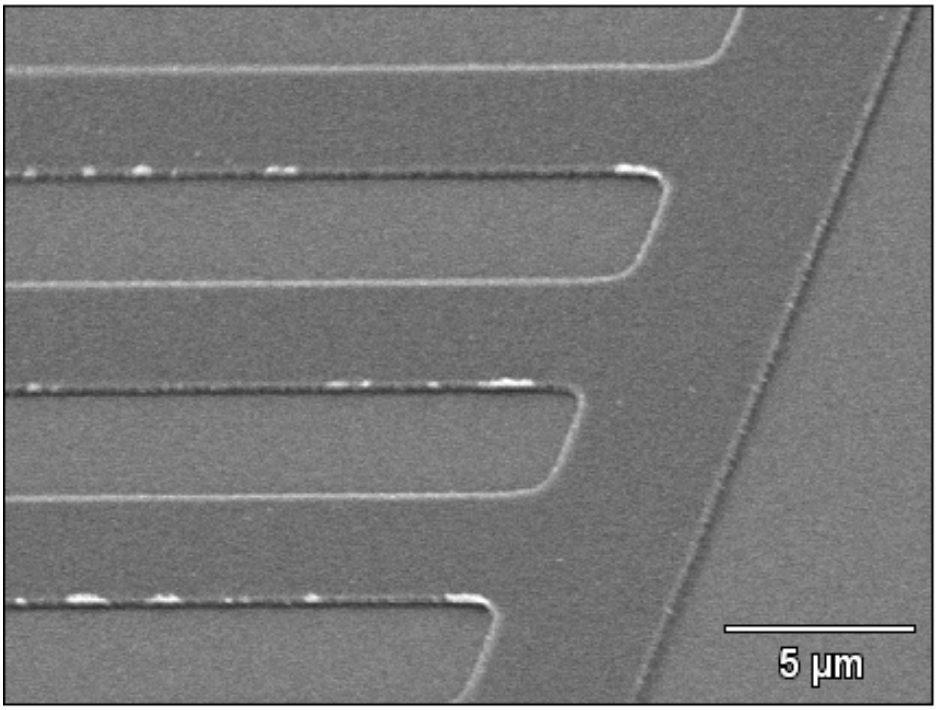

Figure 4.9: SEM image of a typical aluminum grating on YZ $LiNbO_3$. The grating has a metallization ratio of 0.5 as verified in the image and the metal thickness was 1200 Angstroms.

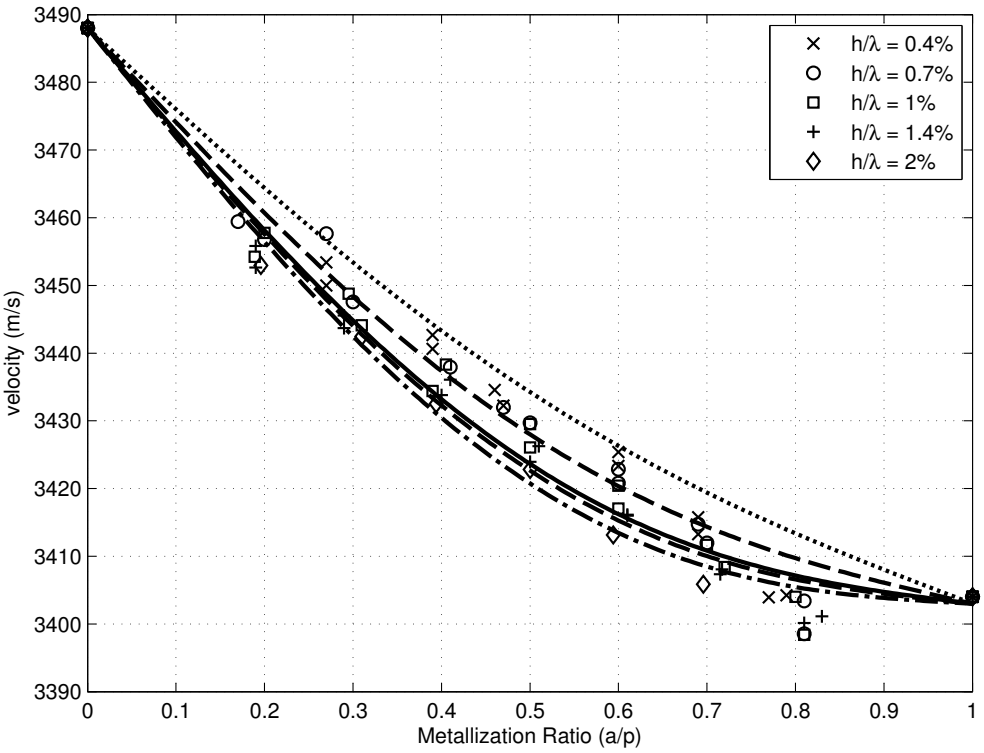

Figure 4.10: Grating velocity versus metallization ratio and normalized metal thickness for shorted aluminum gratings at fundamental operation. The metallization ratio varies from 0.2 to 0.8 and the normalized metal thickness ranges from 0.4% to 2%.

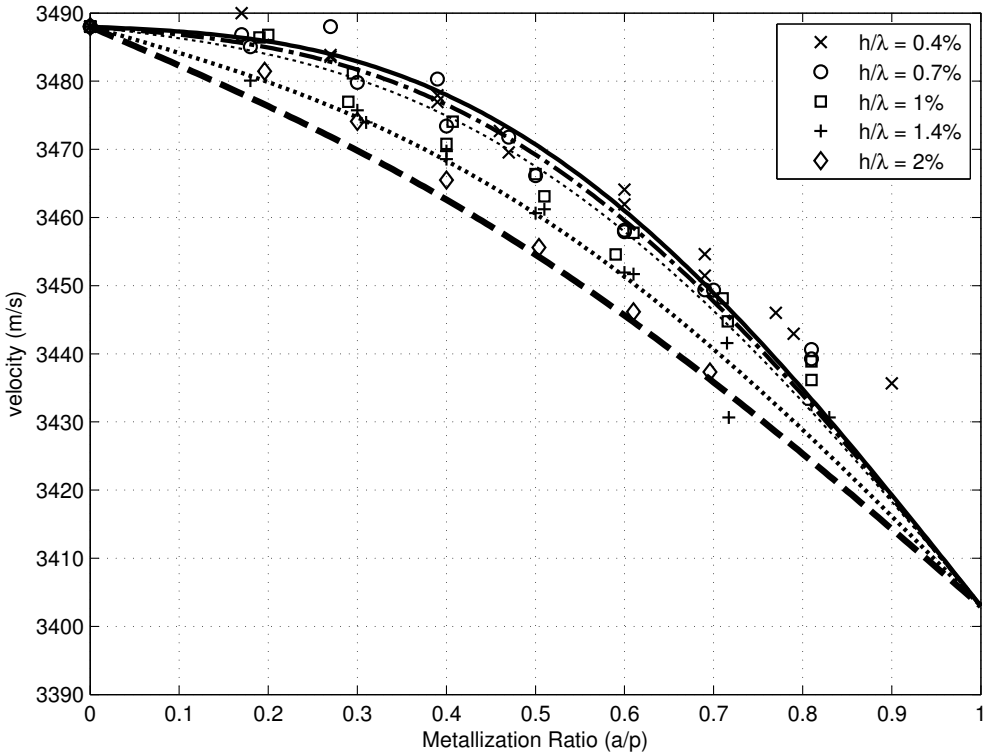

Figure 4.11: Grating velocity versus metallization ratio and normalized metal thickness for open aluminum gratings at fundamental operation. The metallization ratio varies from 0.2 to 0.9 and the normalized metal thickness ranges from 0.4% to 2%.

Fig. 4.10 and Fig. 4.11 show the shorted and open grating velocity, respectively, versus varying metallization ratio and normalized metal thickness at fundamental operation. The free surface velocity occurs at a metallization ratio of zero and slows to the metallized velocity at a metallization ratio of one. The convex and concave curvatures of the fitted curves are predicted by the Floquet analysis for open and short circuit gratings given by Morgan [20]. The coefficients extracted from least squares fit to the data are given in Table 4.3. Note that the signs of the mechanical loading term and the stored energy term are different for the short circuit case and the open circuit case. In the short circuit case the mechanical loading term adds in phase with the electrical loading term and the stored energy term adds out of phase, while the opposite is true in the open circuit case.

Table 4.3: First Harmonic Coefficients for the Transmission Line Model Obtained from Least Squares Fit to the Data

	Reflectivity Coefficients				Velocity Coefficients		
Grating Type	$\frac{\Delta Z_1}{Z_o}$	$\frac{\Delta Z_2}{Z_o}$	$\frac{\Delta Z_o}{Z_o}$	$\frac{B_o}{Y_o}$	$\frac{\Delta v_1}{v_o}$	$\frac{\Delta v_o}{v_o}$	$\frac{B_o}{Y_o}$
Shorted Grating	0.0173	0.0089	0.01327	-2.403	.024	.926	-29.934
Open Grating	0.0187	0.0065	-0.0121	9.5896	.024	1.3159	59.323

4.4.2 Results for Second Harmonic Operation

Fig. 4.12 and Fig. 4.13 are the shorted and open reflectivity per strip versus metallization ratio and normalized metal thickness for second harmonic operation on YZ $LiNbO_3$. The shorted and open

grating reflectivities for second harmonic operation look very similar, as predicted by perturbation theory. The open-circuit reflectivity at second harmonic has a slightly lower value than the short-circuit reflectivity. This may be due to the resistive losses introduced by the regenerative effect of open-circuit gratings, but is unclear at this time. The reflectivity peaks at a metallization ratio of 0.5 for low normalized metal thicknesses and becomes asymmetric for higher normalized metal thickness of 3% and 4%.

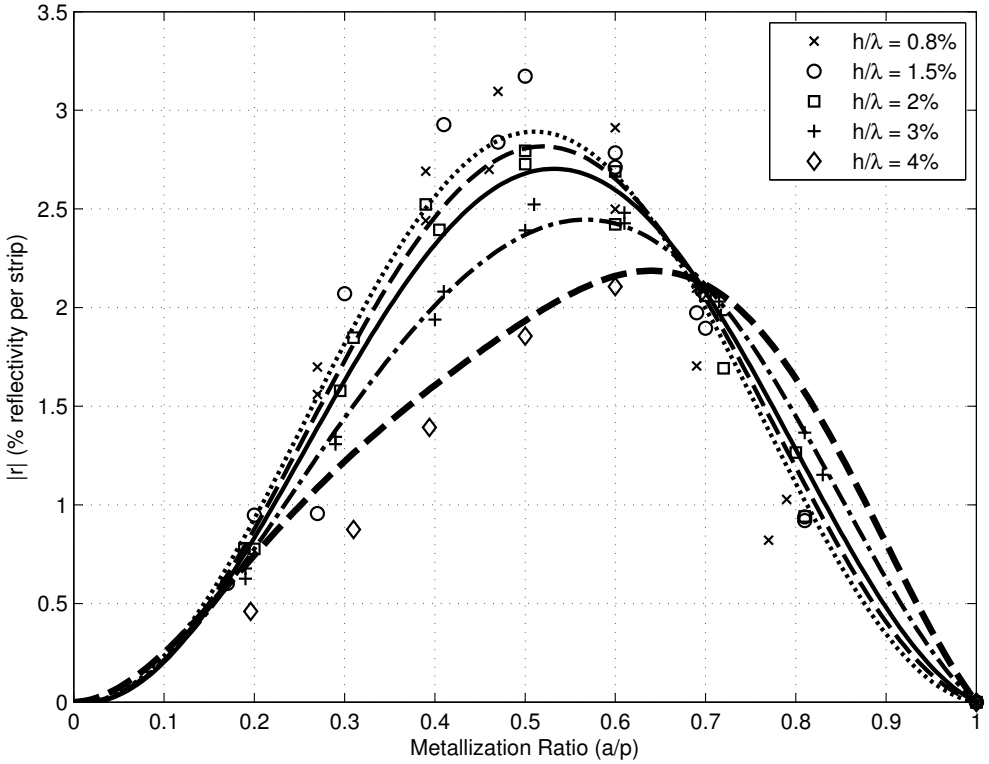

Figure 4.12: Grating reflectivity versus metallization ratio and normalized metal thickness for shorted aluminum gratings at second harmonic operation. The metallization ratio varies from 0.2 to 0.8 and the normalized metal thickness ranges from 0.8% to 4%.

At second harmonic the grating has only one period per wavelength as compared to two periods for fundamental operation; at a metallization ratio of 0.5, the electrical loading and mechanical

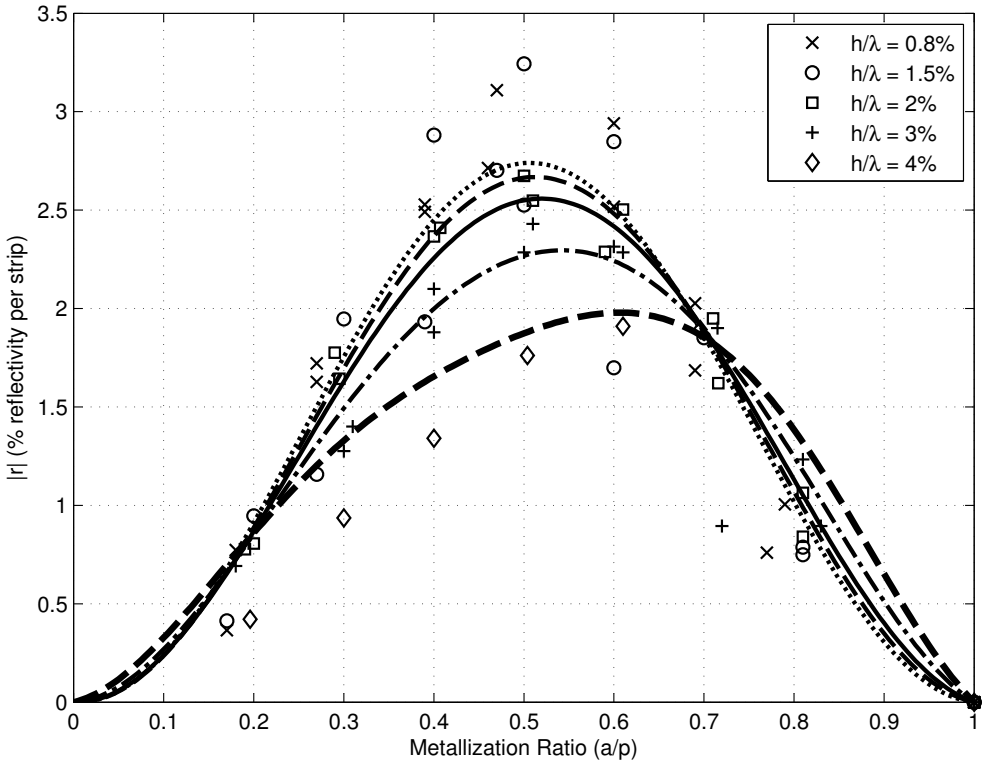

Figure 4.13: Grating reflectivity versus metallization ratio and normalized metal thickness for open aluminum gratings at second harmonic operation. The metallization ratio varies from 0.2 to 0.8 and the normalized metal thickness ranges from 0.8% to 4%.

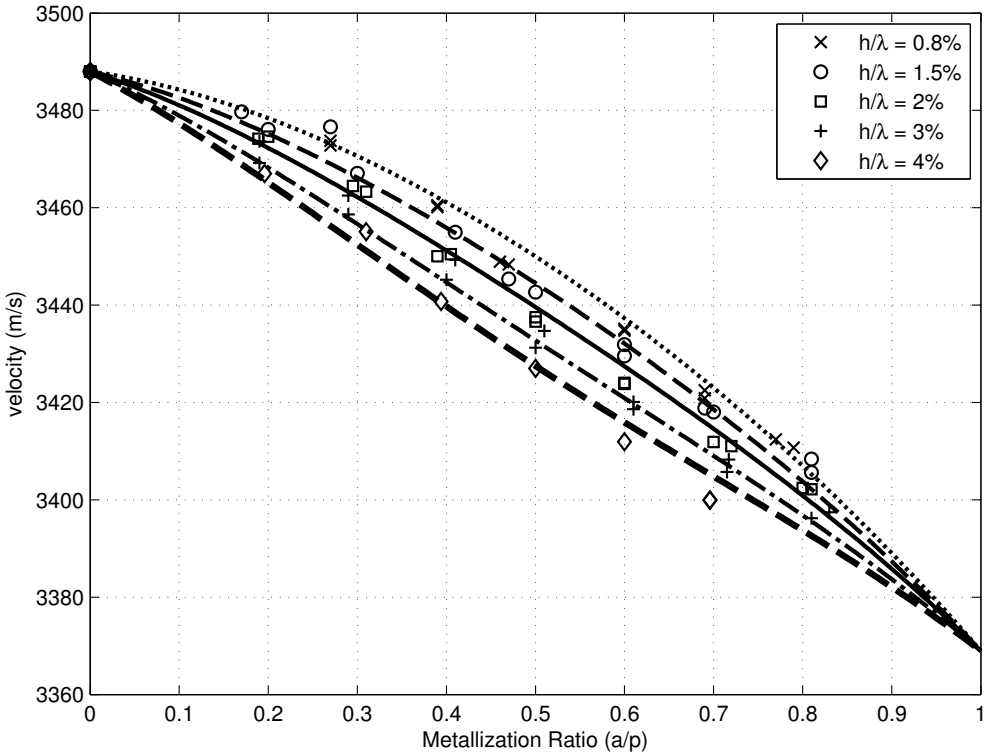

Figure 4.14: Grating velocity versus metallization ratio and normalized metal thickness for shorted aluminum gratings at second harmonic operation. The metallization ratio varies from 0.2 to 0.8 and the normalized metal thickness ranges from 0.8% to 4%.

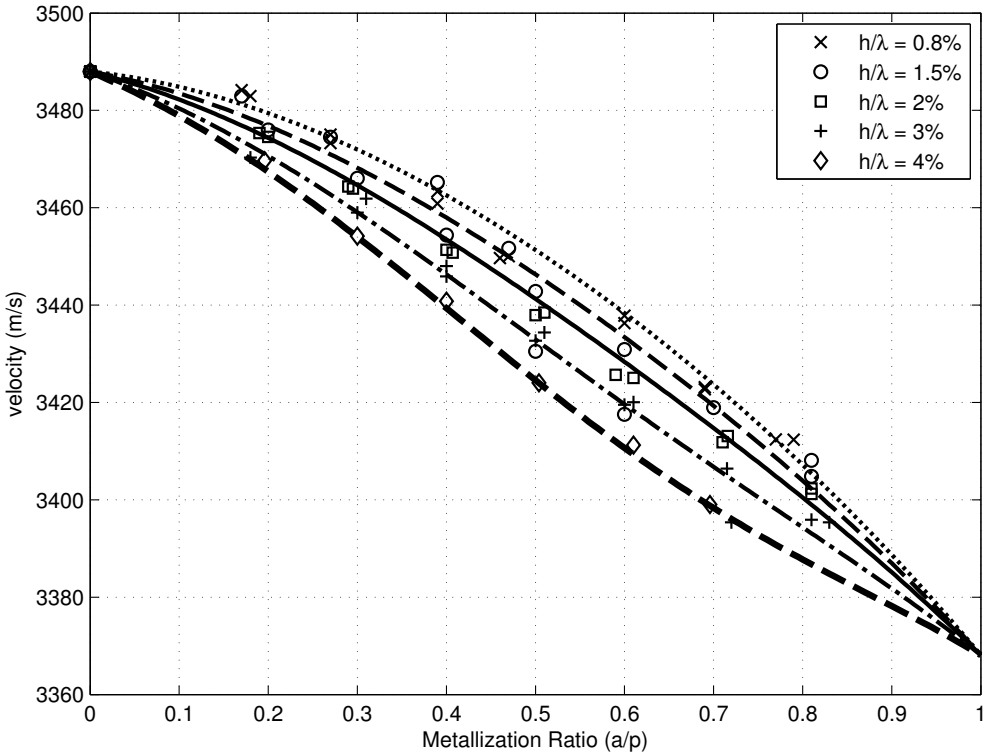

Figure 4.15: Grating velocity versus metallization ratio and normalized metal thickness for open aluminum gratings at second harmonic operation. The metallization ratio varies from 0.2 to 0.8 and the normalized metal thickness ranges from 0.8% to 4%.

loading term add out of phase canceling each other but the reflections from the stored energy term add in phase contributing to a net reflection. For metallization ratios below 0.5 the second harmonic reflectors mimic open grating behavior at fundamental operation, while for metallization ratios above 0.5, the reflectors behave like shorted gratings at fundamental operation. Fig. 4.14 and Fig. 4.15 show the shorted and open grating velocity results, respectively, versus varying metallization ratio and normalized metal thickness at second harmonic operation. There is more scatter in the extracted second harmonic data as compared to the fundamental data. The second harmonic measurements and parameter extraction were found to be more sensitive to many variables, which include measurement accuracy, *a/p* measurements, electrode fabrication, material losses and probably more. The model predicts similar behavior for both open and shorted grating velocities at second harmonic operation as predicted from perturbation theory; the coefficients are given in Table 4.4.

Table 4.4: Second Harmonic Coefficients for the Transmission Line Model Obtained from Least Squares Fit to the Data

	Reflectivity Coefficients			Velocity Coefficients		
Grating Type	$\frac{\Delta Z_1}{Z_o}$	$\frac{\Delta Z_o}{Z_o}$	$\frac{B_o}{Y_o}$	$\frac{\Delta v_1}{v_o}$	$\frac{\Delta v_o}{v_o}$	$\frac{B_o}{Y_o}$
Shorted Grating	0.0293	-0.1178	6.2235	.03412	0.3141	-2.3436
Open Grating	0.0277	-0.0689	5.6292	.03458	0.2903	-1.7789

4.4.3 Reflector Loss Discussion

The focus of this work was to provide a large data base of reflectivity at fundamental and harmonic operation on YZ $LiNbO_3$, to develop grating models useful in COM and other simulation tools. The device wavelengths were chosen to allow for a range of normalized aluminum metal thicknesses. The wavelengths were chosen such that all devices had an operational center frequency of less than 250 MHz. This provides very low free-surface propagation loss and assumes a low metalized film propagation loss. The grating lengths were chosen to provide good reflectivity, but short enough so that there was little stored energy due to multi-reflections within the grating. This provided nearly ideal sinc frequency responses for the gratings and enhanced the accuracy of parameter extraction. The extracted data assumed zero losses in the grating, i.e., ideal reflectivity. This is, of course, inaccurate and any losses will result in a reduced extracted reflectivity from the data. However, test data points were obtained on selected devices to attempt to bound the losses and determine the possible extent of loss on extracted reflectivity. A three transducer test structure, similar to Wright's [42], was fabricated, where a third transducer is placed on the opposite side of the grating (refer to Fig. 4.1). As Wright points out, in general, reflection measurements are more accurate than transmission measurements in reflectivity data extraction, but are very useful tool for diagnostic purposes. With these 3 transducers, various combinations of transmission and reflectivity data combinations can be obtained and used to estimate losses. The test structure for loss extraction and the different measurements used to extract losses are shown in Fig. 4.16.

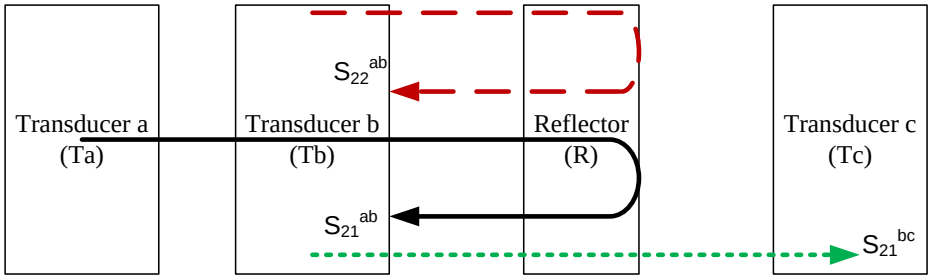

Figure 4.16: The test structure for loss extraction and the different measurements used to extract losses. A combination of reflection and transmission measurements are used to isolate losses under the grating electrodes.

First the reflector responses from the two-port measurements between transducer a and b are compared to isolate any losses from propagation under transducer b. This is done by comparing the gated reflector response from S_{21}^{ab} and S_{22}^{ab}. The loss under transducer b was found to be negligible because it was a wide-band transducer and had only five electrode pairs. From energy arguments, the reflected energy from S_{21}^{ab} , from the isolated reflector and transmitted energy from the S_{21}^{bc} from transducer b to c in the reflector passband should equal one if there are no losses, i.e. $R^2 + T^2 = 1$. Using these energy arguments the loss under the reflector grating can be isolated. Lehtonen, et.al., [46] developed reflectivity and transmission equations, with and without attenuation in the grating. This approach was used by Härmä, et.al. [2], in her data extraction analysis on fundamental YZ $LiNbO_3$ gratings. Following the approach by Lehtonen [46], the COM attenuation parameter, $\gamma(f_c)$ at center frequency is given as:

$$\gamma\left(f_c\right) = -log_e \frac{\left(\left|R\left(f_c\right)\right|^2 + \left|T\left(f_c\right)\right|^2\right)}{2L} \tag{4.8}$$

where $|R(f_c|$ and $|T(f_c)|$ are the reflection and transmission coefficients of the grating at center frequency obtained by normalizing the time-gated reflected and transmitted responses of the reflector to a reference S_{21} delay line response and *L* is the length of the reflector and $L = N_g p$, where N_g is the number of electrodes in the grating and *p* is the period of the grating. Using equation (4.8) and the S-paramater data sets from combinations of the three transducer experimental data, grating losses could be estimated and the loss per electrode extracted. For devices with $h/\lambda = 0.4\%$ at fundamental operation, the attenuation parameter, $\gamma(f_c)$, per wavelength for several a/p values were in the range of 6×10^{-3} to 8×10^{-3} Neper/wavelength; the attenuation per Härmä [2] was in the range of 1.49×10^{-3} to 4.6×10^{-3} Neper/wavelength. Considering this loss parameter in our lossless extraction method, an error of 7% to 9% in the extracted reflectivity values is obtained. At second harmonic for the same devices, there is only one electrode per wavelength and the center frequency of operation is doubled. The attenuation parameter $\gamma(f_c)$ at second harmonic, for devices with $h/\lambda = 0.8\%$ was found to be in the range of 9.4×10^{-3} to 1.4×10^{-2} Neper/wavelength. Considering this loss parameter in the extraction technique yields an error of 13% to 17% in the extracted reflectivity values, which is twice that at fundamental operation.

These attenuation coefficients extracted for fundamental operation of the gratings are consistent with previously published results. The data and analysis appear to confirm that the choice of grating experimental parameters used in the extraction yield reasonably good reflectivity data, even ignoring losses, but are probably low and may be increased by as much as 5-10%. Second harmonic grating operation appears to have greater error in extracted reflectivity, possible 10-20%, based on the loss analysis. There is no other published second harmonic experimental data on YZ

$LiNbO_3$ for comparison at the present time. Since the purpose of this paper is not to provide a detailed grating loss analysis, the model developed and the coefficients provided should provide reasonably good model parameters. The attenuation coefficients provided may also be used to further enhance models, but caution should be exercised. The losses extracted here and in the literature are for limited data sets and at relatively low frequency. Interpolating to higher frequencies and/or attributing losses to any particular effect may lead to false predictions. Further work to determine loss mechanisms and their frequency dependence is warranted, and will be the subject of future efforts. Using the coefficients in tables 4.3 and 4.4 in the equations for fundamental and second harmonic reflectivity and velocity, the reflectivity and velocity for any combination of metallization ratio and normalized metal thickness can be predicted. The equations were programed into the COM model in MATLAB®and used to design and model the coded OFC and P-OFC SAW tags presented in this dissertation.

CHAPTER 5
SPREAD SPECTRUM IMPLEMENTATION OF SAW RFID TAGS AND SENSORS

In recent years there has been an increasing interest in SAW sensor technology for use in many applications such as sensing measureands off of moving machine parts such as turbine blades, gears etc. and moving vehicles, or in hazardous environments where the use of a wired sensor is not possible. SAW devices offer an ideal solution in many of these applications, they are small, rugged, low-cost and can be operated passively, eliminating the need for a battery. SAW based sensors have been previously used to measure temperature, pressure, force, torque, strain, and mass-loading [47, 48]. Delay-line and resonator type SAW sensors have been used previously, but these topologies do not enable coding of the sensor and are ideal for a single sensor environment. In a multi-sensor environment, it is necessary to identify each sensor while simultaneously measuring the external stimuli and this requires coding of the sensor for identification. In this chapter a background on spread spectrum communications and spread spectrum SAW sensor techniques will be provided followed by an introduction to previous work done on orthogonal frequency coded SAW sensor tags.

In a SAW sensor, the physical quantity to be measured produces a physical change in the path of the acoustic wave propagating on the surface of the piezoelectric material. External stimuli

such as temperature, pressure, mechanical stress, etc. change the length of the acoustic path of the piezoelectric material, thus making it possible to sense these measureands remotely. Wireless SAW sensors have been used as temperature sensors, torque sensors on rotating shafts of gears, tire pressure sensors in a moving car etc [49, 50, 51]. Some of these sensors use resonator devices or delay-line devices which cannot be encoded for tag identification. Coding approaches such as chirp impulse compression and single frequency CDMA tags have been used in the past. These techniques allow for an increase of sensitivity and accuracy of measurement, and an increase in range due to the processing gain as a result of spreading the bit information. Some spread spectrum concepts and approaches to communications systems will be discussed in the next section in order to aide in the understanding of these techniques applied to SAW multiple access sensor tags.

5.1 Spread Spectrum Concepts

Spread-spectrum communication systems offer several advantages such as, multiple access, resistance to jamming, inherent security, reduced effects of multipath fading and noise, and longer range. In spread spectrum systems the frequency spectrum of the information signal is spread over a much larger frequency bandwidth than what is necessary for transmitting the information. There are several methods of accomplishing this such as direct sequence modulation, frequency hopping, and orthogonal frequency division multiplexing. The concepts and advantages of some of these techniques will be explained as they apply to a communications system. The background and implementation of spread spectrum SAW sensors for multiple access will then be discussed.

5.1.1 Direct Sequence Spread Spectrum (DSSS)

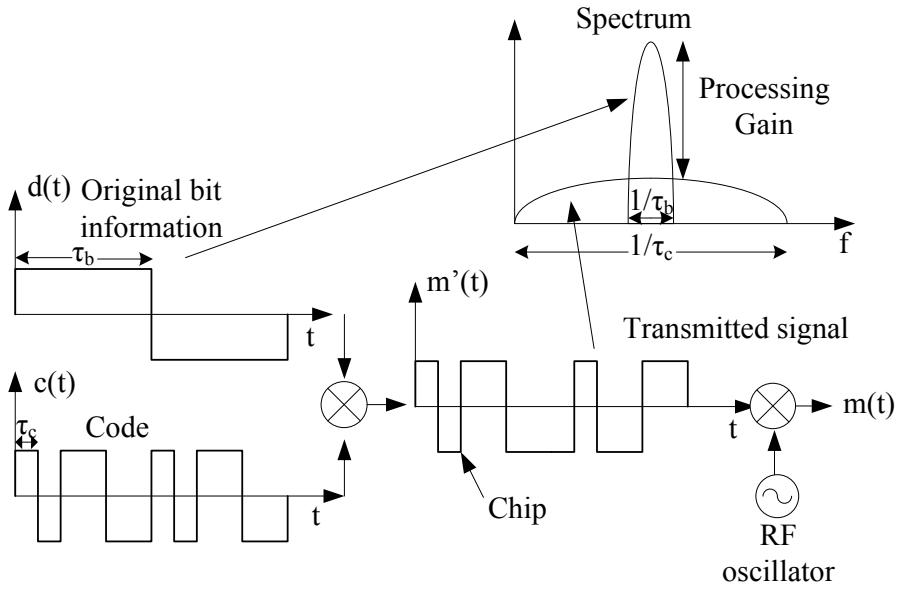

Figure 5.1: Transmitter for a DS/SS system. The bit information and coding signal are mixed together and then translated to carrier frequency. The frequency spectrum shows the bandwidth spreading in the transmitted signal due to the coding.

In direct sequence spread spectrum each pulse of the information signal is mixed with a coding signal and the resulting signal is then translated to the system carrier frequency as shown in Fig. 5.1. Each pulse of the information signal, d(t), is called a bit and has a width τ_b and each pulse of the coding signal, c(t), is called a chip and has a width τ_c.

The most commonly used coding technique is binary phase shift keying (BPSK), where the coding signal is a psuedo-noise (PN) sequence of ± 1 with an integer number of chips corresponding to each bit length such that

$$\tau_b = N \cdot \tau_c \tag{5.1}$$

The PN sequence is a deterministic, psuedo-random sequence of positive and negative chips that are chosen to approximate the statistical properties of white noise [52]. The cross-correlation between PN-codes determines the interference between multiple codes in a multiple access system. If the cross-correlation is zero then the codes are considered to be orthogonal with minimal interference between multiple users. In the DS/SS system the frequency null bandwidth of the transmitted signal, *m(t)*, is *N* times wider than the bandwidth of the original information bit. This spreading of bandwidth reduces the peak power spectral density of the signal and leads to processing gain in the system which is given as:

$$PG = 10 \cdot log \frac{Bandwidth_{bit}}{Bandwidth_{chip}} = 10 \cdot logN \tag{5.2}$$

At the receiver a correlation with a replica of the coding signal is used to demodulate the received signal and recover the original information. The correlation can be done using either a passive correlator (matched filter) or an active correlator if the receiver can be synchronized [53, 54]. Shown in Fig. 5.2 is the receiver block diagram for the DS/SS system. When the receiver is not synchronized the matched filter technique is used for demodulation. The impulse response of the matched filter, h(t) is given as the time reversal of the coding signal c(t):

$$h(t) = c\left(\tau_b - t\right)) \tag{5.3}$$

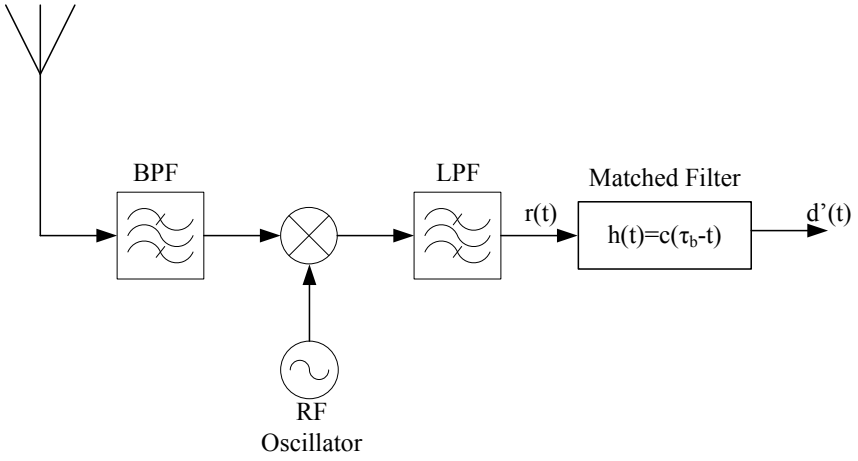

Figure 5.2: Block diagram for a DS/SS fixed correlator receiver. The received signal r(t) is matched filtered to demodulate it and recover the original information signal.

The output of the matched filter, d'(t) is the convolution of the received signal with h(t). In the frequency domain, using fourier transforms the output can be written as:

$$D'(f) = R(f) \cdot C^*(f) \tag{5.4}$$

where $C^*(f)$ is the fourier transform of the complex conjugate of the coding signal and $R(f)$ is the received signal modulated to baseband. The output of the matched filter correlation is a series positive and negative pulses corresponding to the original bit information. The matched filter correlation process is effective in eliminating interference from multipath fading, signal jamming or interference from other PN codes used in a multiple access system. In case of multipath fading, the multipath signals have a larger time delay than the direct path signal. The pulse compression achieved using the matched filter can be used to separate the direct path signal from other multipath

signals that are spaced at least one chip length away from the direct path signal. If the time delay of the multipath is less than one chip width it will interfere with the direct path signal. The pulse compression is a function of the time-bandwidth product of the spread spectrum signal [53]. Thus, if the transmitted signal is jammed, the matched filter spreads the jamming signal during convolution while the desired signal bandwidth is compressed to obtain the original information. As a result of the spreading, the peak power spectral density of the jamming signal within the bandwidth of interest is reduced proportional to the processing gain.

The DS/SS system also allows multiple users to share the same bandwidth simultaneously in a multiple access communications system where each user is assigned a unique psuedo-noise code (PN code). This is called code division multiple access (CDMA); the PN codes of the users in the system are chosen to be orthogonal to each other. The correlation process allows the transmission from a desired user to rise out of the noise while the other codes remain uncorrelated due to code orthogonality.

5.1.2 Frequency Hopped Spread Spectrum (FHSS)

Frequency hopped spread spectrum is an alternate method to spread the spectrum of the original information by modifying the carrier frequency periodically. The spreading code in the FHSS case is the frequency hopping pattern or list of frequencies used for the carrier signal. The frequency hopping occurs over a frequency band called the hopping band and includes M possible frequency channels or carrier frequencies. Each frequency channel has a spectral bandwidth, B, which is

large enough to include most of the power in a signal pulse with a specific carrier frequency [55]. The hopping bandwidth BW_{ss} is defined as:

$$BW_{ss} = M \cdot B \tag{5.5}$$

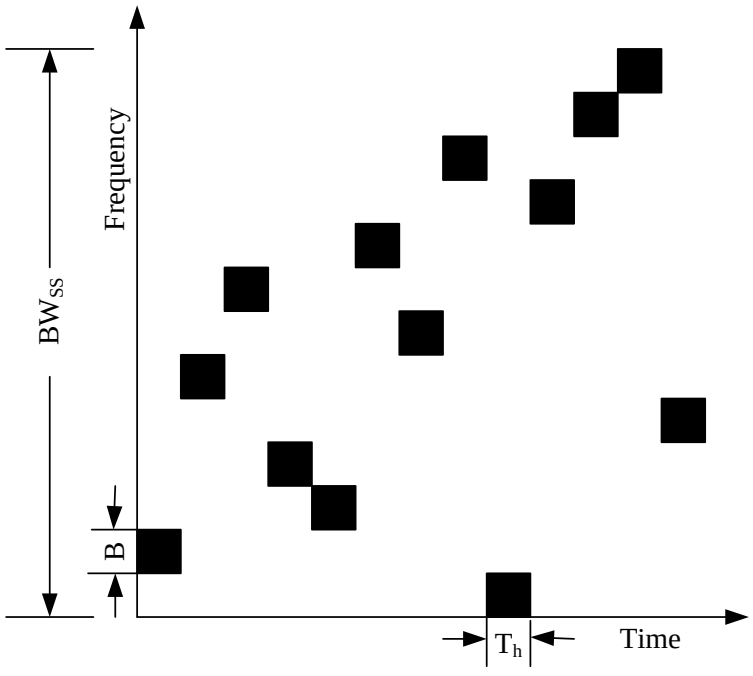

Figure 5.3: Frequency hopped signal pattern. The vertical axis is a map of frequency channels and the horizontal axis indicates the dwell time in each frequency channel.

The time between hops is called the hop interval and the time spent in each frequency channel is called the dwell time, T_h. Fig. 5.3 is an example of a frequency hopped signal pattern. The vertical axis is a map of frequency channels and the horizontal axis indicates the dwell time in each frequency channel. Over the time period T_h, the frequency bandwidth is a narrow slot B, but

over several hops the bandwidth is spread to occupy a much wider spectrum BW_{ss}. This spreading of bandwidth yields a system processing gain which is given by:

$$PG_{FHSS} = 10 \cdot log\frac{BW_{ss}}{B} = 10 \cdot logM \tag{5.6}$$

Frequency hopping can be classified as either slow or fast hopping [53]. For slow hopping the dwell time is larger than the bit length and for fast hopping the dwell time is smaller than the bit length.

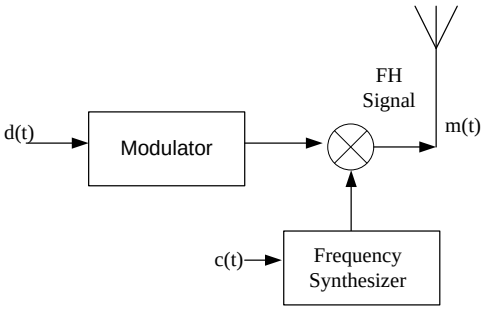

(a) FHSS transmitter block diagram

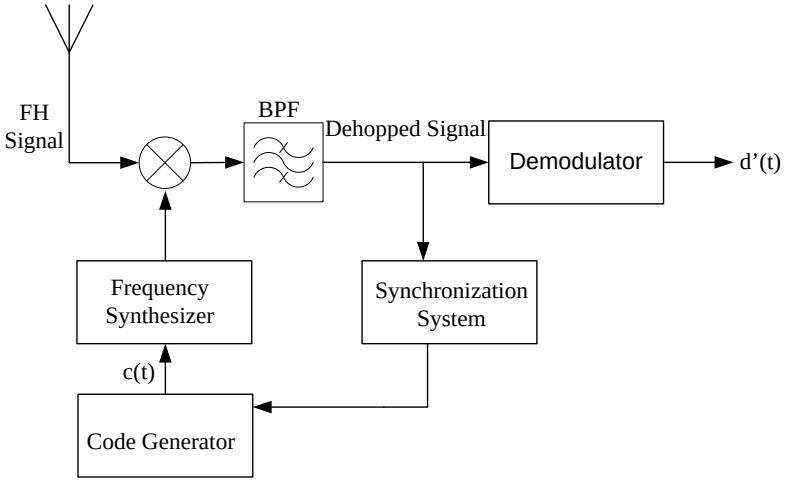

(b) FHSS synchronized receiver block diagram

Figure 5.4: Block diagram of a FHSS transmitter and receiver. (a) At the transmitter the modulated data is mixed with a frequency synthesizer output to produce the frequency hopped signal. (b) At the receiver the frequency hopped signal is decoded using a synchronized synthesizer. The dehopped signal is then demodulated to recover the original data.

Shown in Fig. 5.4 is the block diagram of a FHSS transmitter and receiver. A frequency synthesizer is used in the transmitter to produce frequency-hopping patterns determined by the time-varying multilevel sequence specified by the output bits of a code generator [55]. The data is first modulated using any suitable technique such as BPSK or DS/SS in a hybrid system [53]. The modulated signal is then mixed with the output from a frequency synthesizer to produce the frequency hopped signal. At the receiver the frequency hopped signal is decoded or dehopped using a synchronized synthesizer and demodulated to recover the original data.

5.1.3 Orthogonal Frequency Division Multiplexing (OFDM)

OFDM is a multi carrier communication system where the available spectral bandwidth is divided into many narrow band signals with different sub-carrier frequencies that are transmitted in parallel to minimize interference due to narrow-band interference and frequency-selective fading. The narrow-band signals are represented by pulses in the time-domain and are characterized by sin(x)/x frequency responses.

The individual sub-carrier frequencies are chosen such that an integral number of cycles are contained in a bit and the signals are mathematically orthogonal to each other. A more detailed mathematical description of orthogonality will be given later on in the chapter. The frequency responses of a set of OFDM signals is shown in Fig. 5.5. Although the sub-carrier spectra overlap, the orthogonality condition precludes interference between channels.

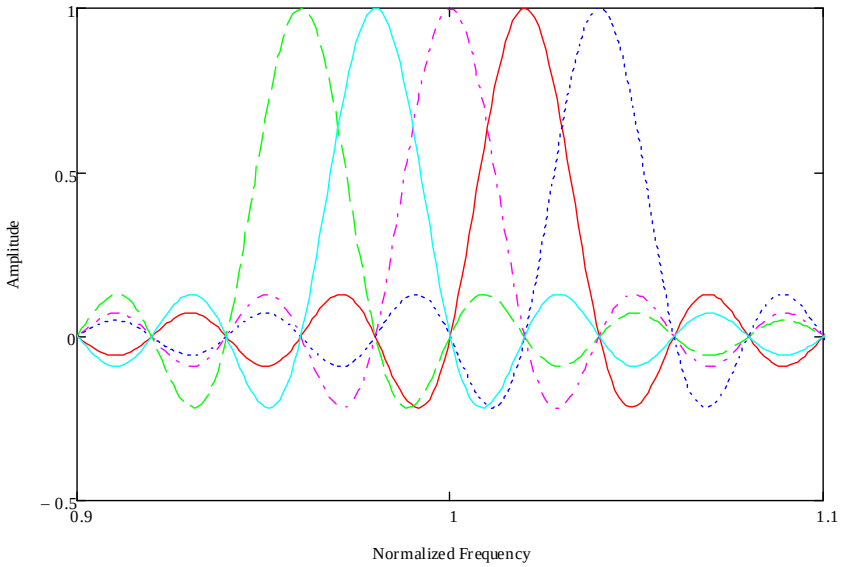

Figure 5.5: 5-Subchannel spectra of an OFDM signal; although the sub-carriers have some spectral overlap, interference between channels is minimal due to sub-carrier signal orthogonality. The frequency is normalized to center frequency.

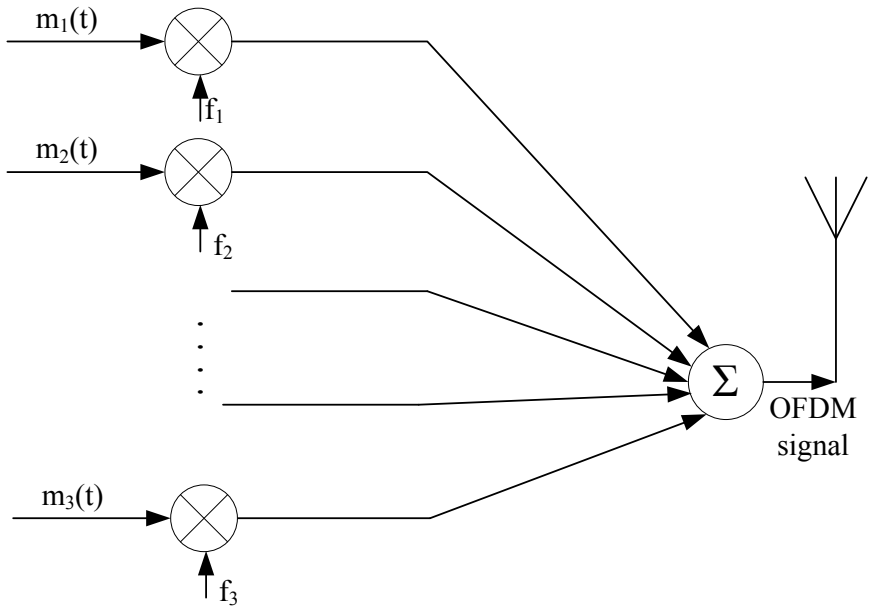

(a) OFDM transmitter block diagram

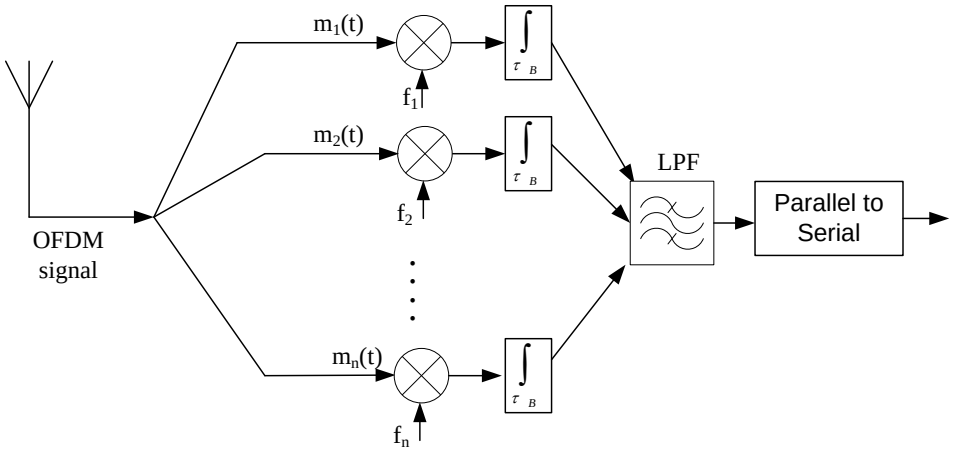

(b) OFDM receiver block diagram

Figure 5.6: Block diagram of an OFDM (a)transmitter and (b)receiver.

Fig. 5.6 is a block diagram for an OFDM transmitter and receiver. All the sub-carrier frequency channels are summed and transmitted simultaneously at the transmitter. At the receiver the received signal is demodulated by translating each carrier down to DC, where the resulting signal is integrated over a symbol period to determine the average amplitude in each bit and recover the original data [56, 3]. The spread spectrum concepts discussed are applied to the design and implementation of SAW sensor tags for multiple access and are discussed in the following sections.

5.2 Spread Spectrum Techniques For Sensors

Spread spectrum methods can be employed in SAW sensors to allow for use in a multiple access environment. SAW sensors are passive devices and are interrogated via an antenna connected to the electroacoustic transducer on the surface of a piezoelectric substrate. The acoustic signal or bit information is then transmitted through an array of passive reflectors or chips which can be designed to provide both time and frequency coding. The signal reflected by the coded reflectors is then retransmitted via the the transducer and antenna to the reciever. The overall insertion loss of the SAW sensor is the difference in the power received at the sensor and the signal retransmitted to the receiver. From the radar equation given in equation (5.7) the power of the transmitted signal decreases with the fourth power of distance [57].

$$r = \frac{\lambda}{4\pi^2} \sqrt[4]{\frac{P_o \cdot G_1^2 \cdot G_e^2}{kT_o \cdot B \cdot F \cdot SNR \cdot D}} \tag{5.7}$$

In equation 5.7, P_o is the transmitted power, G_1 and G_e are the interrogator and SAW tag gains, λ is the EM wavelength, kT_o is the thermal noise of the system, B is the system bandwidth, F is the noise figure, SNR is the signal to noise ratio and D is the sensor insertion loss. The sensor insertion loss is frequency dependent and has a profound effect on the readout range; keeping all other parameters constant and reducing the device loss by only 3 dB would result in an increase in maximum readout distance of 16%.

5.2.1 Single Frequency CDMA Tags

A typical single frequency CDMA tags consists of a a narrow band SAW transducer connected to the antenna with a series of short reflectors with the same center frequency wavelength spaced at varying distances from the transducer. The interrogation signal contains a single frequency RF burst that generates a SAW that is partially reflected from each of the N inline reflectors.

In Fig. 5.7, since all the reflectors are in-line the power received by each reflector decreases geometrically as the wave propagates through subsequent reflectors. The tag impulse response is a series of pulses with geometrically decaying amplitudes corresponding to the physical location of the reflectors. This reflector power loss contributes to the losses in the tag thereby limiting the range of operation. For a typical ID-tag operating in the 1 GHz region, the tag loss is approximately 50dB and accounting for path loss from the radar equation the overall attenuation between the transmitted impulse and received tag response becomes more than 100 dB for short distances of 1/2 meter[8].

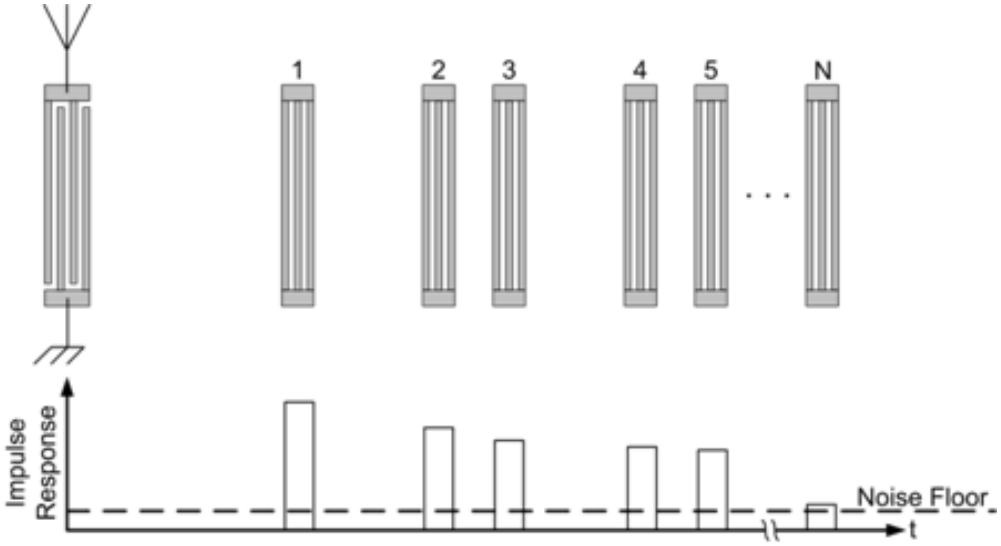

Figure 5.7: Schematic of a single frequency SAW CDMA ID Tag [3]. All the reflectors are in-line in a single track which geometrically decreases the power received by subsequent reflectors.

5.2.2 Orthogonal Frequency Coded Tags

OFC is a coding technique used to spread the signal bandwidth between several frequencies that are defined to be orthogonal to each other. A result of the orthogonality condition is that the different frequency reflectors are transparent to each other thus minimizing reflector losses. The orthogonality condition as it applies to the OFC SAW technique has been defined by Malocha et al [58]. Consider a time limited, nonzero time function h(t) defined in 5.8:

$$h(t) = \sum_{n=0}^{N-1} \varphi_n(t).rect\left(\frac{t}{\tau}\right) \tag{5.8}$$

where,

$$\varphi_n(t) = a_n \cdot cos\left(\tfrac{n\pi t}{\tau}\right)$$

$$rect(x) = \begin{cases} 1 & \text{if } |x| \leq 0.5 \\ 0 & \text{otherwise} \end{cases} \tag{5.9}$$

If the function $\varphi_n(t)$, represents a complete orthogonal basis set, then the members of the basis set are defined in [58] to be orthogonal over a given time interval if

$$\int_{-\frac{\tau}{2}}^{\frac{\tau}{2}} \varphi_n(t) \cdot \varphi_m(t)dt = \begin{cases} K_n & \text{if } n = m \\ 0 & n \neq m \end{cases} \tag{5.10}$$

This yields two functional descriptions for the orthogonal time functions which have the forms:

$$h_1(t) = \sum_{n=0}^{N} a_n cos\left(\frac{2n\pi t}{\tau}\right) rect\left(\frac{t}{\tau}\right) \tag{5.11}$$

$$h_2(t) = \sum_{m=0}^{M} b_m cos\left(\frac{(2m+1)\,\pi t}{\tau}\right) rect\left(\frac{t}{\tau}\right) \tag{5.12}$$

In the equations (5.11) and (5.12) each of the cosine terms in the summations represent a time-gated sinusoid represented in the frequency domain by Sampling functions whose local center frequencies are given by:

$$f_n = \frac{n}{\tau} \;\; and \;\; f_m = \frac{(2m+1)}{2\tau} \tag{5.13}$$

In equation (5.13), the orthogonality requires that $f_n \cdot \tau$ must be an integer with integer number of wavelengths at f_n and integer number of half wavelengths at f_m. This generates a set of sinusoidal functions having frequency responses where the nulls and peaks of adjacent frequencies coincide. Fig. 5.8 is a set of seven Sampling function frequencies normalized to center frequency that form an orthogonal basis set which satisfies the orthogonality conditions defined by equations (5.10), (5.11) and (5.12). In Fig. 5.8(a) the time responses of the chips in the basis set are contiguous and are representative of a linear stepped chirp.

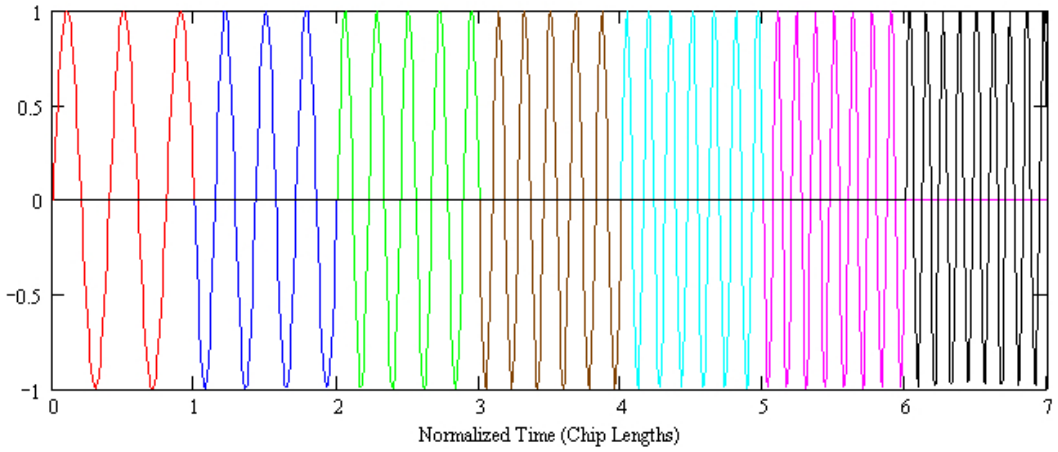

(a)

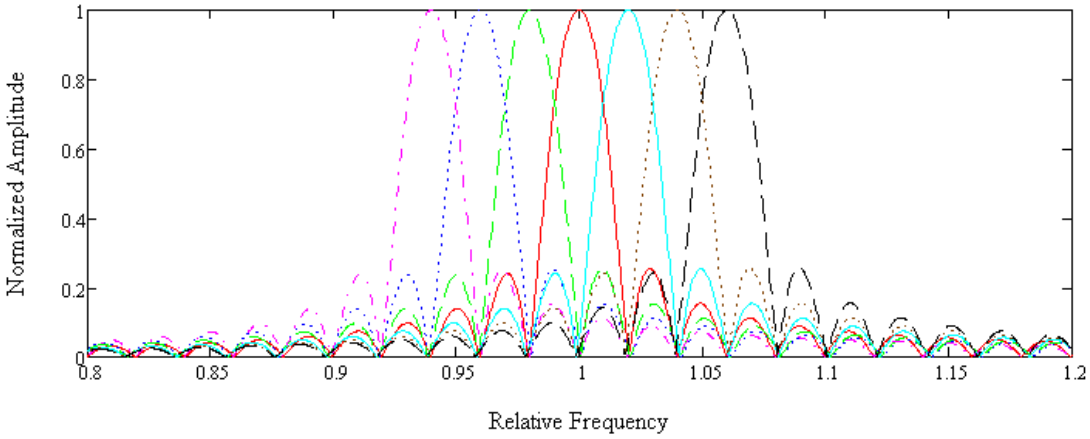

(b)

Figure 5.8: Time and frequency responses of an orthogonal frequency coded stepped chirp response. The chip lengths are kept constant so that the chip frequency responses have the same bandwidths. The time responses have integer number of half wavelength cycles. Time axis is normalized to chip length and the frequency axis is normalized to the center frequency of the chirp bandwidth.

The orthogonality functional descriptions can be used to define a desired signal that has both time and frequency diversity and provides a systematic way of implementing a code in a SAW device embodiment. For a time function $g_{bit}(t)$ with the bit time length τ_B divided into integer number of chips τ_c long, such that $\tau_B = J \cdot \tau_c$ where *J* is the number of chips, the bit is defined [3] as:

$$g_{bit}(t) = \sum_{j=1}^{J} w_j \cdot h_{cj}\left(t - j \cdot \tau_c\right) \tag{5.14}$$

In equation (5.14), w_j is the bit weight and $h_{cj}(t)$ is the definition of each chip. The functional form of the chip definition $h_{cj}(t - j \cdot \tau_c)$ is given in equations (5.11) or (5.12). For example, assuming the basis set in equation (5.12), the chip definition can be written as:

$$h_{cj}\left(t - j \cdot \tau_c\right) = \sum_{m=1}^{M} b_{jm} \cdot cos\left(\frac{(2m+1) \cdot \pi \cdot (t - j \cdot \tau_c)}{\tau_c}\right) \cdot rect\left(\frac{t - j \cdot \tau_c}{\tau_c}\right) \tag{5.15}$$

Letting $b_{jm} = 0$ for all *m*, except $m = C_j$ where $1 \leq C_j \leq M$, the chip definition is then,

$$h_{cj}\left(t - j \cdot \tau_c\right) = b_j \cdot cos\left(\frac{(2C_j+1) \cdot \pi \cdot (t - j \cdot \tau_c)}{\tau_c}\right) \cdot rect\left(\frac{t - j \cdot \tau_c}{\tau_c}\right) \tag{5.16}$$

In equation (5.16) each chip has a single local carrier frequency $f_{cj} = \frac{2C_j+1}{2 \cdot \tau_c}$ and b_j is the chip weight. The following design rules are used to implement the desired time function [3]:

- $b_j = \pm 1$ for all j
- the bit null bandwidth is $BW_{bit} = J \cdot 2 \cdot \tau_c^{-1}$
- C_j is a sequence of unique integers which means that f_{cj} form a contiguous, non-repetitive set

Although the rules require that the adjacent chips be contiguous in frequency, they do not require them to be contiguous in time. This allows the chips to shuffled in the time domain allowing for frequency coding of the bit.

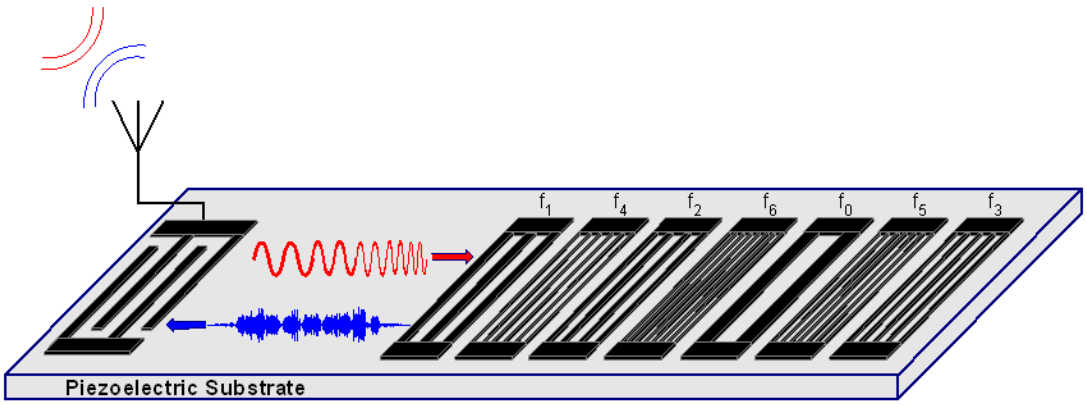

(a)

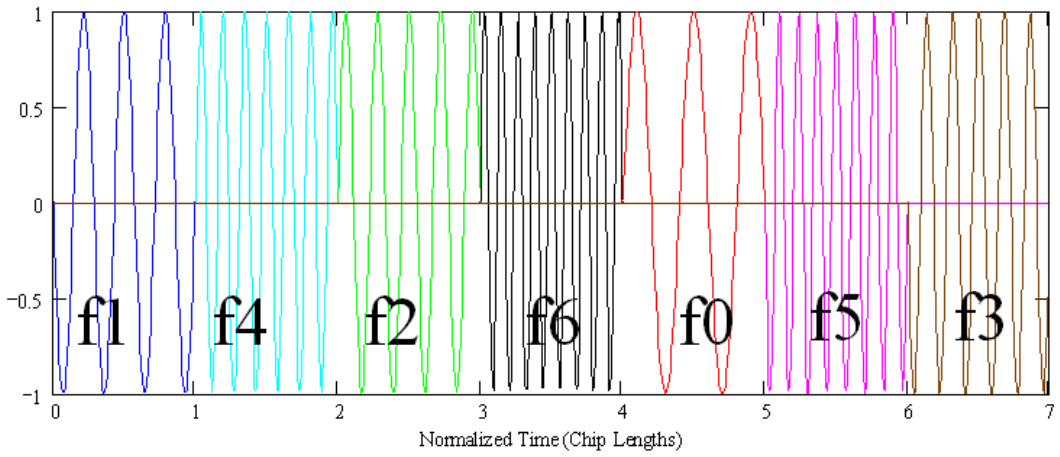

(b)

Figure 5.9: Schematic of a 7 chip SAW OFC RFID tag; the frequency responses of the reflector chips are orthogonal to each other. The figure shows the chirp interrogation signal and the returned noise-like signal which is the convolution of the chirp with the OFC.

Fig.5.8(a) is the time response of an OFC stepped chirp device; the chips are contiguous in the time domain and their time length is kept constant so that the chip frequency responses have the same bandwidths. In the frequency domain the chips are defined by a set of sin(x)/x functions where the peaks and nulls of adjacent frequency responses coincide, thus satisfying the orthogonality condition. The chips in the time domain can be shuffled so that they are non-contiguous to form a unique orthogonal frequency code as shown in Fig. 5.9(b). To implement the code in a SAW device, a wideband SAW transducer is bound by a set of coded reflectors on one side and the center frequency wavelengths of the reflector chips are chosen such that their frequency responses are orthogonal to each other.

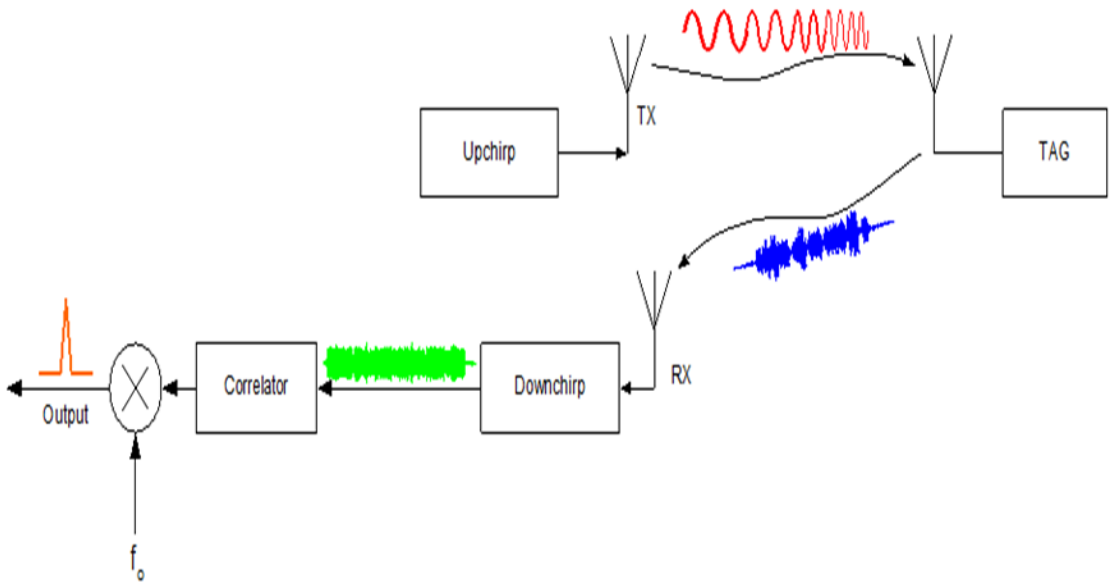

Figure 5.10: A schematic of the interrogation and correlation receiver approach for an OFC SAW reader.

The device can then be interrogated using a linear up-chirp response and the returned noise-like signal is the convolution of the chirp with the OFC. For a given power spectral density (W/Hz),

the chirp provides higher interrogation power as compared to a simple RF tone burst. A simple schematic of the transceiver is shown in Fig. 5.10, where the OFC tag is interrogated using an up-chirp signal. The returned signal at the receiver is first match-filtered through a down-chirp and then correlated with the OFC matched filter to extract the associated sensor information. The details of OFC SAW RFID sensor implementation, design examples and considerations and comparison to psuedo-OFC for reduced device losses and improved correlation properties will be discussed in the next chapter.

CHAPTER 6
ORTHOGONAL AND PSUEDO-ORTHOGONAL FREQUENCY CODED SAW SENSORS

The concept of OFC SAW sensor tag was introduced in chapter 5. In this chapter the implementation of OFC sensor and design considerations will be presented. The optimization of device losses, bandwidth and correlation properties and the development of the psuedo-orthogonal frequency coded (P-OFC) device will be discussed and compared to the OFC device. The motivation of this work is to improve the tag's readable distance, by improving insertion loss and reducing the device fractional bandwidth so that a more functional antenna can be used.

6.1 Implementation of OFC SAW Sensor

As stated in the previous chapter the OFC waveform is implemented in a SAW device using reflector gratings with different periodicities that correspond to the frequency code. Shown in Fig. 6.1 is a picture of an OFC SAW device being probed; the device has a center frequency of 250 MHz and has eight OFC chips with an overall bandwidth of 40 MHz yielding a fractional bandwidth of 16%. The chip time length, τ_c is held constant at 200ns for each chip, this results in each reflector having a different number of electrodes as the reflector center frequency changes. The equation

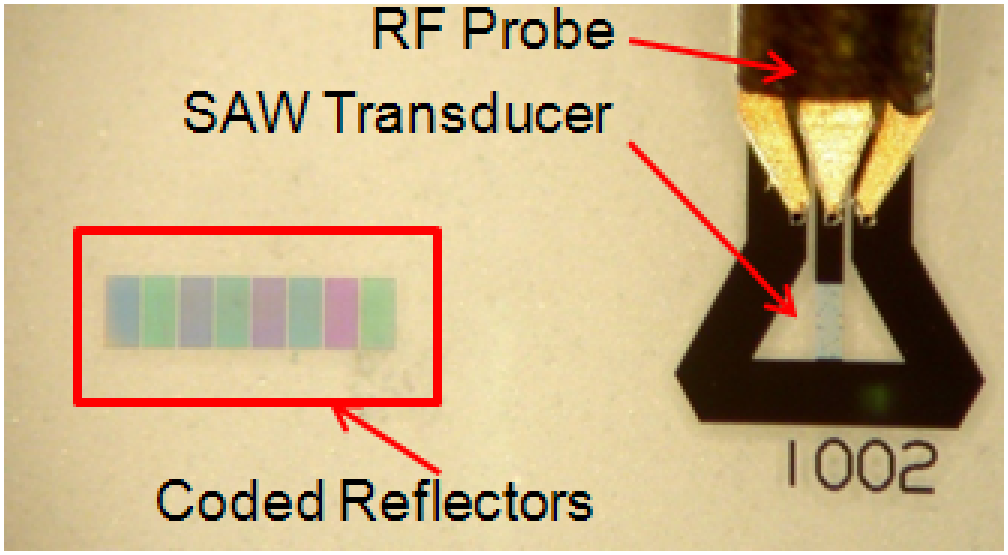

Figure 6.1: Picture of an 8-chip OFC SAW device being probed. The colors of the SAW reflectors is due to the interference pattern from the different center frequencies of the SAW reflectors

used to find the reflector electrode counts is [3],

$$N_j = \tau_c \cdot f_j \tag{6.1}$$

The electrode count is directly proportional to the chip frequency, i.e. as N_j increases, f_j increases. For a given device with the same metal thickness on all reflectors, the normalized metal thickness will be higher on the higher frequency chips. At first harmonic operation reflectivity increases with increasing normalized metal thickness, therefore the highest frequency chip will have the highest amplitude. If the chips are placed inline, propagation loss as the wave propagates under the grating electrodes can also affect the amplitude of the reflector response. As discussed in chapter 4, the propagation loss is proportional to the square of the frequency and has a more

significant effect at high frequencies. As an example, shown in Fig. 6.2 is the COM simulated shorted reflector chip responses of the eight chip OFC device in Fig. 6.1.

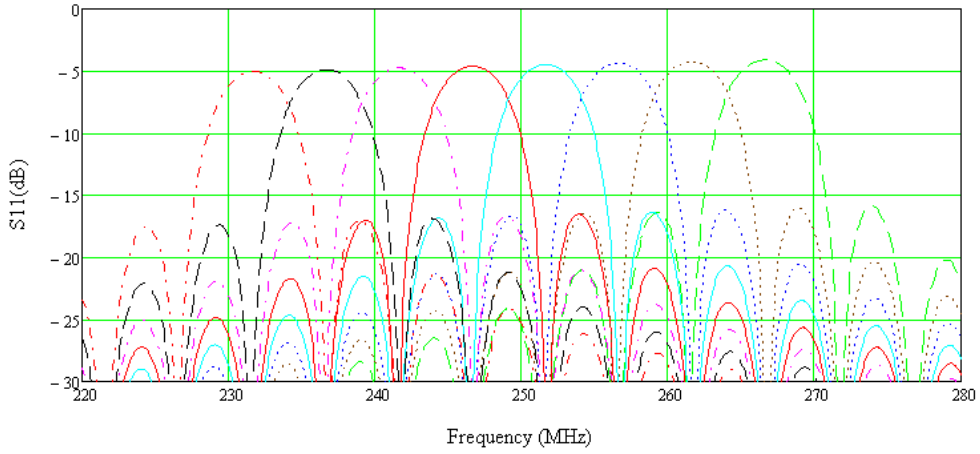

Figure 6.2: Shorted reflector responses of the eight chip OFC SAW tag shown in Fig. 6.1. Each reflector has 50 electrodes, the reflector loss is approximately 5dB per chip

The experimental and COM simulated S_{11} frequency and time responses of the OFC SAW tag are shown in Fig. 6.3. The ripple in the frequency response is the reflection from the reflector chips. The chip responses are amplitude modulated by the transducer passband response and the chips, f_1 and f_2 that are closer to the edge of the transducer passband consequently have lower amplitude. The center frequencies of the reflector chips are f_1=232 MHz, f_2=237 MHz, f_3=242 MHz, f_4=247 MHz, f_5=252 MHz, f_6=257 MHz, f_7=262 MHz, and f_8=267 MHz. The chips are non-contiguous in time and the order of the frequency chips is indicated in the time domain response.

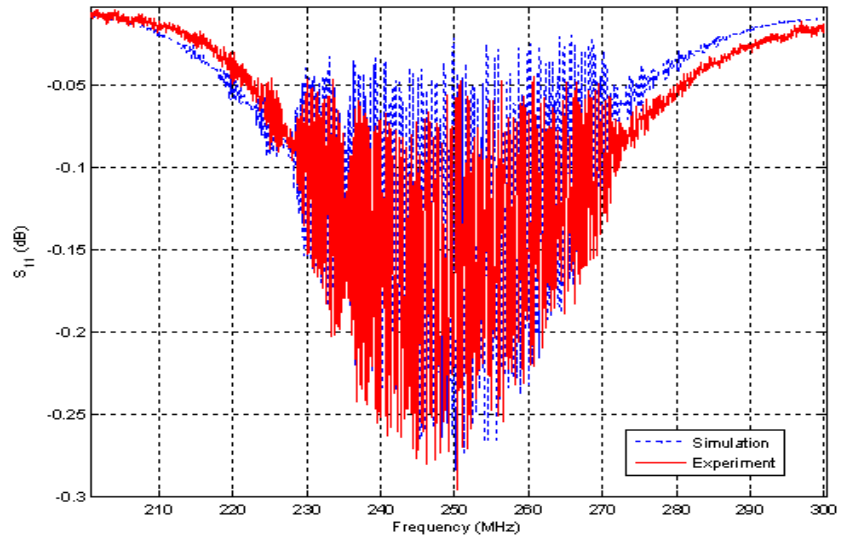

(a)

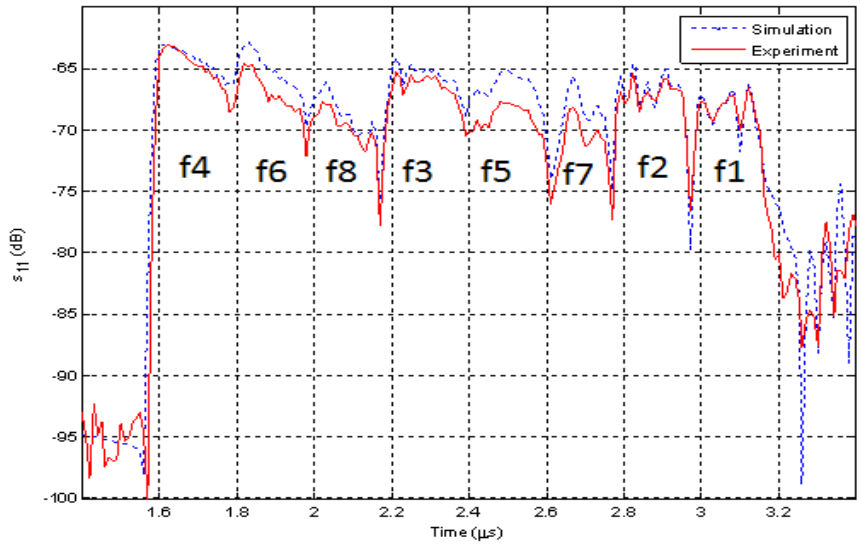

(b)

Figure 6.3: Experimental and COM simulated S_{11} (a) frequency and (b) time responses for an 8-chip OFC SAW device. The overall device bandwidth is 40 MHz.

As stated in chapter 5, the OFC device is interrogated using a linear up-chirp and the received signal is then filtered through a down-chirp and the recovered OFC signal is then correlated using a matched filter. The reflector bank is approximated by a rect function in the time domain and can be matched filtered using a simple gated sine wave given as [59, 3]

$$h_{mf} = \sum_{j=1}^{N} Rect\left(\frac{t - \frac{\tau_c}{2} - \tau_{p_j}}{\tau_c}\right) \cdot sin\left(2\pi f_j \left(\frac{t - \frac{\tau c}{2} - \tau_{p_j}}{\tau_c}\right)\right) \tag{6.2}$$

where N is the number of reflector chips, f_j is the frequency fo the j^{th} chip, τ_{p_j} is the position of the j^{th} chip and τ_c is the chip length which is held constant for all the chips. The correlation output is the convolution of the matched filter time function and the OFC signal and is given as:

$$h_{correlation}(t) = h_{mf}(t) * h_{OFC}(t) \tag{6.3}$$

where h_{OFC} is the received OFC signal. External stimuli such as temperature change varies the SAW velocity and scales the frequency and time domain responses. To detect the SAW velocity change and thus the temperature, a software adaptive matched filter technique is used. A set of matched filters with scaled frequency and time functions corresponding to varying temperatures are used to generate the output correlation [60, 59] as shown in equation (6.4),

$$h_{correlation}(t) = h_{mf}(\alpha \cdot t) * h_{OFC}(t) \tag{6.4}$$

where α is the frequency scaling factor. The temperature of the sensor is detected by sweeping the scaling factor, α, over a wide enough range to maximize the correlation output, $h_{correlation}(t)$. When the sensor is at the design temperature α=1 and it changes linearly at -94 ppm/^{o}C for YZ $LiNbO_3$. The α for which $h_{correlation}(t)$ is maximum corresponds to the sensor temperature [7, 60, 59]. As an example, Fig. 6.4 shows the auto-correlation and the matched filter correlation of the OFC device from the above example.

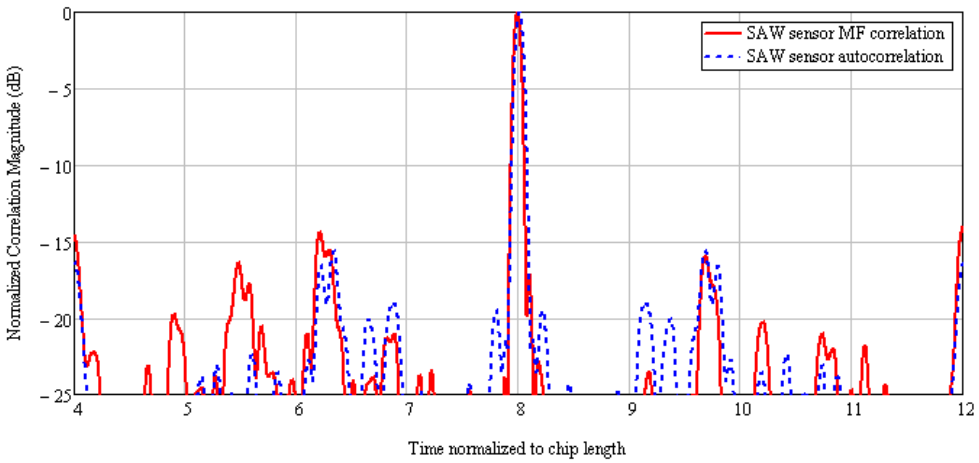

Figure 6.4: Auto-correlation and matched filter correlation of the OFC device with eight chips. Magnitude is normalized to maximum correlation and time is normalized to chip time length.

6.2 Development of Psuedo-Orthogonal Frequency Coding (P-OFC)

OFC tags, use frequency coded reflectors to spread the signal bandwidth and introduce processing gain [58, 61, 62], in the previous example since the bandwidth is divided between eight chips, the processing gain calculated from equation (5.2) is 9dB. The goal of this work was to improve the tag readable distance, by improving insertion loss and to reduce the device fractional bandwidth so

that a more functional antenna could be used. In general, the use of long reflector banks increases net reflectivity thereby decreasing the tag insertion loss and reducing overall fractional bandwidth. However, a long reflector also results in a time response that is very long. This results in an undesired overlap of multiple chips in the time domain and a significant frequency domain spectral overlap between chips, that causes degradation of the ideal or desired chip amplitude and phase information.

In order to overcome the pulse distortion due to spectral overlap of chips a psuedo-orthogonal frequency coding (P-OFC) scheme was investigated. In P-OFC the center frequencies for the long reflectors are redefined to reduce the intra-chip interference and optimize the use of bandwidth.

Optimization of tag design parameters, such as the number of electrodes in each reflector chip, tag bandwidth, chip orthogonality conditions and the chip correlation and cross-correlation properties will be discussed. Additionally, the correlation properties of the new P-OFC condition is compared to the correlation properties of the classical OFC device. A comparison of tag performance as compared to OFC is presented.

In general, the use of long reflector banks increases net reflectivity thereby decreasing the tag insertion loss and reducing overall fractional bandwidth. However, a long reflector also results in a time response that is also very long, similar to a sin(x)/x response exhibiting a stored energy time impulse occurring at τ_c, where τ_c is the chip length. This results in an undesired overlap of multiple chips in the time domain and a significant frequency domain spectral overlap between chips, that causes degradation of the ideal or desired chip amplitude and phase information. The chips ring much longer in time and no longer follow the orthogonality in the time domain as defined

in Chapter 5 and are therefore called psuedo-orthogonal. In the next few sections of this chapter, the P-OFC chips will be defined and the best time and frequency spacing are chosen using the chip correlation and cross-correlation properties. Comparison of OFC and P-OFC is devices was employed to guage improvements in insertion loss, overall bandwidth and correlation properties.

6.2.1 Effect of Reflector Chip Length on Tag Performance

As shown in Fig 6.5(a), as the reflector length increases, thereby increasing the product $Ng \cdot r$, the reflected power increases and the null-bandwidth of the frequency response shrinks. Thus, increasing the reflector length is desirable as this improves the net reflectivity, consequently improving insertion loss of the device. Also, another effect of increasing the reflector length is to reduce overall device fractional bandwidth and thus improve spectral efficiency of the tag. As the reflector length increases its time response approaches a sin(x)/x response with an impulse response occurring at the chip length τ_c shown in Fig. 6.5(b) due to the stored energy effect, which results in some intersymbol interference in the time domain.

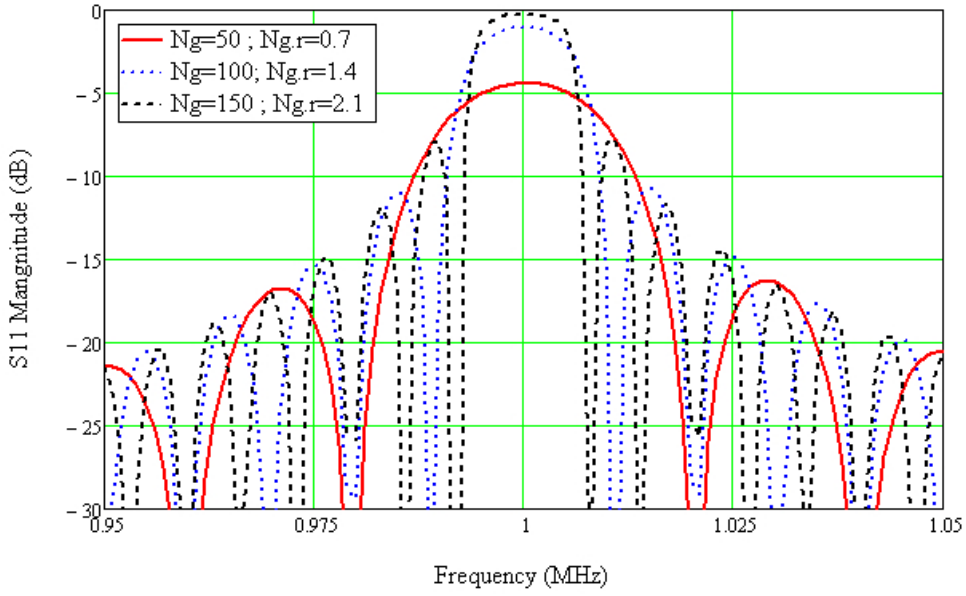

(a)

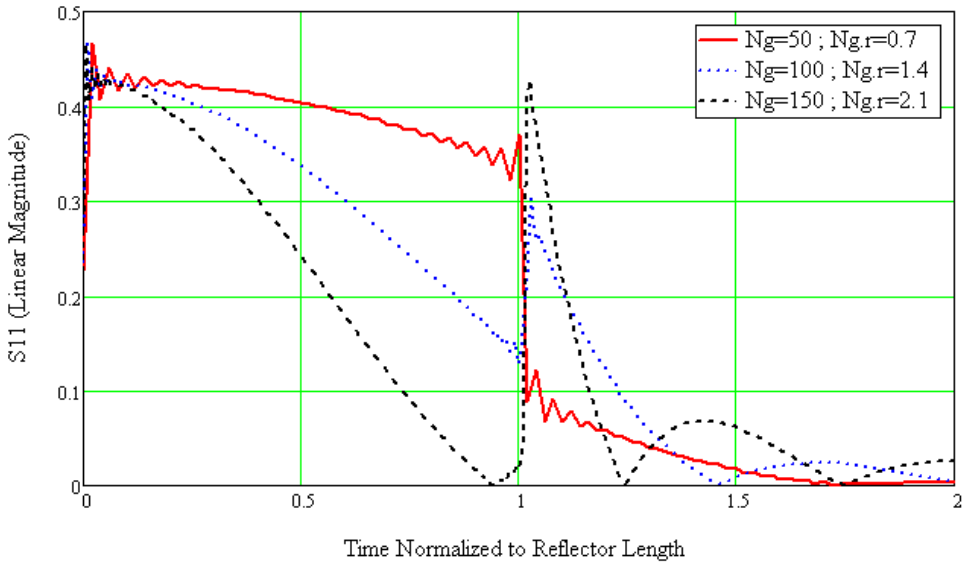

(b)

Figure 6.5: (a) Frequency and (b) time responses of an reflector chip of varying reflector lengths. A reflectivity of 1.4% is assumed for YZ-$LiNbO_3$. The insertion loss of the frequency response increases with increasing $Ng \cdot r$ while the null-bandwidth decreases, and the time response approaches a sin(x)/x type response with increasing $Ng \cdot r$. As $Ng \cdot r$ increases, the stored energy in the reflector due to intra-chip reflections increases and is dissipated later in time resulting in an impulse occuring at τ_c.

Another effect of the increased reflector length is that the main lobe of the frequency response of the reflector approaches a more brick-wall like response, thereby increasing the frequency overlap of two adjacent frequency reflectors and distorting the frequency response of the tag. In order to prevent this spectral domain overlap and loss of tag information, the orthogonality condition needs to be redefined. The first attempt was to redefine orthogonality such that the nulls of two adjacent frequencies coincide as shown in Fig. 6.6(b) thus eliminating the frequency domain overlap of energy between adjacent frequency reflectors in OFC, as depicted in the shaded region in Fig.6.6(a).

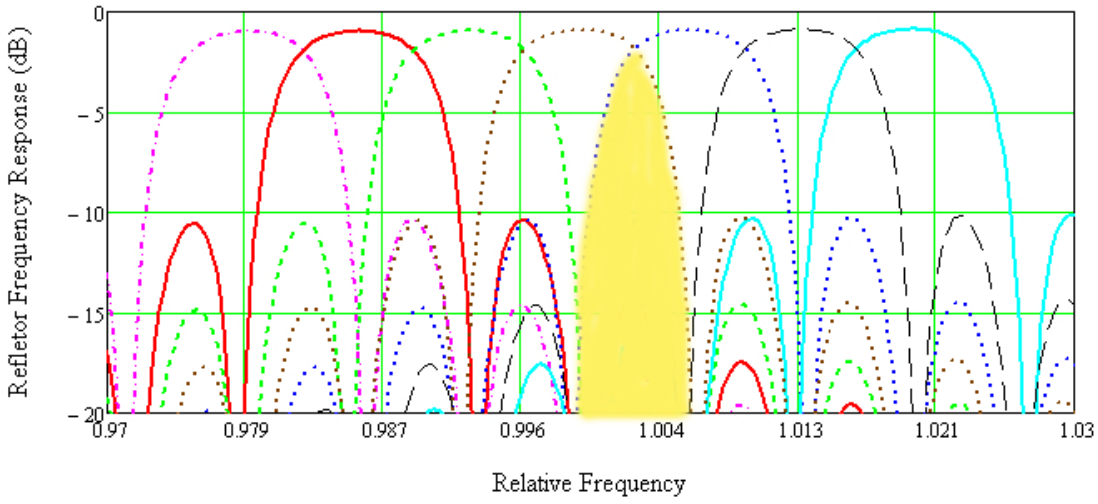

(a)

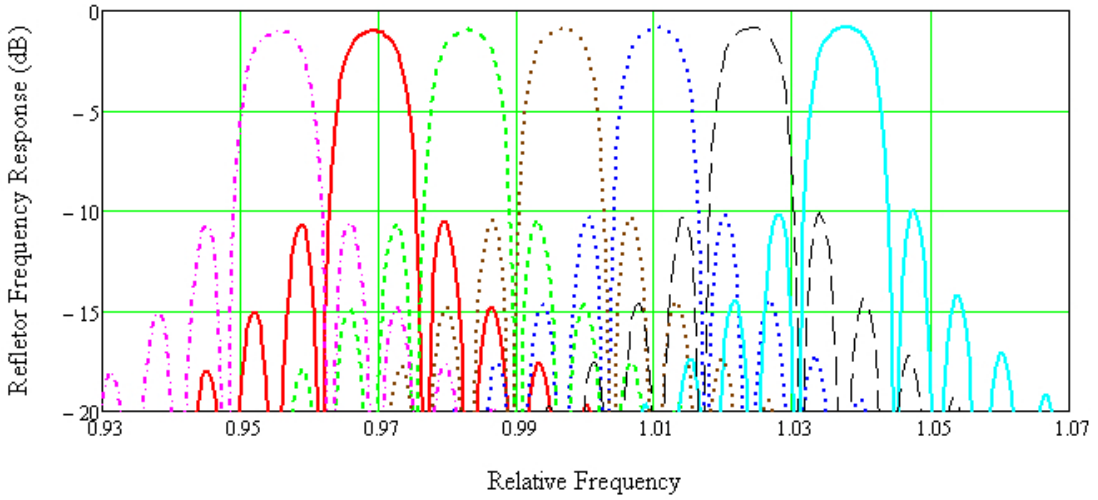

(b)

Figure 6.6: Frequency responses of 7 reflector chips with 150 electrodes using OFC and P-OFC with a reflectivity of 1.4% assumed for YZ-$LiNbO_3$. OFC shows a significant overlap of energy between two adjacent frequency reflectors (shown by the shaded region) which causes distortion of the tag frequency response.

The solid curve in Fig. 6.7 shows the loss of reflected power per chip versus chip length for strip reflectivity of 1.4% assumed for YZ-$LiNbO_3$for a metallization ratio of 0.5. As the chip length approaches 150 electrodes $Ng \cdot r = 2.1$, the loss in reflected power is at approximately 1 dB and appraoching saturation thereafter. The absolute 4 dB bandwidth of a single chip shrinks from 5 MHz at $Ng \cdot r = 0.7$ to 1.67 MHz at $Ng \cdot r = 2.1$ which is a reduction in bandwidth by a factor of 3.

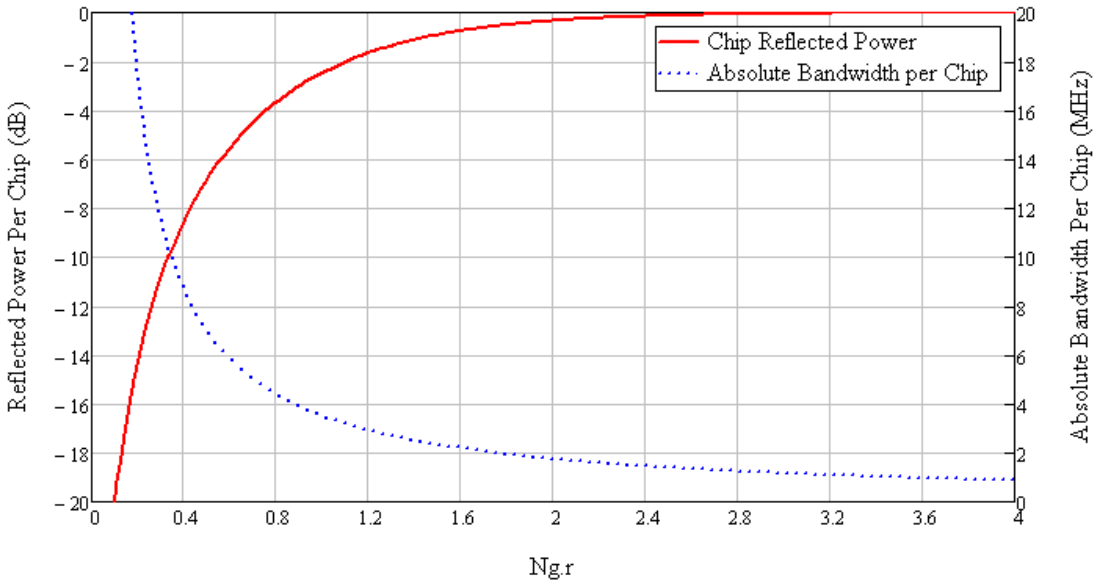

Figure 6.7: COM prediction of the insertion loss of a single chip SAW reflector grating with r=1.4% versus the product $Ng \cdot r$ is shown by the solid curve which approaches 1dB at $Ng \cdot r = 2.1$ or 150 electrodes. The absolute 4 dB bandwidth of a single chip at a center frequency of 250 MHz (shown in the dotted curve) reduces from 5 MHz at $Ng \cdot r = 0.7$ to 1.67 MHz at $Ng \cdot r = 2.1$

6.2.2 Orthogonality Condition for P-OFC

In order to use the long reflectors, to enhance spectral efficiency and reduce the reflector loss, the orthogonality design criteria has been redefined. As shown in Fig. 6.5(a), the main lobe of the frequency response of a reflector chip starts to approach a rect function shape as Ng.r increases. The orthogonality condition defined for OFC in eq(5.13) is defined such that for any given basis set, $f_n \cdot \tau$ must be either an odd or an even integer number of wavelengths at frequency f_n, i.e. $n = 1, 3, 5, ...$ or $n = 2, 4, 6, ...$ Similarly, $f_m \cdot \tau$ must be either an or an odd or an even integer number of wavelengths at frequency f_m, i.e. $m = 1, 3, 5, ...$ or $m = 2, 4, 6, ...$ This new criteria produces a set of Sampling functions in the frequency domain whose nulls coincide resulting in minimal spectral overlap as shown in Fig.6.6(b). The null bandwidth of these sampling functions is $2 \cdot \tau^{-1}$ and since the nulls of adjacent frequency responses coincide the center frequencies in a given basis set are separated by $2 \cdot \tau^{-1}$ as well.

Shown in Fig. 6.6 is a comparison of a set of 7 OFC chips (Fig. 6.6(a)) and a set of 7 P-OFC chips (Fig. 6.6). The set of frequencies that use the orthogonal coding show a large overlap in the frequency response of adjacent frequency reflectors causing distortion of the device response and therefore destruction of the orthogonality condition. The set of frequencies in the psuedo-orthogonal set however, have minimal overlap between adjacent frequency responses. Due to the stored energy effect, the time impulse response length of each chip continues to dissipate energy beyond the actual chip length which creates some intersymbol interference in the time domain which can affect the correlation properties. In order to avoid this intersymbol interference the chips

can be spaced further away from each other so as to allow most of the energy from the multiple reflections within a chip to dissipate. This time separation, τ_s, is dependent on the number of electrodes in a chip. As an example the case of 150 electrodes is considered here, since the P-OFC devices built in this dissertation had 150 electrodes. The time separation, τ_s, in the case of 150 electrodes was $1.75\tau_c$. The energy dissipated beyond τ_s is very small and can be ignored. The P-OFC chips do not strictly obey orthogonality as compared to the short (50 electrode or less) OFC-chips, however the cross-correlation properties for long reflectors are enhanced by using the P-OFC frequency and time spacing as will be seen in the next section.

Beyond 150 electrodes per reflector the energy in the chip beyond τ_c starts to become significant due to the stored intrachip reflections and the increase in reflected power is insignificant. The time domain pulse shape for the reflector can be approximated using a Hamming window. In order to include the energy in the impulse in the region from τ_c to $1.2\tau_c$ and to account for the 180 degree phase change at τ_c , for reflectors between with 150 electrodes the time function, $\mathrm{h}_{POFC}(\mathrm{t})$, can be defined using a piecewise function:

$$h_{POFC}(t) = \sum_{n=0}^{N-1} \varphi_n(t) \cdot env\left(\frac{t}{\tau_c}\right) \tag{6.5}$$

where,

$$\varphi_n(t) = a_n \cdot cos\left(\frac{n\pi t}{\tau}\right)$$

$$env(x) = \begin{cases} 0.54 + 0.46 \cdot cos\left(\frac{2\pi t}{2\tau_c}\right) & \text{if } 0 \leq x \leq 1\tau_c \\ -2e^{(-\frac{t}{\tau_c}^7)} & \text{if } 1 \leq x \leq 1.2\tau_c \\ 0 & \text{otherwise} \end{cases} \tag{6.6}$$

As an example the reflector chip response for a 150 electrode grating is shown in Fig. 6.8.

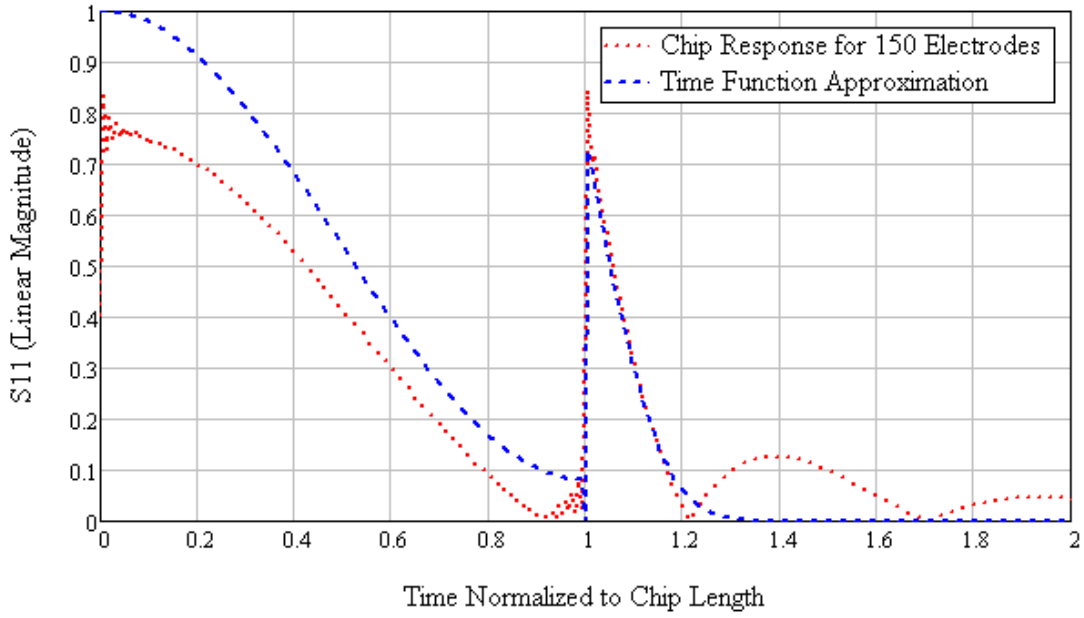

Figure 6.8: Time response of a reflector chip on YZ $LiNbO_3$ with 150 electrodes and its time function approximation.

The energy in the impulse occurring after τ_c can be ignored with no severe consequence to the device correlation. A comparison of the auto-correlation, and matched filter correlation using the Hamming window approximation per chip for a five chip P-OFC device is shown in Fig. 6.9.

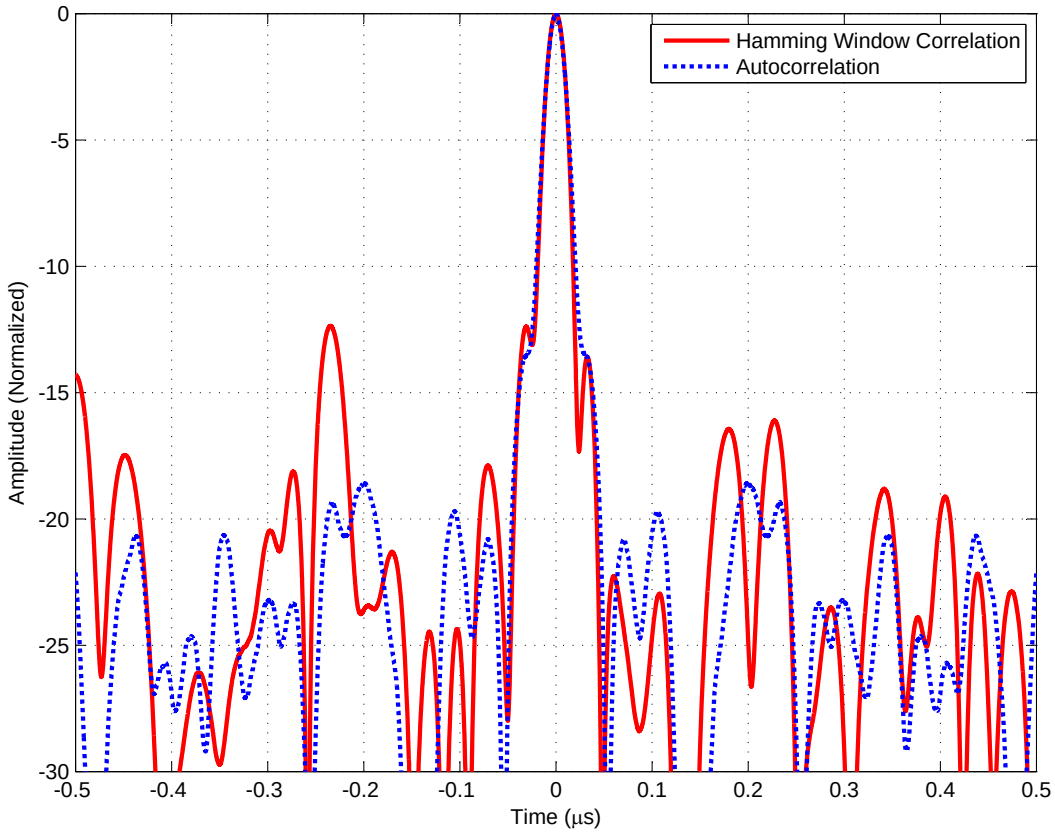

Figure 6.9: Comparison of the device auto-correlation, and matched filter correlation using the Hamming window approximation for a 5 chip P-OFC device.

Thus if the stored energy impulse is ignored, the chip time function can be written as:

$$\varphi_n(t) = a_n \cdot cos\left(\frac{n\pi t}{\tau_c}\right)$$
$$env(x) = \begin{cases} 0.54 + 0.46 \cdot cos\left(\frac{2\pi t}{2\tau_c}\right) & \text{if } 0 \leq x \leq 1\tau_c \\ 0 & \text{otherwise} \end{cases} \tag{6.7}$$

The P-OFC reflectors shown in Fig. 6.6(b) have no spectral overlap in the main lobes of the adjacent frequency chips. Although this substantially minimizes intra-chip reflections in the frequency domain and yields reduced pulse distortion, the bandwidth of the device is still not optimized. An attempt was made to optimize the spectral spacing of the chips based on their correlation and cross-correlation properties. For an OFC device the center frequencies of adjacent frequency chips are $1/\tau_c$ MHz apart. In the P-OFC case in Fig. 6.6(b), center frequencies of the adjacent frequency chips are $2.4/\tau_c$ MHz apart for the case with 150 electrodes, and changes proportional to the null bandwidth of the reflector chips which can be found using a COM reflector equations. Comparing the correlation properties of adjacent frequency reflector chips it was found that the ideal spacing for adjacent frequency reflector chips with 150 electrodes is $1.6/\tau_c$ MHz for optimal spectral efficiency. The correlation properties are discussed in the next section and compared for each of the cases. The center frequencies of the chips are then determined using the following equation,

$$f_c = f_o + S \cdot \frac{C}{\tau_c} \tag{6.8}$$

where, f_c is the chip center frequency, f_o is the center frequency of the device, τ_c is the chip length, S is the frequency spacing factor and is 1 for OFC and 2.4 or 1.6 for the P-OFC cases in this work, and C is the P-OFC code sequence. For a seven chip code an example code sequence would be C=0,-2,-1,-3,+1,+2,+3, thus 0 corresponds to the center frequency chip, -1 to the next lower frequency and +1 to the next higher frequency etc.

The COM simulated reflector fractional bandwidth of an 8 chip tag versus single chip length is shown in Fig. 6.10, and it is observed that as the number of electrodes per chip increases the fractional bandwidth of the devices decreases and starts approaching saturation as the reflector length grows past 200 electrodes $Ng \cdot r = 2.8$. The plot can be split into four regions based on reflector behavior. Region I is the OFC region where $Ng \cdot r < 0.7$, the chips are short and are defined using OFC. As $Ng \cdot r$ increases beyond 0.7, the stored energy in the reflector chips starts to increase and the chips time response is longer than τ_c. This transition region exists between $0.7 < Ng \cdot r < 1.2$; here the reflector loss is still around 3 dB, the reflector dissipates some energy beyond the chip length and some pulse distortion may occur if the OFC chip definition is used. In the region $1.2 < Ng \cdot r < 2.5$, stored energy dissipation beyond τ_c is longer and starts causing pulse distortion requiring the P-OFC definition. For a 8 chip OFC device, it can be seen from Fig. 6.10, that with $Ng \cdot r = 2.1$, 150 electrode chip lengths, the loss of reflected power per chip is approximately 1dB and the overall fractional bandwidth of the device is at about 7%.

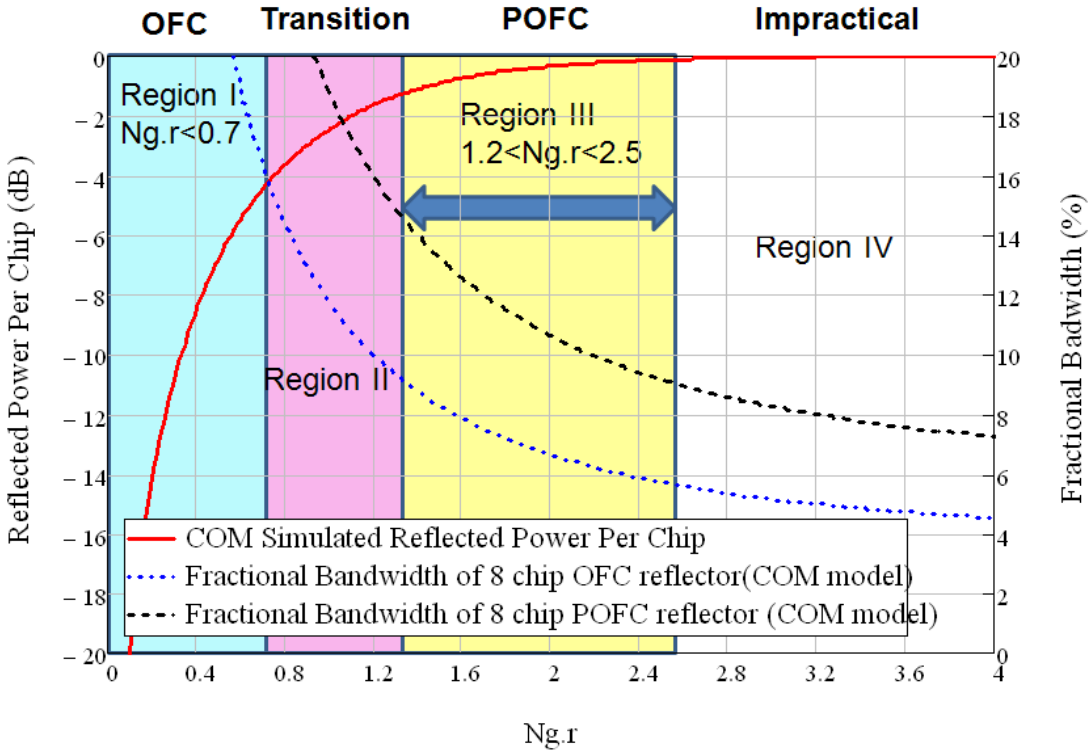

Figure 6.10: Insertion loss of a single chip versus the product $Ng \cdot r$ is shown by the solid curve which approaches 1dB at $Ng \cdot r = 2.1$ or 150 electrodes. The fractional bandwidth of an eight chip device using OFC and P-OFC definitions are shown. The OFC definition is used for $Ng \cdot r < 0.7$ while the P-OFC definition is used for $1.2 < Ng \cdot r < 2.5$.

6.3 Chip Correlation and Cross-Correlation Properties

The auto-correlations and cross-correlations are important parameters since they define the orthogonality of the chips to each other. The auto-correlation of the tag to its matched filter is used for tag detection in an OFC and it is critical that the individual chips and therefore the tag, have a robust auto-correlation peak relative to the cross-correlation responses. For two chips that are perfectly orthogonal to each other the cross-correlation should be zero where the peak of the auto-correlation occurs, indicating minimal interference from adjacent frequencies.

The auto-correlation of a chip represented by a time limited function f(t) is defined as:

$$R_f(\tau) = \int_{-\frac{\tau}{2}}^{\frac{\tau}{2}} f^*(t) f(t) dt \tag{6.9}$$

The fourier transform of the auto-correlation response is called the power spectral density and is a measure of the power distribution versus frequency. Similarly, the cross-correlation of two chips represented by time limited functions f(t) and g(t) are defined as:

$$R_{fg}(\tau) = \int_{-\frac{\tau}{2}}^{\frac{\tau}{2}} f^*(t) g(t) dt \tag{6.10}$$

If the two chips f(t) and g(t) are orthogonal to each other then their cross correlation $\mathrm{R}_{fg}(\tau)$ at $\tau = 0$ is zero, i.e.:

$$R_{fg}(\tau = 0) = \int_{-\frac{\tau}{2}}^{\frac{\tau}{2}} f^*(t) g(t) dt = 0 \tag{6.11}$$

Thus orthogonality is defined as:

$$\int_{-\frac{\tau}{2}}^{\frac{\tau}{2}} f^*(t)g(t)dt = \begin{cases} 1, & \text{g(t)=f(t)} \\ 0, & \text{g(t)}\neq \text{ f(t).} \end{cases} \tag{6.12}$$

Shown in Fig.6.11 is the auto-correlation of a reflector chip of varying lengths. The amplitude of the correlation pulse increases significantly, approximately 5 dB, as the chip length is increased from 50 electrodes to 100 electrodes and the compressed pulse width is reduced as a function of chip time length. The cross-correlation of a single OFC and different frequency separations of the P-OFC chip with its first and second adjacent frequency chips are shown in Fig. 6.12, Fig. 6.13, Fig. 6.14 and Fig. 6.15. All the correlation pulses are normalized to the maximum amplitude of the auto-correlation pulse shown in red. The frequency domain energy overlap between two adjacent frequency chips in OFC translates to degraded cross-correlation properties which in turn affects tag detectability in a multi-sensor environment.

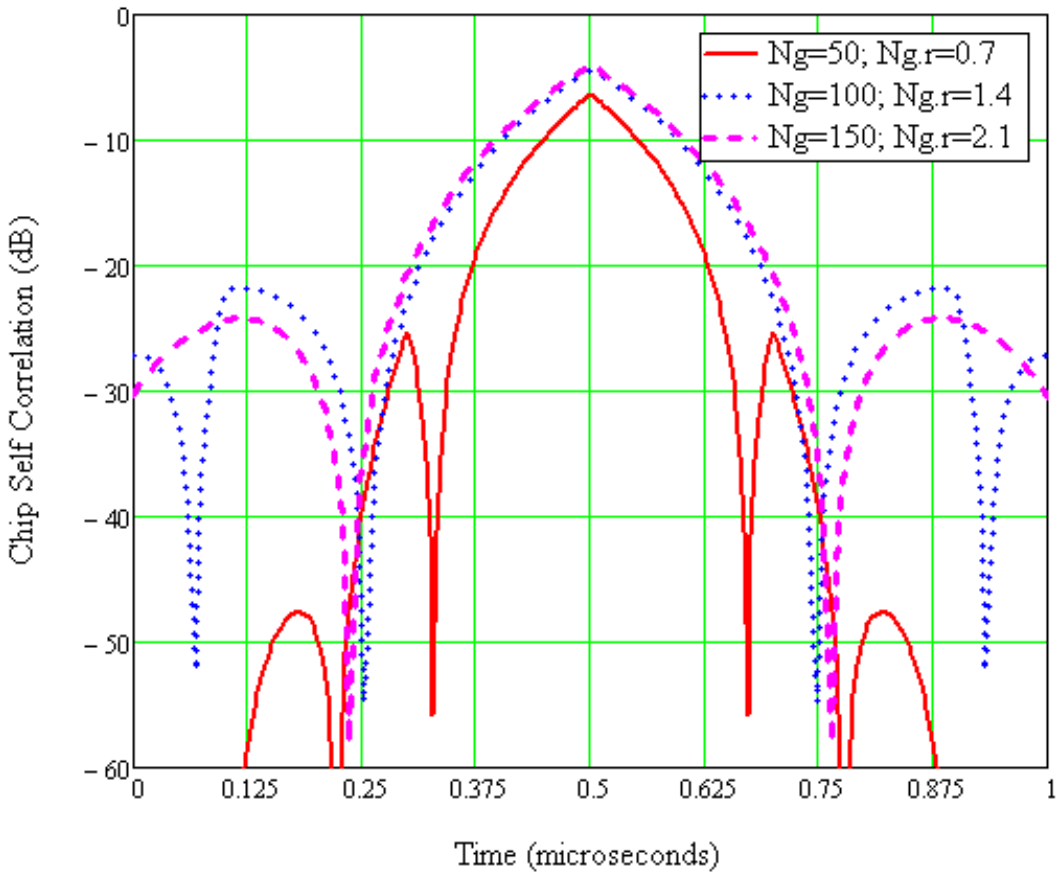

Figure 6.11: Auto-correlation of a reflector chip of varying lengths plotted versus time normalized to chip time length. The peak of the auto-correlation pulse increases from -17 dB for $Ng \cdot r = 0.7$ to -12 dB for $Ng \cdot r = 2.1$ and -11 dB for $Ng \cdot r = 2.8$.

The correlation and cross-correlation properties of OFC and P-OFC with varying frequency separation between adjacent chips is shown in the next few figures. Fig. 6.12 shows the auto-correlation (solid line) and the cross-correlation with the first (f_1 with f_2) and second (f_1 with f_3) adjacent OFC frequencies for reflector chips with 50 electrodes. The cross-correlation with the first (dotted line) and second adjacent (dashed line) chips produces a dip at the peak of the auto-correlation. Fig. 6.13, shows the auto-correlation and cross-correlation peaks for the case where the adjacent frequencies are separated using the the OFC orthogonality condition. As noted earlier in the chapter, the overlap of adjacent chip energy in the frequency domain causes severely degraded cross-correlation, producing a peak in the $f_1 * f_2$ cross-correlation that is only 7 dB lower than the auto-correlation peak. This is significantly improved in Fig. 6.14 and Fig. 6.15, where the frequency spacing of the chips are at $2.4/\tau_c$ and $1.6/\tau_c$ respectively. The cross correlations with the latter spacing are slightly degraded but this option allows for more optimal bandwidth use. Using the comparison of correlation properties is a good way to determine the ideal chip spacing. The best correlation and cross-correlation properties for individual chips is obtained when the chip spacing is at $2.4/\tau_c$ since the cross-correlation has lower energy at the auto-correlation peak. However, the spacing of $1.6/\tau_c$ further optimizes bandwidth use while still providing a cross-correlation that is at least 15 dB lower than the peak auto-correlation. Although the cross-correlations do not produce a null near the peak of the auto-correlation, the energy in the cross-correlations is fairly evenly distributed throughout the band of interest.

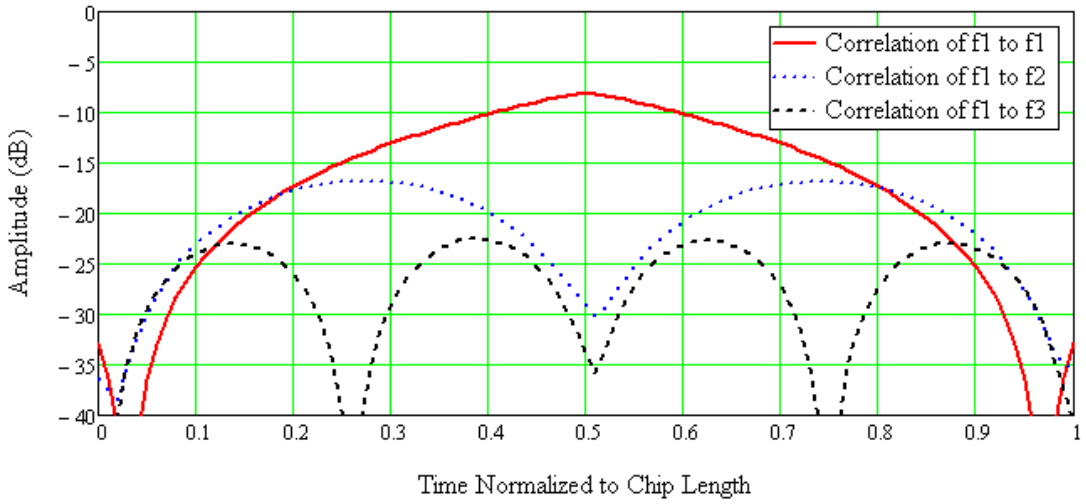

Figure 6.12: Cross-correlation of first and second adjacent OFC frequencies for reflector chips with 50 electrodes. Amplitude of all three correlation pulses are normalized to the peak of the auto-correlation shown in red and plotted versus time normalized to chip length.

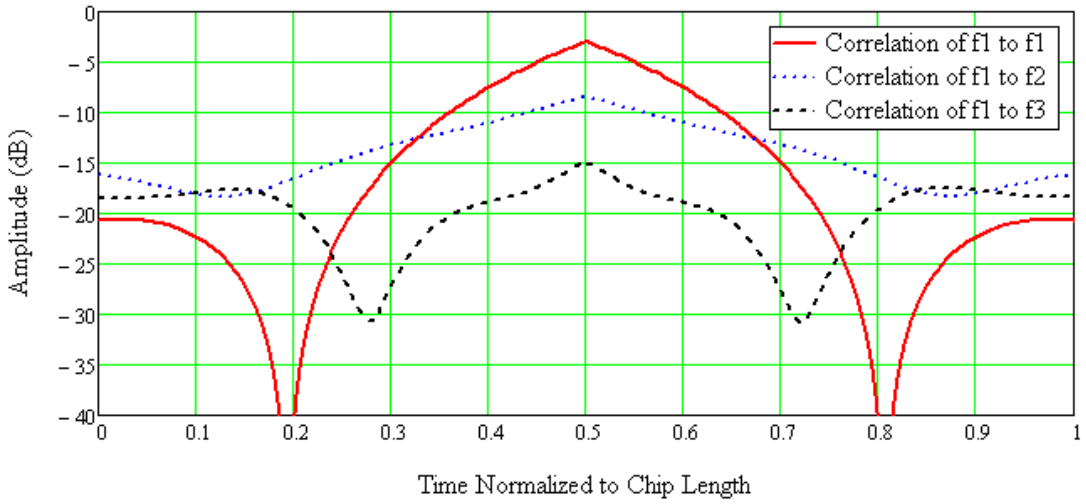

Figure 6.13: Cross-correlation of first and second adjacent OFC frequencies for reflector chips with 150 electrodes. Amplitude of all three correlation pulses are normalized to the peak of the auto-correlation of f_1 shown in red and plotted versus time normalized to chip length. There is significant energy in the cross-correlations due to the frequency distortion and overlap of long reflectors that no longer approximate the ideal OFC conditions.

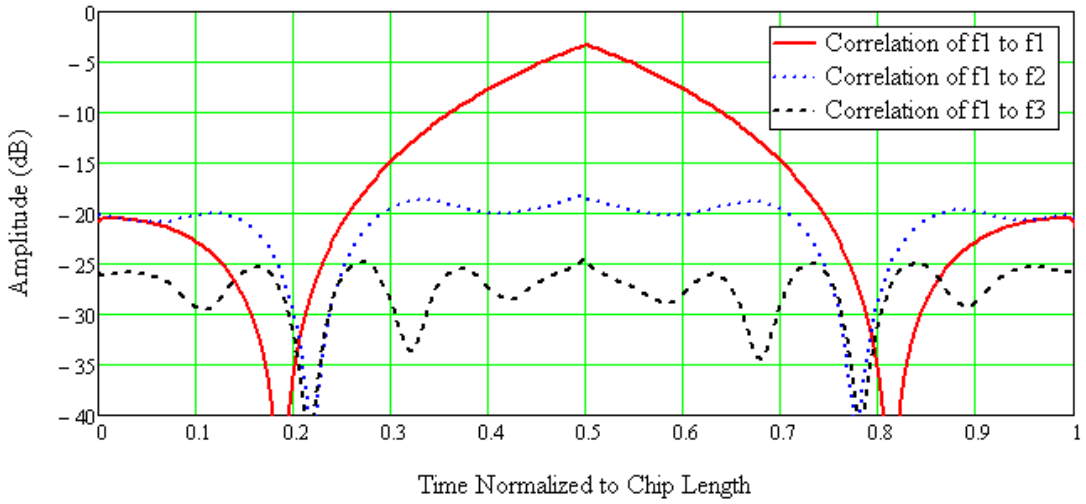

Figure 6.14: Cross-correlation of first and second adjacent P-OFC frequencies for reflector chips with 150 electrodes. The center frequency separation is $2.4/\tau_c$MHz. Amplitude of all three correlation pulses are normalized to the peak of the auto-correlation of f_1 shown in red and plotted versus time normalized to chip length.

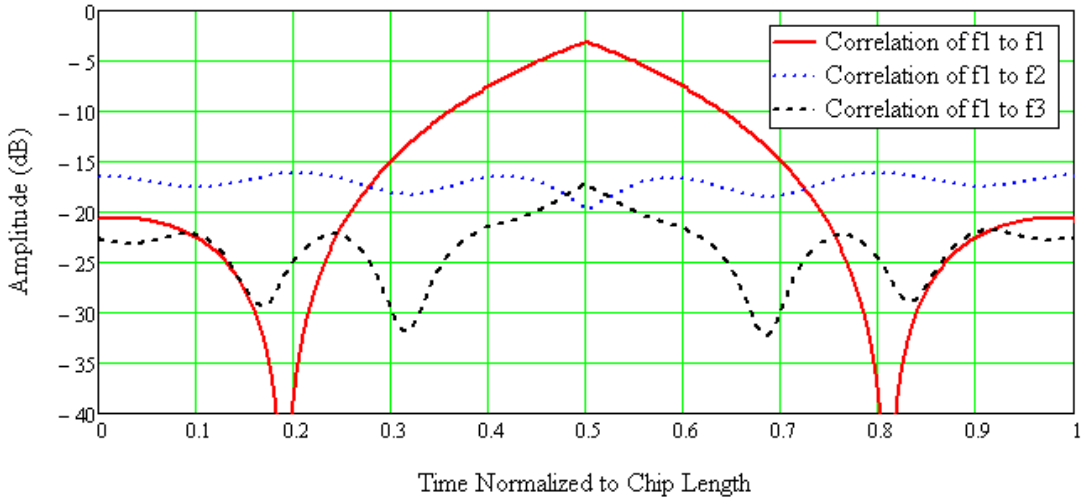

Figure 6.15: Cross-correlation of first and second adjacent bandwidth optimized P-OFC frequencies for reflector chips with 150 electrodes. The center frequency separation is $1.6/\tau_c$MHz. Amplitude of all three correlation pulses are normalized to the peak of the auto-correlation of f_1 shown in red and plotted versus time normalized to chip length.

6.4 Devices at 250 MHz

Several 8 chip P-OFC and OFC devices were built on YZ-$LiNbO_3$and experimental results and COM model simulations were compared and excellent correlation between model and experiment was observed. Fig. 6.16 and Fig. 6.17 are the P-OFC and OFC experimental and COM simulated SAW tag time responses, respectively. In Fig. 6.17 $chip_5$ and $chip_6$ are distorted due to intersymbol interference in frequency from adjacent frequency chips. However, Fig. 6.16 shows a much more robust response with little chip degradation. These tag responses are electrically mismatched and therefore show a large insertion loss; simple series inductive tuning can reduce the insertion loss significantly. Fig. 6.18 shows the experimental and COM simulated SAW ID tag response for P-OFC with 150 electrode reflector chips. The effect of the SAW transducer is minimized by time-gating the OFC reflector response and normalizing by the transducer conductance. The high frequency chip roll-off is attributed to propagation loss under the reflector grating. Fig. 6.19 shows the experimental and the COM simulated gated SAW ID tag responses for an OFC device with 50 electrode chips. When compared to the OFC device with only 50 electrodes in each chip the 150 electrode P-OFC SAW tag shows approximately 3dB less insertion loss.

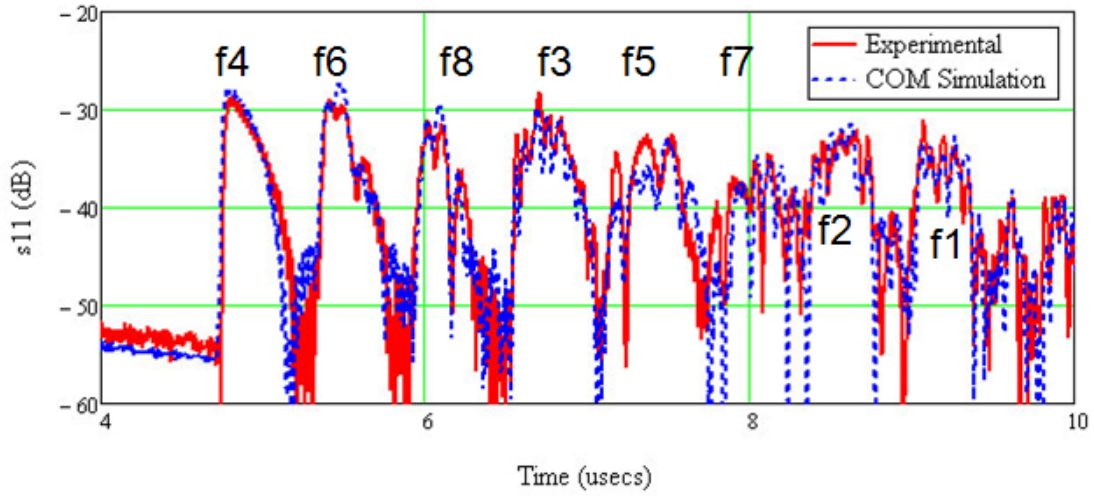

Figure 6.16: Experimental (in red) and COM simulated (blue) response of an 8-chip P-OFC SAW ID tag. Experimental and COM simulation shows good agreement and no chip degradation is observed.

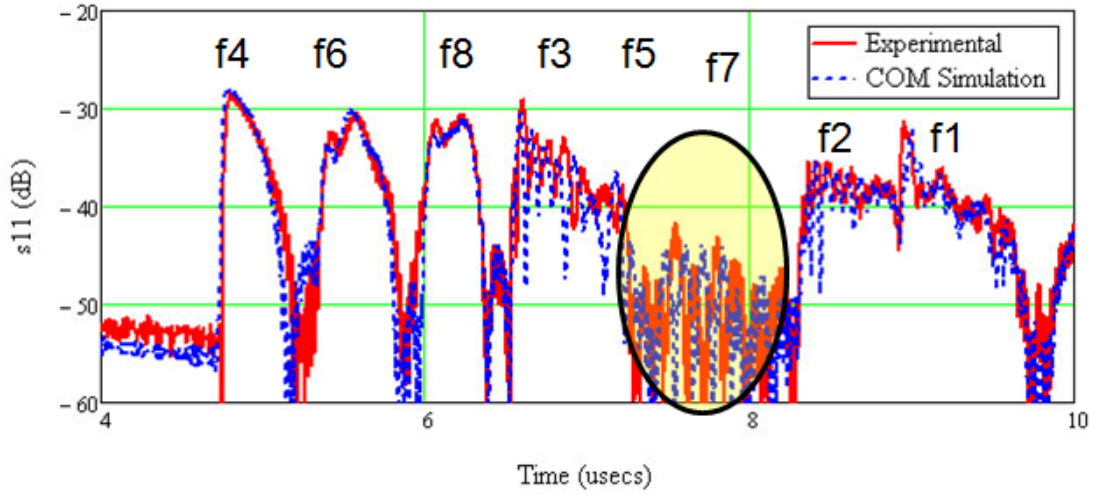

Figure 6.17: Experimental (in red) and COM simulated (blue) response of an 8-chip OFC SAW ID tag. Experimental and COM simulation shows good agreement and chip degradation is observed for chips five and seven (shown in the highlighted area).

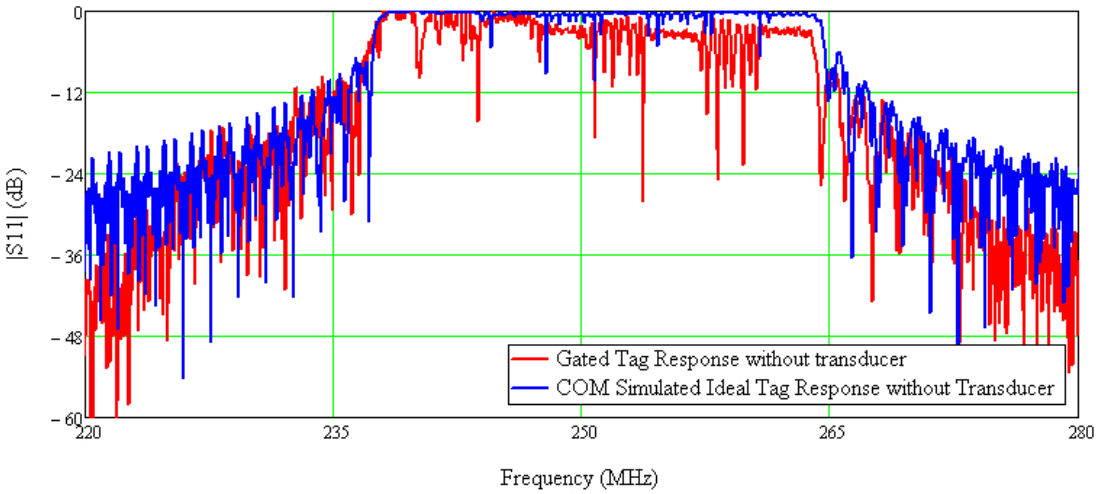

Figure 6.18: Experimental gated SAW OFC reflector response (in red) and COM simulated ideal OFC reflector response (in blue) for a 8 chip P-OFC tag with 150 electrodes in each chip.

Figure 6.19: Experimental gated SAW OFC reflector response (in red) and COM simulated ideal OFC reflector response (in blue) for a 8 chip OFC tag with 50 electrodes in each chip.

6.5 Device Results at 915 MHz

In order to make the antenna smaller it was necessary to go to higher frequencies. A center frequency of 915 MHz was chosen since it was in the region of the ISM band and the industry collaborator, Mnemonics, was able to secure an experimental UWB license for testing their transceiver system at this center frequency.

A previously designed simple dipole antenna on printed circuit board (PCB)at 915 MHz with a gain of roughly 2dB was used as the sensor antenna [63]. The dimensions of the device and antenna are 4.5in x 1.5in. A picture of an OFC device with the PCB antenna is shown in Fig. 6.20.

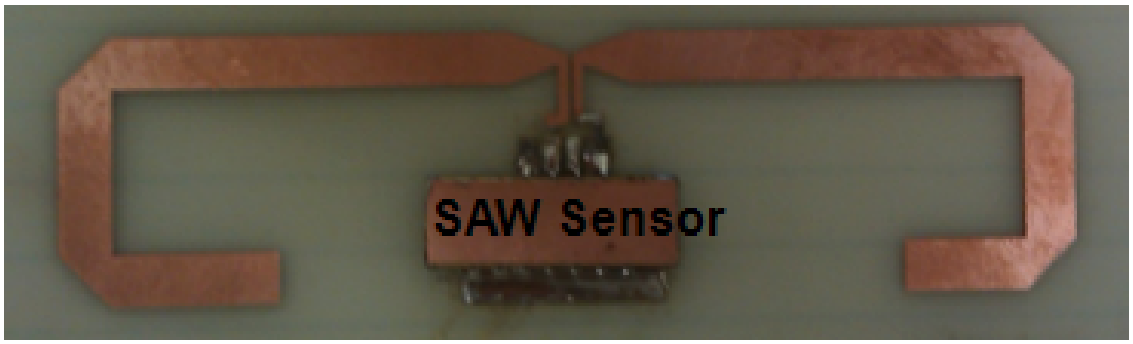

Figure 6.20: Picture of OFC device at 915 MHz mounted on PCB dipole antenna.

OFC sensors with five chips each were built with impedance optimized to minimize mismatch loss when the sensors were connected to the dipole antenna. The devices were designed so that the real part of the packaged device impedance would be close to the real part of the dipole antenna impedance. Shown in Fig. 6.21 is the impedance of the dipole antenna and the impedance of the 915 MHz OFC device. The antenna impedance is more inductive and the SAW device has a capacitive impedance; in order to avoid an external matching network and keep the amplitudes of

the chips relatively uniform an attempt was made to self match the real part of the SAW device to 50 ohms. To accomplish this, the device was split into two tracks that were electrically in parallel. Fig. 6.22 shows the layout of the device.

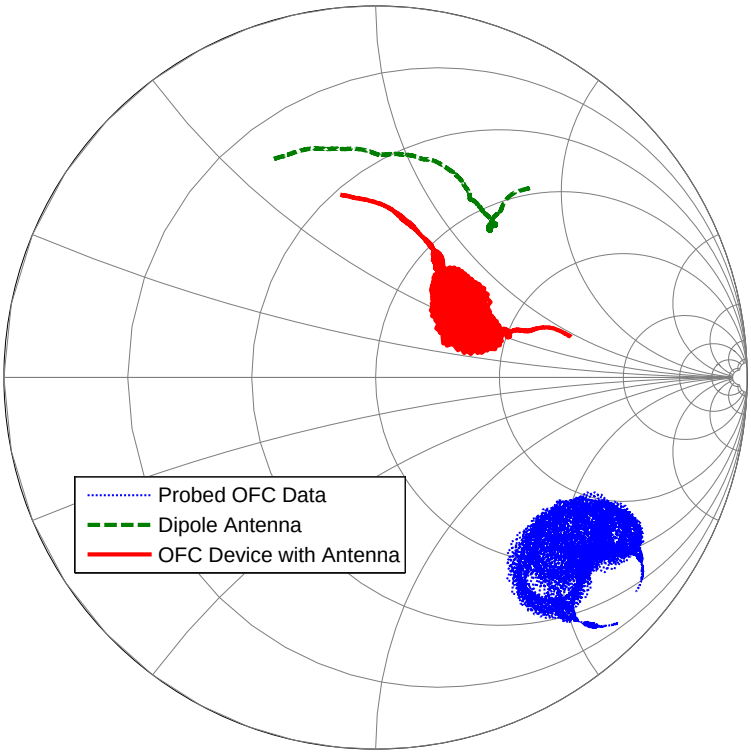

Figure 6.21: Plot of measured antenna impedance, probed OFC device impedance and impedance of packaged OFC device with dipole antenna operating at 915 MHz center frequency.

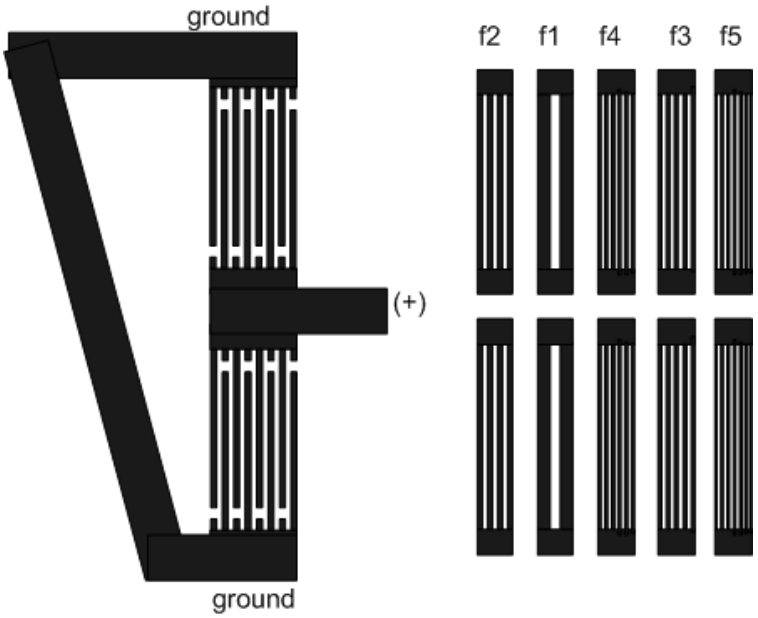

Figure 6.22: Schematic of impedance optimized OFC device at 915 MHz. All the reflectors are inline which introduces losses from the wave propagating under adjacent reflectors.

The transducer for each track was designed to be offset in frequency so that it was centered at either at f_2 or at f_4 and the beamwidths and number of transducer electrodes were chosen such that the net impedance of the two tracks would be have a real part close to 50 ohms at center frequency. The reflectors in each track were inline and were identical to each other. Each reflector chip had 50 electrodes and the entire device bandwidth was 100MHz yielding a fractional bandwidth of 11%. Fig. 6.23 shows the frequency and time domain plots of one of the OFC devices out of a set of four different codes. The device had $\lambda/4$ electrodes in the transducer, and the grating center frequencies were as follows: f_1= 878MHz, f_2= 896MHz, f_3= 915MHz, f_4= 933MHz, and f_5= 951MHz. The code sequence was f_2, f_1, f_4, f_3, and f_5. The roll-off in time domain from chip 1 to chip 5 is due to propagation losses under the grating electrodes which was originally unaccounted for in the design and is almost 6dB.

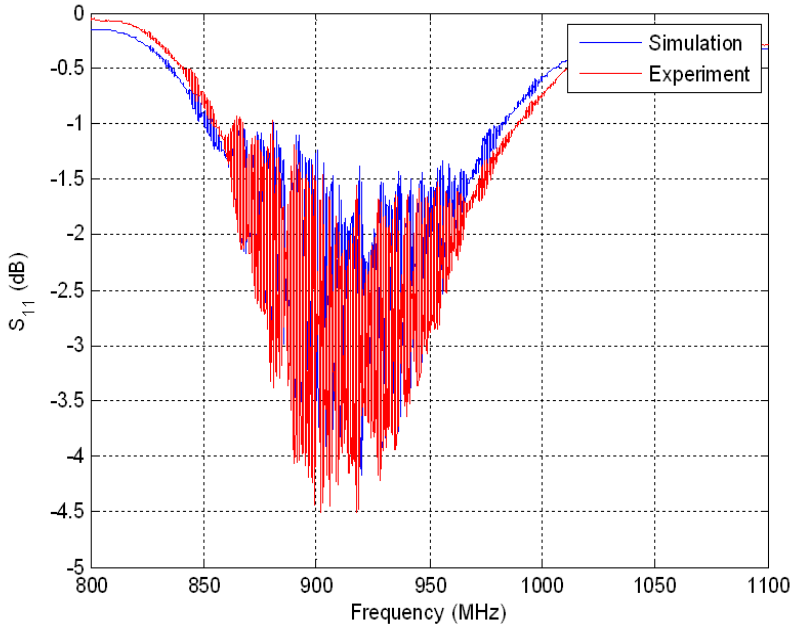

(a)

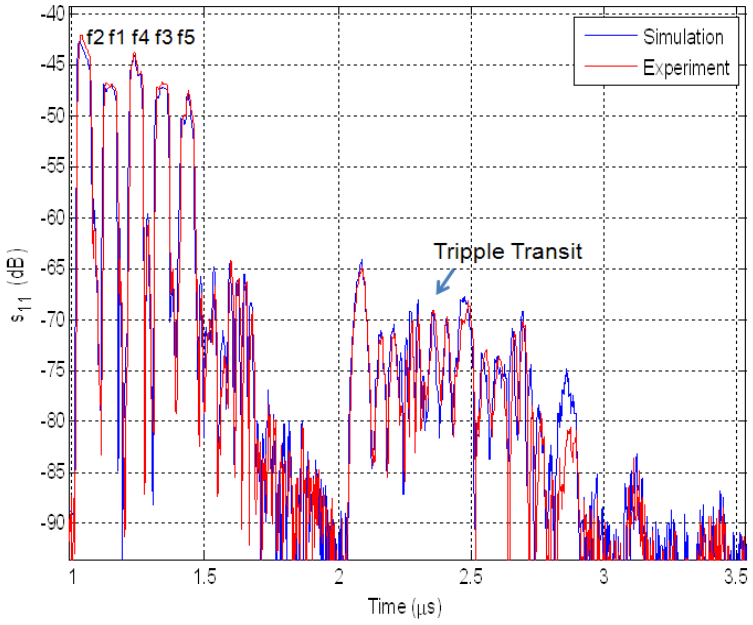

(b)

Figure 6.23: Frequency and time responses of a 5-chip OFC device. The amplitude roll-off in time domain is due to propagation losses under the gratings and is predicted well by the COM simulation which included the loss factor under the grating electrodes.

The OFC devices were interrogated using the transceiver provided by Mnemonics, Inc. The obtained raw data was then processed using a software adaptive matched filter in MATLAB®to determine the temperature of each sensor tag. Fig. 6.24 shows the acquired temperature plot of a single sensor; the solid line is the sensor temperature and the dots indicated the temperature tracked by a thermocouple attached to the back of the PCB. The sensor was cooled and heated using dry ice and a heating gun and all these measurements were first made at a distance of 7 feet. The thermal mass of the PCB and the package for the sensor resulted in a deviation of thermocouple and sensor temperature due to the thermal lag. The sensor was then moved to a distance of 12 ft, 15 ft and 21 ft respectively and continued to track well with the temperature recorded by the thermocouple. The spikes in the sensor temperature are due to signal interruptions from moving the sensor and the time it takes for the adaptive filter to be able to correlate and lock on to the sensor again.

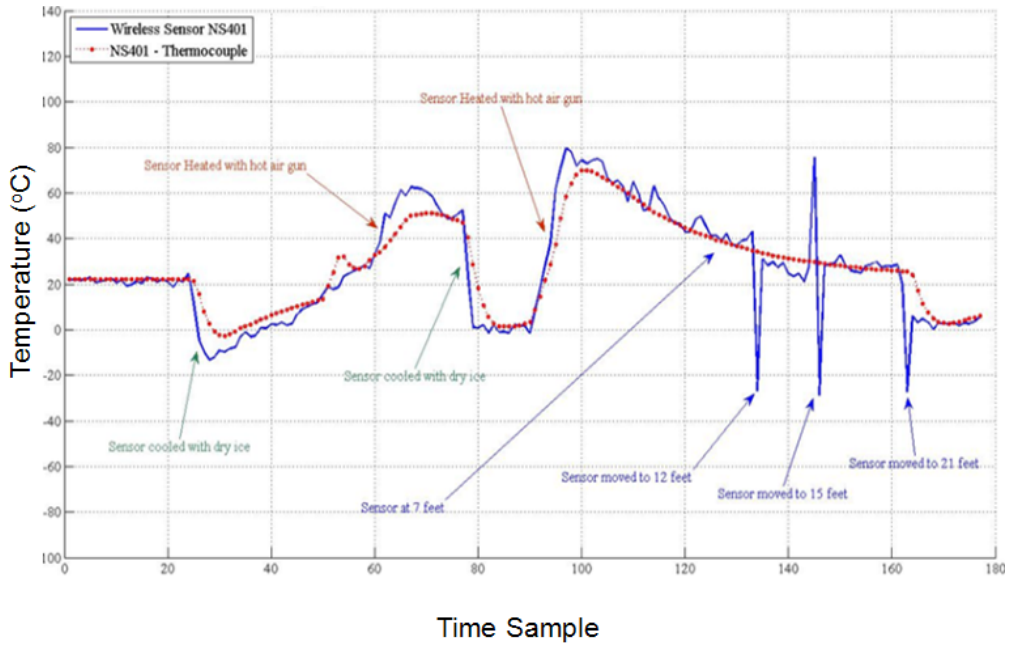

Figure 6.24: Plot of single OFC sensor being heated and cooled; solid line is extracted sensor temperature and dots indicate thermocouple temperature. The discrepancies between the thermocouple and sensor temperature are due to the thermal mass of the sensor package and PCB. Each time sample is a few seconds since the data acquisition and the adaptive filter software is in MATLAB®.

Next four OFC devices with different codes were simultaneously interrogated using the Mnemonics transceiver; time domain plots of the four devices are shown in Fig. 6.25. The codes had frequency diversity and had no time overlap to provide good cross-correlation properties.

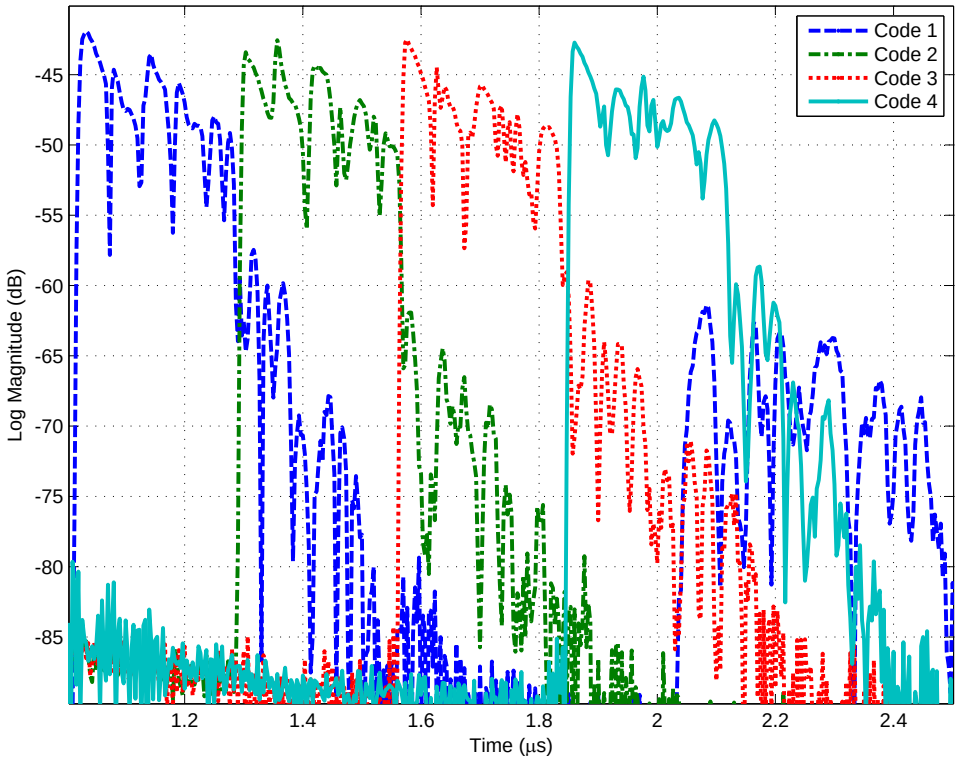

Figure 6.25: Time domain responses of the four orthogonal codes used for simultaneous interrogation. The codes had frequency diversity and had no time overlap to provide good cross-correlation properties.

If the codes are placed equidistantly from the transceiver, the signal from all four codes arrives at the transceiver simultaneously, which creates the worst case scenario, severely distorting the desired correlation. Offsetting the reflectors in the time-domain so that they are orthogonal to each other in time and frequency will never allow for the signals to completely overlap in time, thus improving the correlation peak to side-lobe ratio for the desired sensor. In Fig. 6.26(a) and Fig. 6.26(b) are the auto-correlation and matched filter correlation with the signal from a single sensor and with the sum of the signals from all the four sensors. The correlation side-lobes are worse by at least 3 dB in the case where multiple sensors are interrogated.

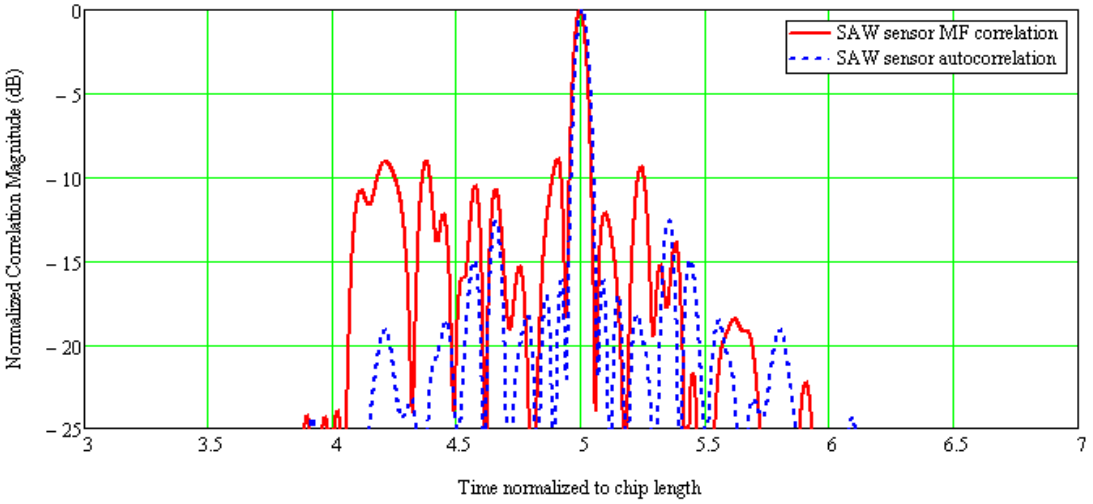

(a)

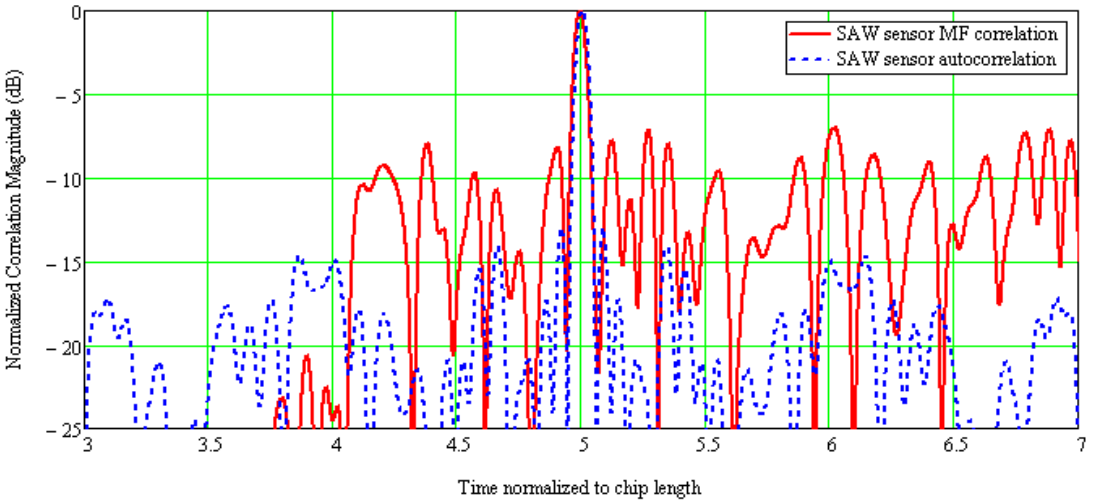

(b)

Figure 6.26: Matched filter correlation with (a)single sensor (b) four sensors in the system. Side-lobe level increases as more sensor are introduced into the environment due to self-interference of multiple sensors.

Since all the reflectors were inline, the loss from propagating under the reflector electrodes causes the chips to roll-off in the time domain. In order to reduce the effects of propagation loss under the gratings the reflectors can be arranged in tracks so that the wave does not propagate under two adjacent reflectors. An OFC device using this layout is shown in Fig. 6.27

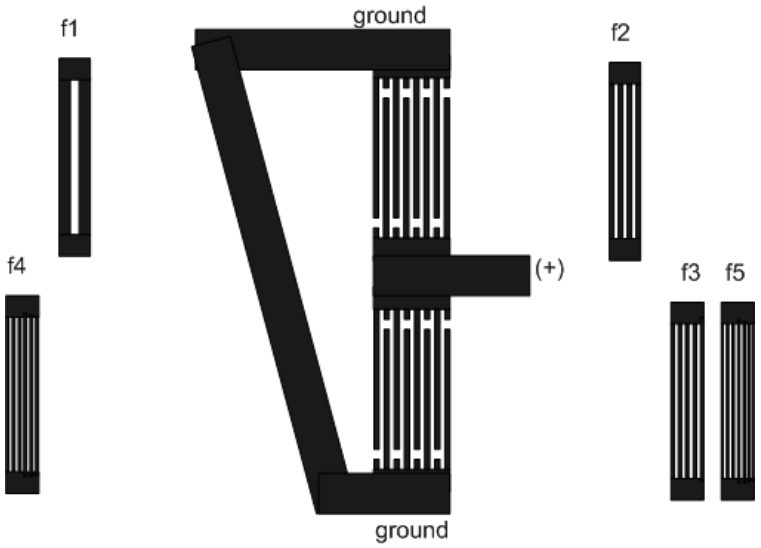

Figure 6.27: Time domain responses of the four orthogonal codes used for simultaneous interrogation. The codes had frequency diversity and had no time overlap to provide good cross-correlation properties.

Devices were built with this layout to test for improvement of device performance. Fig. 6.28 is the time domain plot of the device with the staggered layout. The chip amplitude modulation is now less than 3 dB which enhances the device correlation properties. This method significantly improves device performance in the P-OFC case where each of the reflector chips are much longer and the roll-off in the chips is substantial. Fig. 6.29 shows the time domain responses of a P-OFC device at 915 MHz that has the reflectors in an inline layout and one in which the reflectors are

staggered as shown in Fig. 6.27. The chip roll-off in the inline layout is approximately 15dB and is significantly reduced in the staggered layout.

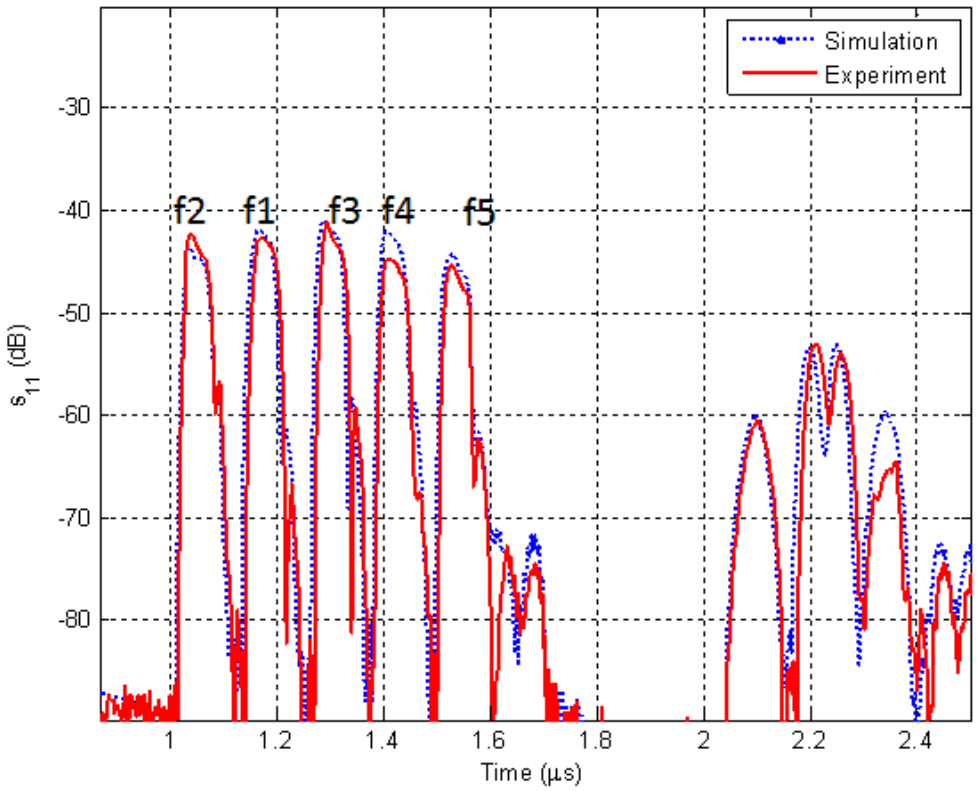

Figure 6.28: Time domain response of the OFC device with the improved staggered layout. The time domain roll-off is improved which enhances correlation properties.

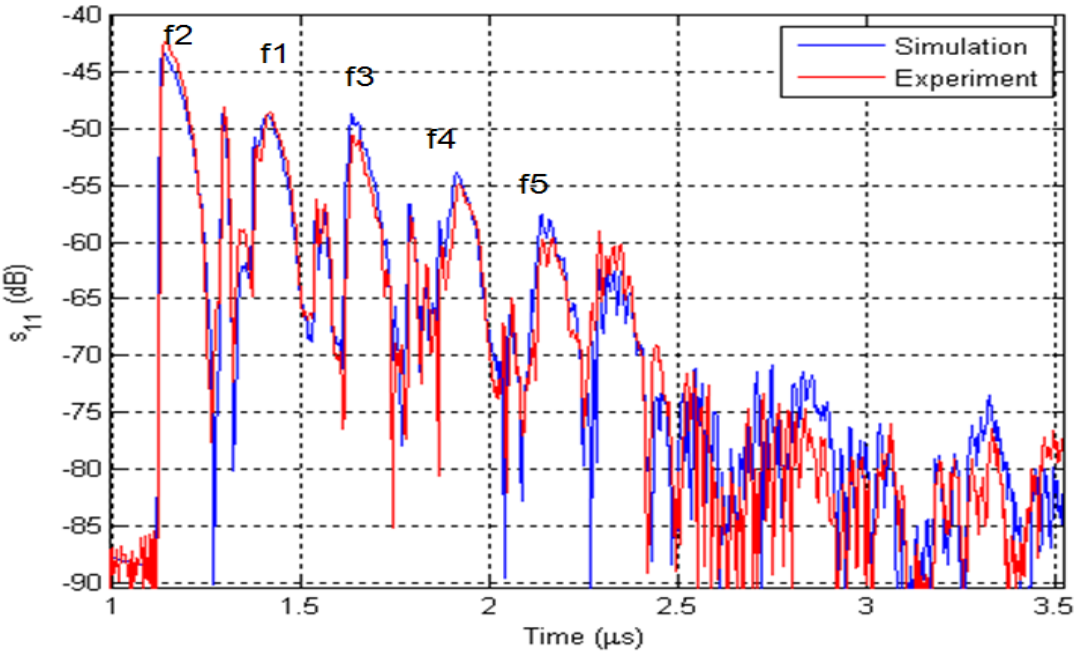

(a)

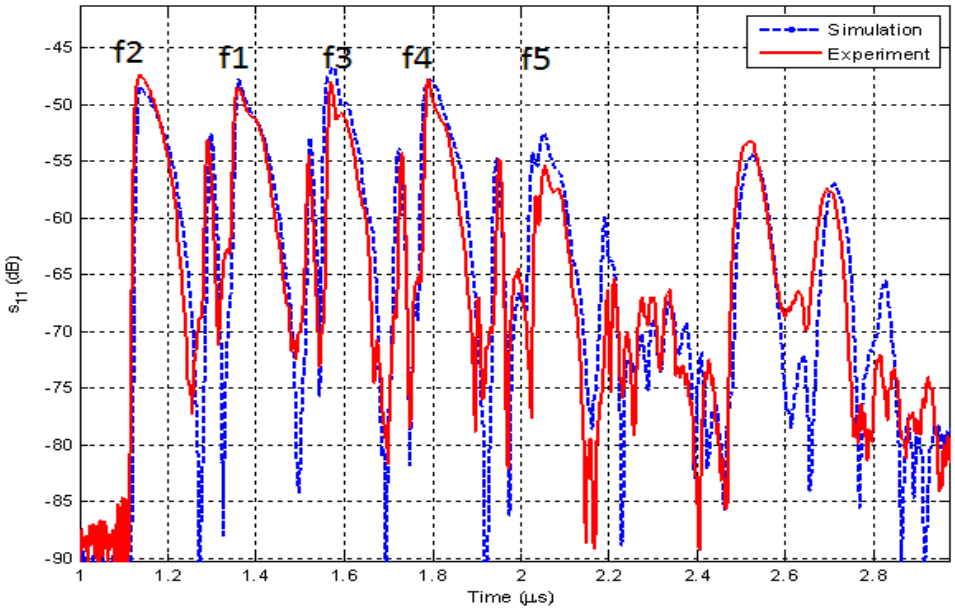

(b)

Figure 6.29: Comparison of an inline chip layout and a staggered chip layout. The roll-off in chip amplitude to due propagation losses under the reflector electrodes is significantly reduced in the staggered layout case.

The code sequence for the P-OFC device is the same as that chosen for the OFC device shown earlier so that a good one to one comparison can be provided. The reflector responses for the staggered layout of the OFC device and the P-OFC device were gated in the time domain and normalized to the transducer response in order to eliminate effects of the transducer passband, bidirectional loss and mismatch loss. The gated reflector chips for the two devices are plotted in Fig. 6.30 to show a comparison of the reflector bandwidth and the reflector losses. The P-OFC device has a bandwidth of interest from 890MHz to 940MHz, a span of 50MHz and a fractional bandwidth of 5.4% at 915MHz center frequency. The OFC device has a bandwidth of interest from 865MHz to 965MHz, a span of 100MHz and a fractional bandwidth of 11%. The P-OFC reflectors have 150 electrodes in each chip and are 3 times longer than the OFC chips which have only 50 electrodes per chip. The insertion loss of the P-OFC reflectors is about 3 dB lower than the OFC reflectors due to the longer reflector length.

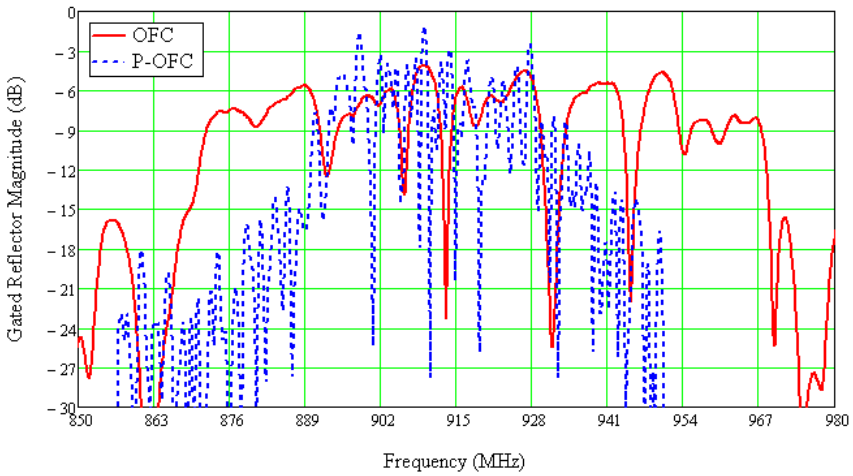

Figure 6.30: Comparison of gated reflector responses with transducer effects eliminated. P-OFC device has 5.4% fractional bandwidth and the OFC device has 11% bandwidth, the reflector loss is 3 dB lower in the P-OFC device.

Next, the devices were correlated against themselves and the compressed pulses are shown in Fig. 6.31. Fig. 6.31 shows the compressed pulses obtained from the auto-correlation of a five chip OFC device with 50 electrodes per chip and a five chip P-OFC device with 150 electrodes per chip; a COM simulated five chip OFC device auto-correlation with 150 electrodes per chip is also shown for comparison of the compressed pulse. The 150 electrode per chip OFC device will have a high energy overlap with adjacent frequency chips producing pulse distortion as shown earlier and therefore is not used. The compressed pulse width is related to the time-bandwidth product of the device. The OFC device with 150 electrodes has the widest compressed pulse and the P-OFC code has a narrower compressed pulse, which allows for greater sensitivity. The use of longer reflector chips provides lower insertion loss thus allowing for larger transmission distance in a wireless environment.

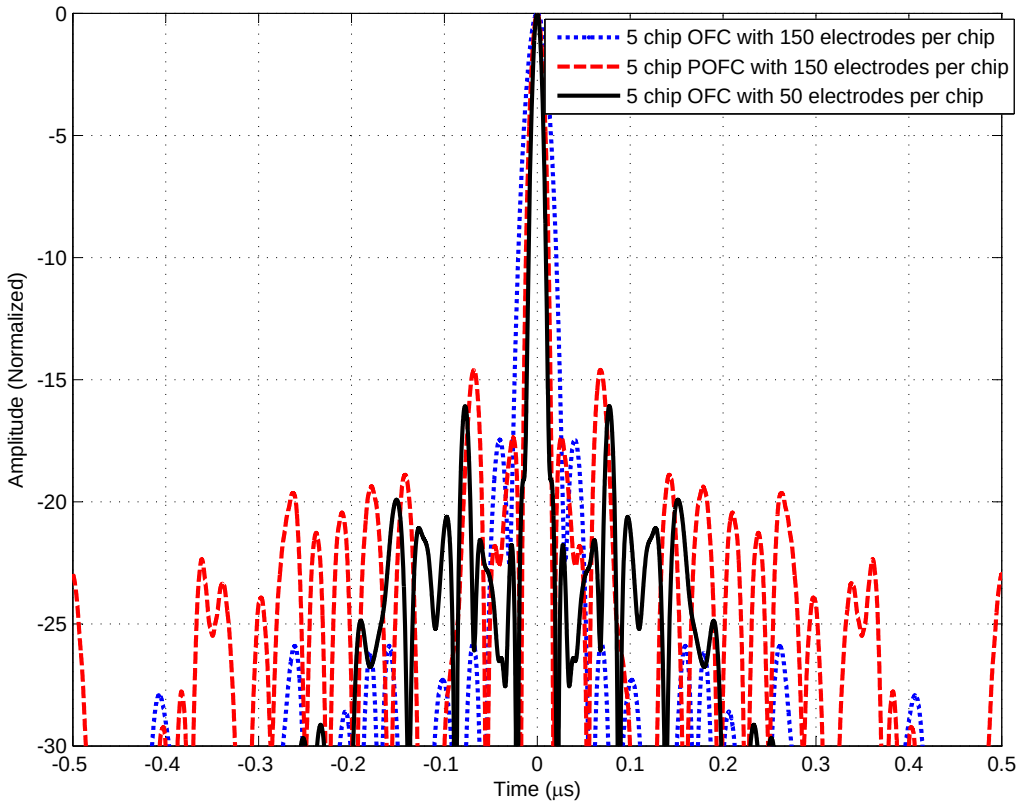

Figure 6.31: Compressed pulse obtained from the auto-correlation of the responses of an (150 electrodes per chip) five chip OFC device and P-OFC device and a (50 electrodes per chip) five chip OFC device . The P-OFC auto-correlation has a narrower pulse.

The P-OFC device was then interrogated using the Mnemonics' transceiver system to sense temperature wirelessly. The device used for the wireless interrogation had a fractional bandwidth of 5.4% as compared to the 11% fractional bandwidth for an OFC device with five chips. The reflector loss was 3dB, the overall device insertion loss was 18 to 20dB which is due to the transducer bidirectional loss of 6dB, mismatch loss between antenna and device and reflector losses. The P-OFC device was first interrogated by itself at a distance of 7ft and the results are shown in Fig. 6.32. The device was heated using a heat gun and then cooled using a can of gas duster held upside down. The temperature from the sensor tracked well with the thermocouple when heated, however when cooled there was some lag in the temperature possibly due to changes in the antenna radiation introduced due to the liquid from the gas duster on the antenna surface. As the liquid residue from the gas duster evaporated the sensor temperature correlated well with the thermocouple data. The results are similar to the wireless measurement for the OFC device shown in Fig. 6.24

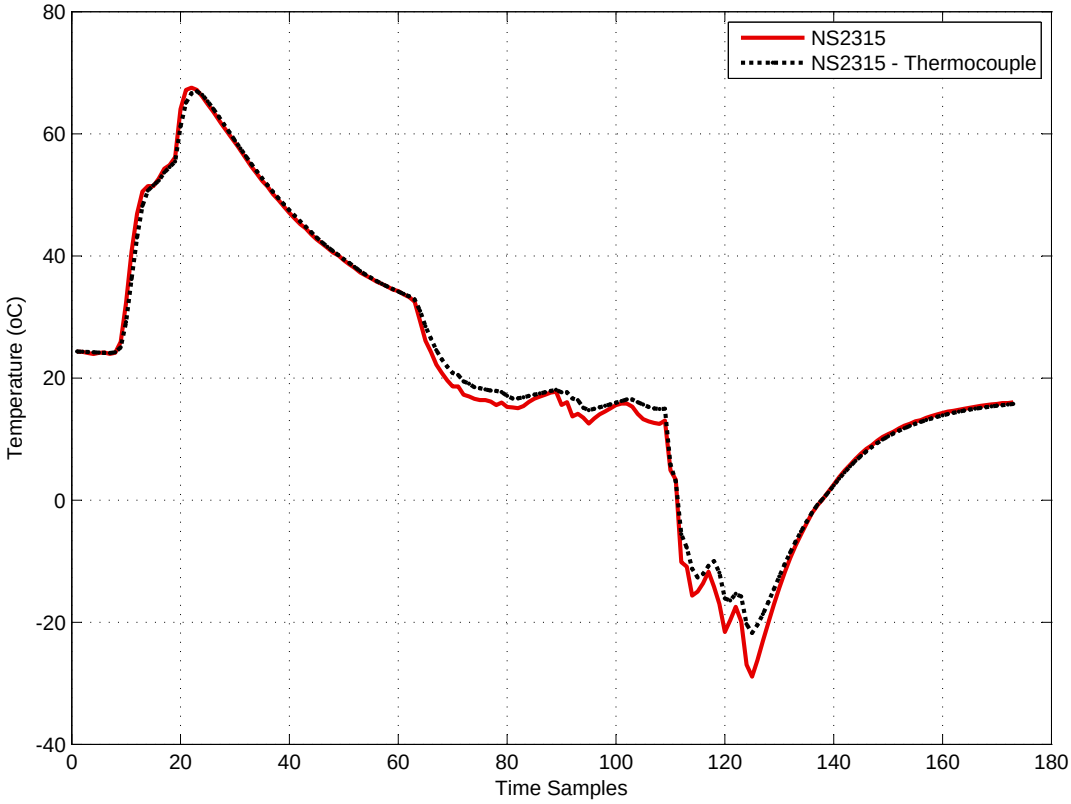

Figure 6.32: Wireless interrogation of the new P-OFC device at 915MHz using transceiver from Mnemonics. The device was heated using a heat gun and then cooled using a can of gas duster held upside down. The P-OFC device had a 5.4% fractional bandwidth.

6.6 Harmonic Operation

Harmonic device operation was investigated to test the feasibility of building devices at higher frequencies with lower line-width resolution. Delay line devices with transducers that had $\lambda/6$ and $\lambda/8$ wavelength electrodes and reflectors that had $\lambda/4$ wavelength periodicity were fabricated. Transducers with $\lambda/6$ wavelength electrodes operate at first and second harmonic and transducers with $\lambda/8$ wavelength electrodes operate at first and third harmonic.

The S_{21} frequency and time responses of the of three delay lines with reflectors are plotted in Fig. 6.33. The reflector response appears as a ripple in the passband of the delay line frequency response. Bulk radiation occurs close to the second harmonic passband, which cause a loss of energy from the surface wave at the frequency of interest. The reflectors operated at both the second and third harmonics, however for the given metal thickness and electrode width the normalized metal thickness (h/λ) increases with increasing harmonic operation. Thus the first harmonic reflector has the lowest normalized metal thickness and the third harmonic has the highest. The second harmonic reflector in this case where the metal thickness was 2000A^o had the highest reflectivity, and reflectivity for first and second harmonic was previously characterized; however, reflectivity behavior at the third harmonic had not been investigated. Therefore, third harmonic transducer operation with second harmonic reflectors was chosen for the harmonic OFC and P-OFC devices. This allowed use of the COM model with the second harmonic reflectivity model presented earlier, to predict device behavior.

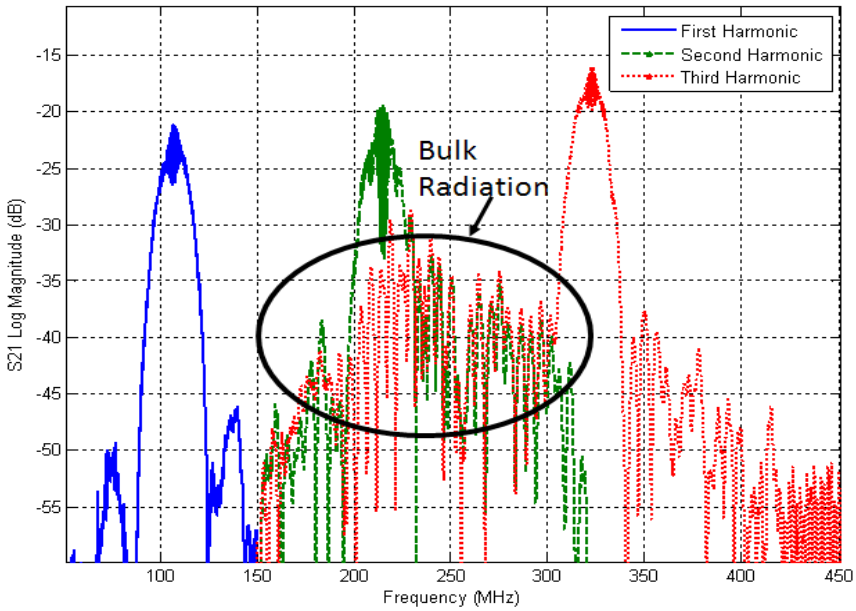

(a)

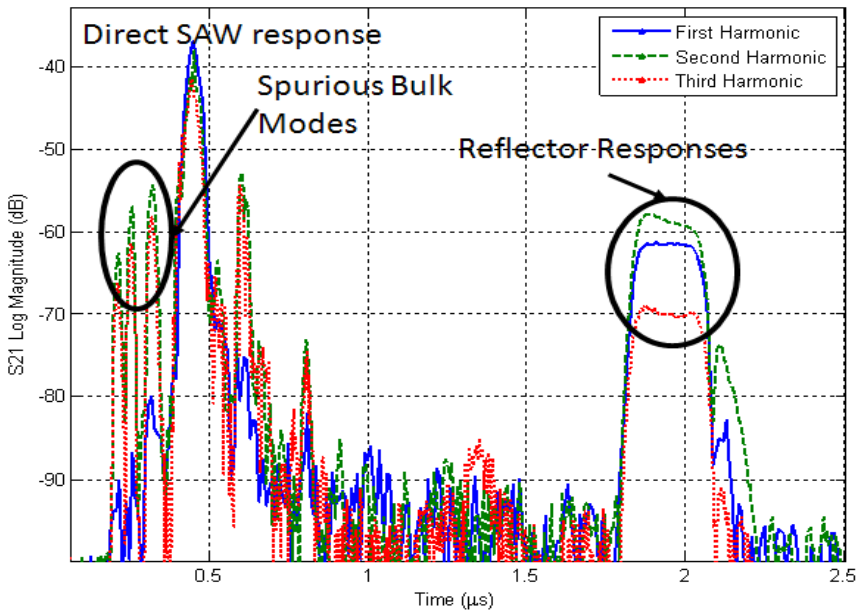

(b)

Figure 6.33: The S_{21} (a)frequency and (b)time response of delay line devices with reflectors. The reflector response appears as a ripple in the passband of the delay-line frequency response. Bulk radiation occurs close to the region of the second harmonic transducer passband. The reflectors operate at all harmonics with the greatest reflectivity for the given film thickness occurring at second harmonic.

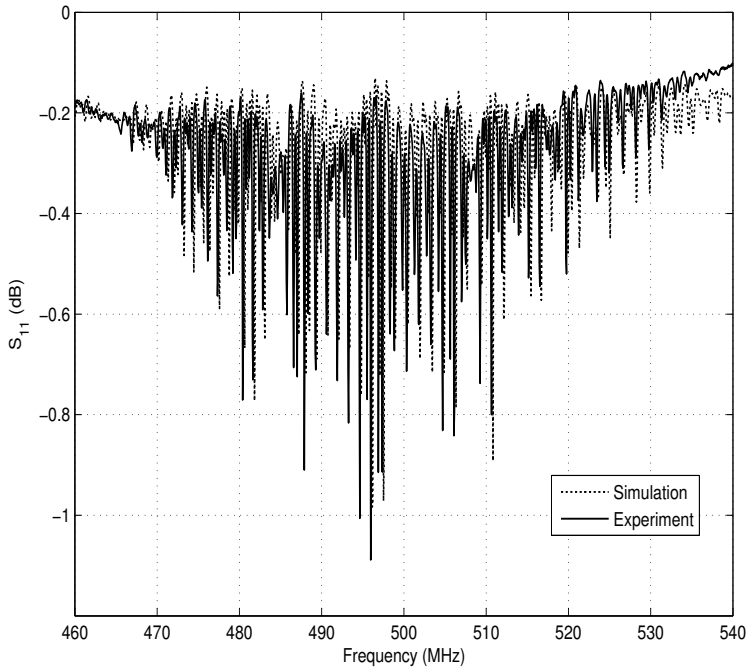

(a)

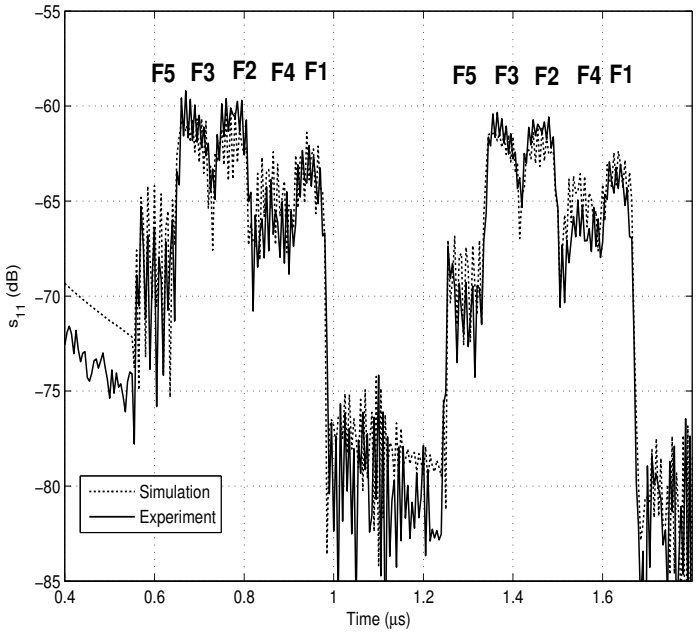

(b)

Figure 6.34: Experimental (solid red curve) and COM modeled (dashed blue curve) S_{11} (a)frequency and (b)time responses of an OFC reflector device at second harmonic operation. The device has 5 reflector chips each on either of the transducer, hence two sets of reflections are observed in the time response.

Shown in Fig. 6.34 are the S_{11} frequency and time responses of an OFC tag operating at second harmonic at a center frequency of 500 MHz. The experimental and COM modeled results are shown and exhibit good correlation. There are slight discrepancies between COM predicted and measured performance attributed to small imperfections in fabrication with variation in $\frac{a}{p}$ versus frequency and scaling. In the second harmonic device a $\frac{1}{8}$ wavelength electrode transducer operating at its third harmonic was used with reflectors operating at their second harmonic. The transducer was bound by five orthogonal reflector chips on either side, this produces two sets of reflections as shown in the time domain response. The device had shorted aluminum reflectors with an average of 20 electrodes per chip, a normalized metal thickness of 1.4% and a metallization ratio of 0.5. The frequency domain order of the reflector chips as they appear spatially are indicated in time domain response by labels F1, F2...etc; F1=476 MHz being the lowest frequency and F5=524 MHz being the highest with a step of 12 MHz between frequencies and a net device frequency bandwidth is 48 MHz. The second harmonic device employed reflector chips with fewer electrodes as compared to the 250MHz fundamental device, and therefore has a wider frequency bandwidth. Fig.6.34(b) show that the time delays of the experimental and COM simulated responses correlate well for the different frequency reflector chips, indicating the velocity used is accurate. The modulation of chip reflector magnitudes is due to transducer bandwidth narrowing and is predicted well in the simulation. The experimental and theoretical correlation of the time chip amplitudes of the devices indicate that the reflectivity is being modeled correctly. These results validate the proposed changes to the terms in the transmission line model and verify

that the coefficients obtained from the least squares fit to the data can be used to accurately model reflectivity and velocity at both fundamental and second harmonic operation.

A P-OFC harmonic device with a $\frac{1}{8}$ wavelength electrode transducer operating at its third harmonic was used with reflectors operating at their second harmonic. The device had a center frequency of 1.6 GHz to test feasibility at frequencies higher than 1GHz and determine the effect of losses under the gratings at higher frequencies. Since the reflectors at second harmonic have strong reflectivity, shorter chips with an average of 75 electrodes per chip were used. However, inspite of the shorter chips the losses under the electrodes was high as seen in the time domain chip amplitude roll-off in Fig. 6.35(a). The chips were laid out in the staggered format shown in Fig. 6.27 to minimize the losses, and yet had a roll-off of 10 dB from the first chip to the last was observed. The gated frequency response of the reflectors normalized to the transducer response is shown if Fig. 6.35(b). The first frequency chip, f_1 has a loss of 10dB from free space propagation. The last chip f_5 has a loss of 20 dB from propagation losses under the gratings. The propagation losses at frequencies beyond 1 GHz introduce too much loss in the gratings therefore making it problematic in reducing the over-all insertion loss of the device and hence making them useful as passive sensors for only short range applications.

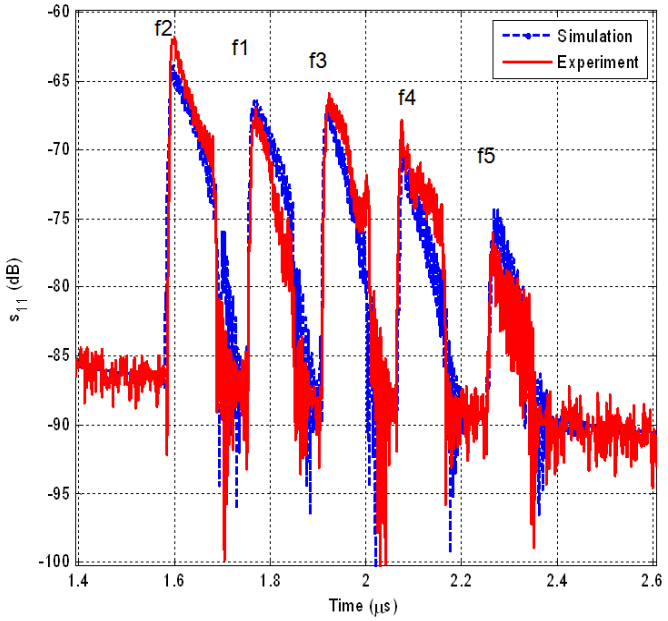

(a)

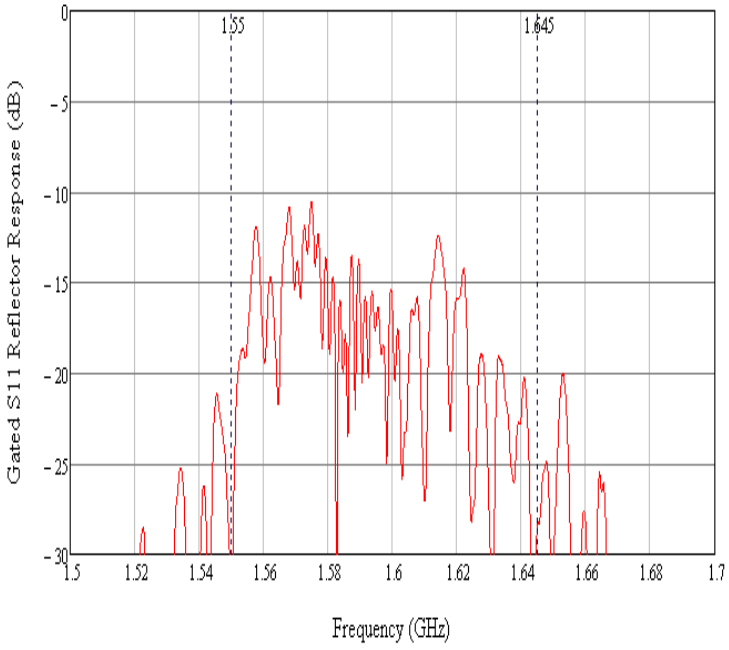

(b)

Figure 6.35: (a)Time-domain response of a five chip P-OFC device at 1.6 GHz using harmonic operation. The roll-off from chip one to 5 is approximately 10 dB. (b) The gated reflector response of the P-OFC device; effects of transducer bidirectional loss and mismatch loss are eliminated, and propagation loss effects are isolated. The first chip, f_1, has a loss of 10 dB, due to free space propagation loss at 1.6GHz, chip f_5 has a loss of 20dB.

6.7 Devices on 128^o YX Lithium Niobate

128^o YX $LiNbO_3$ has higher coupling of 5.4% and a lower TCD of 75ppm/^{o}C as compared to YZ $LiNbO_3$ which has a coupling of 4.6% and a TCD of 94 ppm/^{o}C. The higher coupling and lower TCD makes it an attractive material choice for other sensor applications such as strain, pressure etc. Preliminary investigation of OFC devices on 128^o YX $LiNbO_3$ was performed. Using a mask for OFC devices on YZ $LiNbO_3$ OFC devices were fabricated on 128^o YX $LiNbO_3$ and the experimental results of a device designed for 915MHz on YZ $LiNbO_3$ are shown in Fig. 6.36. The SAW velocity on 128^o YX $LiNbO_3$ is 3979m/s which is higher than that on YZ $LiNbO_3$ (3488m/s), therefore the frequency response occurs at higher frequency of 1.05GHz. In order to have the reflectors centered within the transducer bandwidth the reflectors would have to be redesigned to account for the velocity shift under the reflector electrodes on 128^o YX $LiNbO_3$.

For comparison the S_{11} frequency response device on YZ $LiNbO_3$ and 128^o YX $LiNbO_3$ are shown in Fig. 6.36. The device on 128^o YX $LiNbO_3$ has better coupling as seen in the S_{11} response, however the reflectors are not centered within the transducer passband and a new design would be needed to correct for this shift. In order to compare the fractional bandwidth and the losses in the reflectors the gated reflector responses of the devices with transducer effects eliminated are plotted in Fig. 6.37. The frequency scale for the device on 128^o YX $LiNbO_3$ was scaled down to be centered at 915 MHz for comparison. The fractional bandwidth of the device on YZ $LiNbO_3$ and 128^o YX $LiNbO_3$ remains the same at 11%, however the reflector loss is approximately 3 dB lower on 128^o YX $LiNbO_3$. 900A^o of aluminum was used on YZ $LiNbO_3$ to obtain optimum reflectivity,

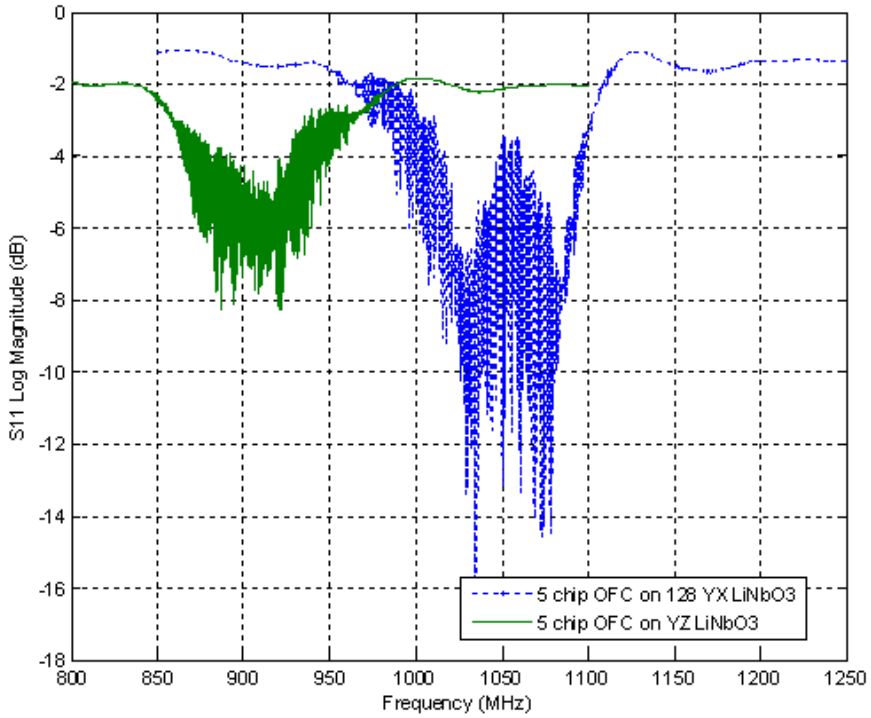

Figure 6.36: Comparison of the S11 frequency responses of same OFC device on on YZ $LiNbO_3$ and 128^o YX $LiNbO_3$. The device on 128^o YX $LiNbO_3$ has higher coupling, velocity and reflectivity.

however, in order to get higher reflectivity on 128^o YX $LiNbO_3$ a much thicker aluminum film of 2200A^o was used.

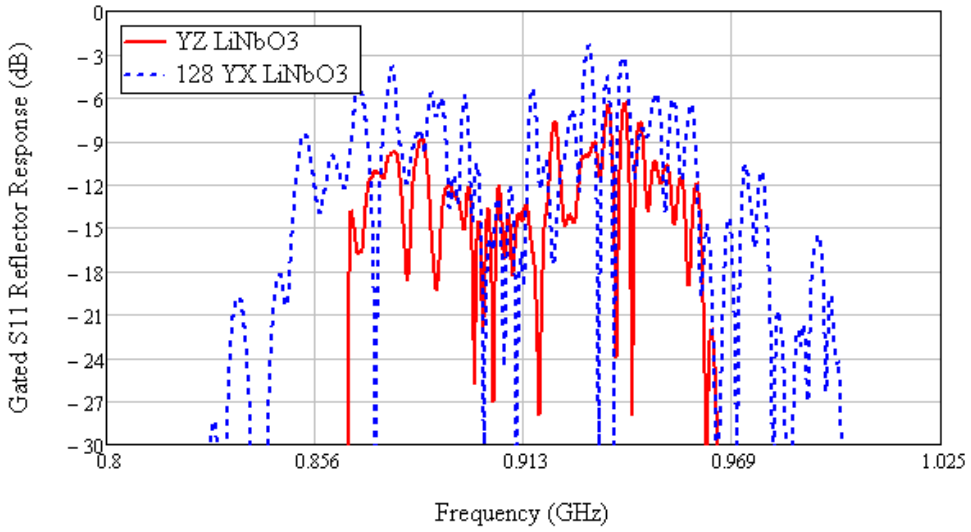

Figure 6.37: The gated reflector responses of the OFC devices on YZ $LiNbO_3$ and 128^o YX $LiNbO_3$ with transducer effects eliminated. The frequency scale for the device on 128^o YX $LiNbO_3$ was scaled down to be centered at 915 MHz for comparison.

6.8 Summary of Results

The concept of P-OFC to reduce device insertion loss and fractional bandwidth was presented. The P-OFC definition for orthogonality can be used in the region $1.2 < Ng \cdot r < 2.5$. P-OFC devices with $Ng \cdot r = 2.1$ i.e. devices with 150 electrodes in each chip, were built for this dissertation. The ideal frequency separation between chips was determined based on individual chip auto-correlation and cross-correlation properties to adjacent frequency chips. The frequency spacing of $1.6/\tau_c$ was found to yield good correlation properties while simultaneously reducing the device bandwidth to

5.4% which is approximately half that of the OFC device with 50 electrodes per chip. The devices were modeled and designed using the new reflectivity model incorporated into the COM model and the correlation between simulation and measurement justified the validity of the model and extracted reflectivity on YZ $LiNbO_3$.

Several OFC and P-OFC devices with optimized impedances were designed on YZ $LiNbO_3$ first at 250 MHz to test proof of concept and model validity and then at 915 MHz for use in the transceiver system by Mnemonics. The 915 MHz devices were mounted on a PCB antenna and the individual OFC and P-OFC sensors were tested with the transceiver and temperature could be extracted up to a distance of 60 m. The lower insertion loss of P-OFC devices allows for longer range, the device loss is improved by 3 dB which increases the distance by 16% according to the radar equation. The fractional bandwidth was reduced to 5.4% for the P-OFC device as compared to 11% for the OFC device with 5 chips. This will allow for use of more chips in the same given bandwidth of 11% and therefore allow for more code diversity in future devices. Shrinking of the fractional bandwidth also allows for possible use in the 2.4 GHz ISM band which has a fractional bandwidth of 4%. However, the device losses under long reflector structures at high frequency prove to be somewhat problematic making the device useful only in short range applications.

Devices at second harmonic operation were fabricated on YZ $LiNbO_3$ and proved to be feasible. Devices were fabricated at 500 MHz and 1.6 GHZ for second harmonic operation and the results were shown; at 1.6 GHz the reflector losses increased significantly and effects of propagation loss under the electrodes and possible bulk scattering are close to 5dB per chip. Finally, the first OFC devices on 128^o YX $LiNbO_3$ at 1.05 GHz were built and the devices had lower loss and

more reflectivity. The coupling to bulk modes on 128^o YX $LiNbO_3$ are known to be lower than YZ $LiNbO_3$ making it a more suitable substrate for harmonic device operation in future work [20, 64].

CHAPTER 7
DISCUSSION AND CONCLUSION

A modification to the transmission line model for a SAW reflector on YZ $LiNbO_3$ has been proposed and implemented in this dissertation. To support the proposed modifications many delay line devices with both open and short circuit aluminum gratings and variations in metallization ratios and normalized metal thicknesses were fabricated on YZ $LiNbO_3$. The gratings had metallization ratios ranging from 0.2 to 0.8 and normalized metal thickness ranging from 0.4% to 4% which provided a large range of data to characterize the reflectivity and velocity. The grating reflectivity and velocity for these devices were extracted at both first and second harmonic operation.

Modifications to the piezoelectric shorting terms and a dependence on normalized metal thickness corresponding to the form of the terms derived in perturbation theory [1, 44, 65] were proposed in order to better fit the data. A least squares fit was then performed on the data using the proposed modifications to the transmission line model. The proposed modified model fits the experimental data well and the coefficients obtained from the least squares fit were used to model grating reflectivity and velocity in the COM model and simulate frequency coded reflector devices. The experimental data of the OFC reflector devices correlate well to the COM simulation at fundamental and second harmonic operation and thus validates the proposed modifications to the transmission line model. An analysis of loss was done on a select few devices to investigate the

effect of extraction and provide a good estimation of error in the extracted parameters. At low frequencies where the reflectivity data was extracted, the loss mechanisms are relatively low and the error is minimal. However, as device operation approaches frequencies of 1 GHz and higher, the propagation loss parameters grow proportional to the frequency squared and are therefore much higher.

The concept of P-OFC was introduced to reduce device insertion loss and fractional bandwidth. The P-OFC chips were defined and devices designed and built. Optimized OFC and P-OFC devices were built at 250 MHz and 915 MHz on YZ $LiNbO_3$ and the results compared to the new improved reflectivity model implemented in the COM simulations. The extracted coefficients model reflectivity well and a varied spread of metallization ratios and metal thicknesses can now be modeled with accurate results.

The P-OFC device has an impulse response that is three times longer than the typical OFC device, however it had approximately 3 dB lower insertion loss and a fractional bandwidth that was 5.4% for the optimized device as compared to 11% for OFC device with 5 chips. The reduced fractional bandwidth allows for the ability to include more chips in the same bandwidth which can be used for more code diversity in future designs. Multiple device layouts of devices with reflectors in two tracks were fabricated to find the optimal layout of reflector structures for minimal propagation loss under reflectors and to simultaneously optimize the transducer impedance.

The inclusion of the extracted second harmonic reflectivity coefficients in the COM model allows for design and simulation of harmonic devices. Feasibility of second harmonic devices on YZ $LiNbO_3$ has been shown with devices operating at 500 MHz and 1.6 GHz. Propagation losses

at higher frequencies proved to be quite high in the 1.6 GHz device and therefore higher frequency devices were not pursued further in this dissertation. The optimized POFC and OFC devices on YZ $LiNbO_3$ at 915 MHz were used with the Mnemonics' transceiver system to sense temperature and have been shown to work up to a range of 60+ meters. The results show that the sensors work extremely well in the system and the correlation to the thermocouple temperature is quite good.

Devices were fabricated on 128^o YX $LiNbO_3$ to test feasibility for future work. 128^o YX $LiNbO_3$ has higher coupling and slightly lower TCD than YZ $LiNbO_3$ and therefore is also a good substrate choice for a temperature sensor. Moreover, it has lower coupling to bulk modes, thereby reducing losses due to bulk scattering at harmonic operation and may be a better choice for harmonic operation devices.

An extraction of loss parameters under the reflector electrodes over varying frequency needs to be investigated to provide a more rigorous prediction of the propagation losses in the reflectors as the frequency increases. It would also be useful to incorporate a reflectivity model for third and fourth harmonic reflectors to possibly use these at 2.4 GHz. The devices are currently being designed using a bi-directional transducer which introduces a 6 dB bi-directional loss and when the device is electrically matched the triple transit is high which increases the likelihood of code-collisions. Future work is needed to improve the device insertion loss and triple transit suppression by employing a unidirectional transducer embodiment. To use the sensors for high temperature applications above 200^oC, investigation of OFC and P-OFC devices on other materials such as Langasite and Langatate are needed.

The feasibilty of using P-OFC devices has been shown, and temperature using a single P-OFC was extracted. P-OFC devices with up to 4 codes similar to those used for OFC were simulated in a system to test for multi-sensor operation. Using 4 codes that are spaced in time so that there is minimal intersymbol interference between the chips allows the detection of individual sensors. However, using this technique beyond four codes may not be feasible since the die size increases and the propagation losses on the substrate increase. An investigation into the losses under reflector electrodes at high frequencies is needed to investigate the constraints on device length. A study on possible coding techniques and combining OFC and P-OFC chips to produce pulse position and pulse width modulation coding techniques is warranted for future work in order to increase code diversity. An optimization of the P-OFC matched filter being used could aide in improving tag detection in a multi-sensor environment. The feasibilty of using P-OFC device in the ISM band at 2.4 GHz with 4% fractional bandwidth needs to be investigated. In order to achieve this, harmonic devices on YX 128^0 $LiNbO_3$ should be investigated since bulk wave radiation is expected to be reduced, thus lowering loss and reducing chip degradation.

LIST OF REFERENCES

[1] S. Datta and B. Hunsinger, "A theoretical analysis of stored energy in surface wave gratings," in *Ultrasonics Symposium, 1979*, 1979, pp. 673–677.

[2] S. Harma, C.-U. Kim, S. Balashov, and V. Plessky, "Narrow electrodes on YZ-$LiNbO_3$ as an alternative to etched grooves for dispersive delay lines," *IEEE Transactions on Ultrasonics, Ferroelectrics and Frequency Control*, vol. 55, no. 2, pp. 494 –498, 2008.

[3] D. Puccio, "Design, analysis, and implementation of orthogonal frequency coding in saw devices used for spread spectrum tags and sensors," Ph.D. dissertation, School of Electrical Engineering and Computer Science, University of Central Florida, Orlando, FL., 2006.

[4] F. Seifert, W.-E. Bulst, and C. Ruppel, "Mechanical sensors based on surface acoustic waves," *Sensors and Actuators A: Physical*, vol. 44, no. 3, pp. 231 – 239, 1994. [Online]. Available: http://www.sciencedirect.com/science/article/B6THG-44B7YMK-1Y/2/d6bc0a16fcd1d3c33d1284c8b2ed8406

[5] A. Pohl, G. Ostermayer, L. Reindl, and F. Seifert, "Monitoring the tire pressure at cars using passive saw sensors," in *Ultrasonics Symposium, 1997. Proceedings., 1997 IEEE*, vol. 1, Oct. 1997, pp. 471 –474 vol.1.

[6] E. Benes, M. Groschl, F. Seifert, and A. Pohl, "Comparison between baw and saw sensor principles," *Ultrasonics, Ferroelectrics and Frequency Control, IEEE Transactions on*, vol. 45, no. 5, pp. 1314 –1330, Sep. 1998.

[7] G. Ostermayer, A. Pohl, C. Hausleitner, L. Reindl, and F. Seifert, "CDMA for wireless saw sensor applications," in *Spread Spectrum Techniques and Applications Proceedings, 1996., IEEE 4th International Symposium on*, vol. 2, sep 1996, pp. 795 –799 vol.2.

[8] A. Pohl, G. Ostermayer, L. Reindl, and F. Seifert, "Spread spectrum techniques for wirelessly interrogable passive saw sensors," in *Spread Spectrum Techniques and Applications Proceedings, 1996., IEEE 4th International Symposium on*, vol. 2, sep 1996, pp. 730 –734 vol.2.

[9] C. Hartmann, "A global saw id tag with large data capacity," in *Ultrasonics Symposium, 2002. Proceedings. 2002 IEEE*, vol. 1, oct. 2002, pp. 65 – 69 vol.1.

[10] J. Kuypers, S. Tanaka, M. Esashi, D. Eisele, and L. Reindl, "2.45 ghz passive wireless temperature monitoring system featuring parallel sensor interrogation and resolution evaluation," in *Sensors, 2006. 5th IEEE Conference on*, 2006, pp. 773 –776.

[11] J. Kuypers, L. Reindl, S. Tanaka, and M. Esashi, "Maximum accuracy evaluation scheme for wireless saw delay-line sensors," *Ultrasonics, Ferroelectrics and Frequency Control, IEEE Transactions on*, vol. 55, no. 7, pp. 1640 –1652, 2008.

[12] D. Puccio, D. Malocha, and N. Saldanha, "Implementation of orthogonal frequency coded saw devices using apodized reflectors," in *Frequency Control Symposium and Exposition, 2005. Proceedings of the 2005 IEEE International*, 29-31 Aug. 2005, pp. 892–896.

[13] D. C. Malocha, D. R. Gallagher, and N. Y. Kozlovski, "6j-5 ultra wide band communication systems using orthogonal frequency coded saw correlators," in *Ultrasonics Symposium, 2006. IEEE*, 2-6 Oct. 2006, pp. 1075–1078.

[14] R. Tancrell and M. Holland, "Acoustic surface wave filters," vol. 59, no. 3, march 1971, pp. 393 – 409.

[15] C. Campbell, *Surface acoustic wave devices for wireless and mobil communications*. Academic Press, Inc., 1998.

[16] W. P. Mason, *Electormechanical Transducers and Wave Filters*. Princeton, N.J.: Van Nostrand, 1948, pp. 201-209.

[17] W. P. Mason, *Physical Acoustics, IA*. NewYork: Academic Press, Inc., 1964, pp. 169-270.

[18] W. Smith and W. Pedler, "Fundamental- and harmonic-frequency circuit-model analysis of lnterdigital transducers with arbitralry metallization ratios and polarity sequences," *Microwave Theory and Techniques, IEEE Transactions on*, vol. 23, no. 11, pp. 853 – 864, Nov. 1975.

[19] W. Smith, "Basics of the saw interdigital transducer," *European Workshop on the Computer-Aided Design of Surface Acoustic Wave Devices*, vol. 2, pp. 25–63, Jul. 1976.

[20] D. P. Morgan, *Surface-Wave Devices for Signal Processing*. Amsterdam; New York: Elsevier, 1985.

[21] H. Kogelnik, "Coupled wave theory for thick hologram gratings," *Bell System Technical Journal*, vol. 48, no. 9, pp. 2909–2947, 1969.

[22] H. Kogelnik and C. Shank, "Coupled-wave theory of distributed feedback lasers," *Journal of Applied Physics*, vol. 43, no.5, pp. 2327–2335, 1972.

[23] H. Haus and P. Wright, "The analysis of grating structures by coupling-of-modes theory," in *1980 Ultrasonics Symposium*, 1980, pp. 277 – 281.

[24] D.-P. Chen and H. Haus, "Analysis of metal-strip SAW gratings and transducers," *Sonics and Ultrasonics, IEEE Transactions on*, vol. 32, no. 3, pp. 395–408, May 1985.

[25] B. Abbott, "A coupling of modes model for SAW transudcers with arbitrary reflectivity weighting," Ph.D. dissertation, University of Central Florida, Orlando, FL., 1989.

[26] J. Plessky, V. Koskela, "Coupling of modes analysis of SAW devices," *International Journal of High Speed Electronics and Systems*, vol. 10, No.4, pp. 867–947, 2000.

[27] K.Dransfeld and E. Salzmann, "Excitation, detection and attenuation of high frequency elastic surface waves," *W.P. Mason and R.N. Turston (eds.), Physical Acoustics*, vol. 7, pp. 219–272, 1970.

[28] N. Saldanha, "Coupling of modes model and analysis of one-port SAW resonators on Langanite and Langatate," Master's thesis, University of Central Florida, Orlando, FL, 2003.

[29] C. Elachi, "Waves in active and passive periodic structures: A review," in *Proceedings of IEEE, vol. 64, pp.1666-1698*, December 1976.

[30] P. Wright, "A new generalized modeling of SAW transducers and gratings," in *Frequency Control, 1989., Proceedings of the 43rd Annual Symposium on*, 31 May-2 June 1989, pp. 596–605.

[31] P. Wright, "Analysis and design of low-loss saw devices with internal reflections using coupling-of-modes theory," *Ultrasonics Symposium, 1989. Proceedings., IEEE 1989*, pp. 141 –152 vol.1, oct. 1989.

[32] G. Tobolka, "Mixed matrix representation of saw transducers," *Sonics and Ultrasonics, IEEE Transactions on*, vol. 26, no. 6, pp. 426 – 427, nov. 1979.

[33] R. Peach, "A general approach to the electrostatic problem of the saw interdigital transducer," *Sonics and Ultrasonics, IEEE Transactions on*, vol. 28, no. 2, pp. 96 – 104, mar. 1981.

[34] S. Datta and B. Hunsinger, "Element factor for periodic transducers," *Sonics and Ultrasonics, IEEE Transactions on*, vol. 27, no. 1, pp. 42 – 44, jan. 1980.

[35] D. Morgan, "Cascading formulas for identical transducer p-matrices," *Ultrasonics, Ferroelectrics and Frequency Control, IEEE Transactions on*, vol. 43, no. 5, pp. 985 –987, sep. 1996.

[36] J. Campbell and W. Jones, "A method for estimating optimal crystal cuts and propagation directions for excitation of piezoelectric surface waves," *Sonics and Ultrasonics, IEEE Transactions on*, vol. 15, no. 4, pp. 209 – 217, Oct. 1968.

[37] K. Shibayama, K. Yamanouchi, H. Sato, and T. Meguro, "Optimum cut for rotated y-cut linbo3crystal used as the substrate of acoustic-surface-wave filters," *Proceedings of the IEEE*, vol. 64, no. 5, pp. 595 – 597, May 1976.

[38] J. Hornsteiner, E. Born, G. Fischerauer, and E. Riha, "Surface acoustic wave sensors for high-temperature applications," in *Frequency Control Symposium, 1998. Proceedings of the 1998 IEEE International*, May 1998, pp. 615 –620.

[39] J. Diaz, H. Karrer, J. Kusters, J. Matsinger, and M. Schulz, "The temperature coefficient of delay-time for x-propagating acoustic surface-waves on rotated y-cuts of alpha quartz," *Sonics and Ultrasonics, IEEE Transactions on*, vol. 22, no. 1, pp. 46 – 49, Jan. 1975.

[40] N. Naumenko and L. Solie, "Optimal cuts of langasite, la3ga5sio14 for saw devices," *Ultrasonics, Ferroelectrics and Frequency Control, IEEE Transactions on*, vol. 48, no. 2, pp. 530 –537, Mar. 2001.

[41] R. Li and J. Melngailis, "The influence of stored energy at step discontinuities on the behavior of surface-wave gratings," *Sonics and Ultrasonics, IEEE Transactions on*, vol. 22, no. 3, pp. 189–198, May 1975.

[42] P. Wright, "Modeling and experimental measurements of the reflection properties of SAW metallic gratings," *IEEE 1984 Ultrasonics Symposium*, pp. 54 –63, 1984.

[43] D. Puccio, N. Saldanha, D. Malocha, and M. Pereira da Cunha, "SAW reflectivity and resonator results for LGT and LGN," in *Frequency Control Symposium and PDA Exhibition, 2002. IEEE International*, 29-31 May 2002, pp. 324–327.

[44] S. Datta and B. J. Hunsinger, "First-order reflection coefficient of surface acoustic waves from thin-strip overlays," *Journal of Applied Physics*, vol. 50, pp. 5661–5665, 1979.

[45] P. Cross, "Properties of reflective arrays for surface acoustic resonators," *Sonics and Ultrasonics, IEEE Transactions on*, vol. 23, no. 4, pp. 255 – 262, Jul 1976.

[46] S. Lehtonen, V. Plessky, C. Hartmann, and M. Salomaa, "Extraction of the saw attenuation parameter in periodic reflecting gratings," *IEEE Transactions on Ultrasonics, Ferroelectrics and Frequency Control*, vol. 52, no. 1, pp. 111 –119, 2005.

[47] L. Reindl, G. Scholl, T. Ostertag, H. Scherr, U. Wolff, and F. Schmidt, "Theory and application of passive saw radio transponders as sensors," *Ultrasonics, Ferroelectrics and Frequency Control, IEEE Transactions on*, vol. 45, no. 5, pp. 1281 –1292, Sep. 1998.

[48] A. Pohl, "A review of wireless saw sensors," *Ultrasonics, Ferroelectrics and Frequency Control, IEEE Transactions on*, vol. 47, no. 2, pp. 317 –332, 2000.

[49] G. Montress, T. Parker, and J. Callerame, "A miniature hybrid circuit saw oscillator using an all quartz packaged resonator," in *IEEE 1985 Ultrasonics Symposium*, 1985, pp. 277 – 282.

[50] H. Scherr, G. Scholl, F. Seifert, and R. Weigel, "Quartz pressure sensor based on saw reflective delay line," in *Ultrasonics Symposium, 1996. Proceedings., 1996 IEEE*, vol. 1, Nov. 1996, pp. 347 –350 vol.1.

[51] U. Wolff, F. Schmidt, G. Scholl, and V. Magori, "Radio accessible saw sensors for non-contact measurement of torque and temperature," in *Ultrasonics Symposium, 1996. Proceedings., 1996 IEEE*, vol. 1, Nov. 1996, pp. 359 –362 vol.1.

[52] J. Meel. Spread spectrum (ss) introduction. [online], available:. [Online]. Available: http://www.sss-mag.com/pdf/Ss_jme_denayer_intro_print.pdf

[53] C. Cook and H. Marsh, "An introduction to spread spectrum," *Communications Magazine, IEEE*, vol. 21, no. 2, pp. 8 – 16, Mar. 1983.

[54] V. P. Ipatov, *Spread Spectrum and CDMA Principles and Applications*. Jonh Wiley & Sons Ltd., 2005.

[55] D. Torrieri, *Principles of Spread-Spectrum Communication Systems*. Springer Science+Business Meida, Inc., 2005.

[56] S. M. Nabritt, "Simulation and performance analysis of a wireless local area network," Ph.D. dissertation, University of Central Florida, 2002.

[57] F. Schmidt, O. Sczesny, C. Ruppel, and V. Magori, "Wireless interrogator system for saw-identification-marks and saw-sensor components," pp. 208 –215, Jun. 1996.

[58] D. Malocha, D. Puccio, and D. Gallagher, "Orthogonal frequency coding for saw device applications," in *Ultrasonics Symposium, 2004 IEEE*, vol. 2, 23-27 Aug. 2004, pp. 1082–1085Vol.2.

[59] N. Kozlovski and D. Malocha, "Saw passive wireless multi sensor system," pp. 1541 –1544, 2009.

[60] N. Kozlovski and D. Malocha, "SAW noise-like anti-collision code study," *Frequency Control Symposium, 2009 Joint with the 22nd European Frequency and Time forum. IEEE International*, pp. 616 –621, 2009.

[61] D. Puccio, D. Malocha, and N. Saldanha, "Multiple access saw sensors using orthogonal frequency coding," in *Sensors, 2005 IEEE*, 30 2005-nov. 3 2005, p. 4 pp.

[62] D. Malocha, D. Puccio, and N. Lobo, "Reflector design for orthogonal frequency (OFC) coded devices," in *Ultrasonics Symposium, 2006. IEEE*, 2-6 Oct. 2006, pp. 820–824.

[63] B. Santos, "SAW reflective transducers and antennas for orthogonal frequency coded SAW sensors," Master's thesis, University of Central Florida, 2009.

[64] S. Lehtonen, V. Plessky, N. Bereux, and M. Salomaa, "Performances of short reflectors on 128 deg; linbo3," in *Ultrasonics Symposium, 2004 IEEE*, vol. 1, 2004, pp. 433 – 436 Vol.1.

[65] S. Datta and B. Hunsinger, "An analysis of energy storage effects on SAW propagation in periodic arrays," *Sonics and Ultrasonics, IEEE Transactions on*, vol. 27, no. 6, pp. 333 – 340, Nov 1980.